

Dissertation
submitted to the
Combined Faculties for Natural Sciences and for Mathematics of the
Ruperto-Carola University of Heidelberg, Germany
for the degree of
Doctor of Natural Sciences

presented by
Dipl.-Phys. Christian Domesle
born in Wasserlos

Oral examination: 4th of July, 2012

Momentum Imaging of Photofragments and Photoelectrons using Fast Ion Beams

Referees:

Prof. Dr. Andreas Wolf

Priv.-Doz. Dr. Alexander Dorn

Photofragment und Photoelektronen Spektroskopie an schnellen Ionen-Strahlen — Im Rahmen der vorliegenden Arbeit wurde eine Methode zur Fragmentations-Kanal spezifischen Detektion von Photoelektronen der photoneninduzierten Dissoziation von schnellen Molekül-Ionen Strahlen etabliert. Hierfür wurde ein neuartiges Sattelpunkt Elektronen-Spektrometer zunächst zur Untersuchung der Photodetachment Dynamik an einem Strahl negativ geladener O^- Ionen bei 532 nm in Betrieb genommen. Um alle Reaktionsprodukte der Photolyse von kleinen Wasserclustern $(H_2O)_nH^+$ ($n \leq 3$) im Wellenlängenbereich von 13.5-40 nm zu erfassen, kam zusätzlich ein neu entwickeltes Detektionssystem für schwere Ionen-Fragmente zum Einsatz, welches in Kombination mit dem Sattelpunkt Spektrometer zur Untersuchung der dissoziativen Photoionisation des Hydronium- (H_3O^+) und des Zundel-Ions ($H_5O_2^+$) eingesetzt wurde. Hierbei konnte nachgewiesen werden, dass im Falle von H_3O^+ drei dominierende Zerfalls-Kanäle ein binärer $H_2O^+ + H^+$ und zwei Dreikörper Aufbrüche $OH^+ + 2H^+$, $OH^+ + H^+ + H$ durch Ionisation eines Außen-Valenz Elektrons initiiert wird. Durch die erstmalig gemessenen Elektronen-Spektren konnte gezeigt werden, dass vorrangig die Ionisation des $3a_1$ Orbitals den binären Kanal bedingt, wohingegen eine Vakanz im $1e_1$ Orbital zur Fragmentation in den Dreikörper-Kanal führt. Weiterhin wurde die Photolyse von $H_5O_2^+$ studiert, wobei fünf dominante Kanäle identifiziert werden konnten, bei denen in einer Großzahl von Reaktionen das Hydronium-Ion selbst abgespalten wird. Das gemessene Elektronen-Signal zeigt auch hier, dass vorrangig Vakanzen in den Außenorbitalen zur Dissoziation des Moleküls führen.

Momentum imaging of photofragments and photoelectrons using fast ion beams — Within the framework of this thesis a method for break-up channel specific detection of the photoelectrons from photon-induced dissociation processes of fast moving molecular ion has been established. For this purpose, a novel saddle-point electron spectrometer was commissioned while investigating the photodetachment dynamics on a fast moving beam of oxygen anions. For a complete detection of all outgoing reaction products emerging from the photolysis of small water clusters $(H_2O)_nH^+$ ($n \leq 3$) in the wavelength range of 13.5-40 nm a new fragment analyzing system has been developed and, in combination with the novel saddle-point spectrometer applied, to investigate the dissociative photoionization of the hydronium (H_3O^+) and the Zundel ion ($H_5O_2^+$). In case of the hydronium ion, a binary $H_2O^+ + H^+$ and two three-body channels $OH^+ + 2H^+$, $OH^+ + H^+ + H$ have been identified to be initiated by outer valence vacancies where the binary channel is mainly triggered by the ionization of the $3a_1$ orbital and the three-body channels follow ionization from the $1e_1$ orbital. The photolysis of $H_5O_2^+$ is found to proceed via five prominent pathways where for a large number of processes the hydronium ion is split off as a stable structural unit. Also here, the investigation of the photoelectron spectra revealed the prominent dissociation pathways to be initiated by outer valence vacancies.

Contents

1	Introduction	1
2	Background	5
2.1	Dissociative photoionization of polyatomic ions	5
2.1.1	Potential energy surface	5
2.1.2	Photoionization of molecular ions	7
2.1.3	Electron and heavy fragment energies	8
2.2	Fast beam fragmentation	12
2.2.1	Break-up process	13
2.2.2	Photofragment angular distribution	17
2.3	Photoelectron detection with fast beams	20
2.3.1	Photoelectron angular distribution	20
2.3.2	Photoelectron velocities	20
3	Experimental technique	25
3.1	Trapped Ion Fragmentation setup at FLASH (TIFF)	25
3.1.1	Hollow cathode ion source	27
3.1.2	Fragment detection system	31
3.1.3	New heavy charged fragment analyzer	32
3.2	Electron spectrometer	36
3.2.1	Saddle point electron spectrometer	36
3.2.2	Magnetic bottle electron spectrometer	43
3.3	Position sensitive fragment detectors	44
3.3.1	Multi-Channel Plate	44
3.3.2	Delay line detection principle	45
3.4	The Free-Electron Laser FLASH	47
3.5	Data acquisition and analysis	49
3.5.1	Data acquisition	50
3.5.2	Data analysis	51

4	Electron emission from fast O^- ions	55
4.1	Magnetic bottle spectrometer	56
4.1.1	Experimental parameters	57
4.1.2	Experimental results	58
4.1.3	Monte Carlo model	59
4.1.4	Discussion	61
4.2	Saddle point spectrometer	62
4.2.1	Experimental parameter	62
4.2.2	Experimental results	63
4.2.3	Monte Carlo Simulation	64
4.3	Conclusion	65
5	Free electron laser experiments on H_3O^+	67
5.1	Properties of H_3O^+	67
5.2	Photoionization pathways	68
5.3	Fragmentation	71
5.3.1	Experimental parameters	71
5.3.2	Fragment assignment	72
5.3.3	Fragmentation pathways	73
5.3.4	Photofragment momentum imaging	75
5.4	Photoelectron spectroscopy	82
5.4.1	Experimental parameters	82
5.4.2	Experimental results	84
5.4.3	Coincidence with light charged fragment	84
5.4.4	Coincidence with charged water	86
5.4.5	Double coincidence with light fragments	87
5.4.6	Monte Carlo Simulation	88
5.5	Discussion	91
5.5.1	Two-body break-up: $\text{H}_2\text{O}^+ + \text{H}^+$	91
5.5.2	Three-body break-up: $\text{OH} + \text{H}^+ + \text{H}^+$	96
6	Free electron laser experiments on $\text{H}^+(\text{H}_2\text{O})_2$	99

6.1	Properties of $\text{H}^+(\text{H}_2\text{O})_2$	100
6.2	Photoionization pathways	101
6.2.1	Expected fragmentation pathways	102
6.3	Fragmentation	103
6.3.1	Experimental parameters	103
6.3.2	Fragment assignment	103
6.3.3	Assignment of fragmentation pathways	104
6.3.4	Photofragment momentum imaging	112
6.4	Photoelectron spectroscopy	114
6.4.1	Coincidence with H_2O^+	114
6.4.2	Coincidence with H_3O^+	115
6.4.3	Monte Carlo Simulation	116
6.5	Discussion	118
7	Summary and outlook	121
A	Monte Carlo simulation	125
A.1	SIMION based Monte-Carlo Simulation	125
A.2	Parametric Monte-Carlo model	127
	Bibliography	131
	Danksagung	139

Chapter 1

Introduction

Cluster formation of water molecules around a proton is often found in the gas as well as liquid phase. Especially small systems like $(\text{H}_2\text{O})_n\text{H}^+$ ($n \leq 3$) have attracted immense research interest since they have been identified as fundamental structural units of cluster formation [Mar99, Nie08]. The hydronium ion H_3O^+ is also of key importance for the oxygen chemistry in interstellar environments and planetary atmospheres [Ste95, Hol99]. In these media the major destruction mechanisms of such a system is dissociative recombination with electrons but also photodissociation and dissociative photoionization can be initiated by photons in the vacuum ultra-violet (vuv) and soft x-ray spectral regions [Leq91, Ste95, Sta05].

Dissociative recombination [Buh10] and photodissociation have been subject to numerous theoretical and experimental researches. Up to now, only little is known about the dissociative photoionization of these clusters where a further ionization promotes the system into a dissociative state of the dication. The potential energy which is associated with the valence vacancy is equivalent to the orbital energy of the ionized shell. Thus, one important quantity to get insight on the dynamics of the dissociative photoionization is the energy spectrum of the emitted photoelectrons. This yields precise information on the amount of energy which is deposited in the target and on the potential energy surface as it arises from valence ionization. On the other hand, the dissociative potential surface can lead to a variety of final channels via largely unexplored pathways. In this decay the potential energy is transformed into internal excitation of the fragments and measurable kinetic energies of the break-up products, lying in the range of a few eV. Thus, the production of the different fragment types provides information on the dissociative dicationic potential surface.

The best control over the target conditions in laboratory setups to investigate photon induced fragmentation mechanisms like dissociative photoionization can be achieved by gas-phase experiments which allow to study the species of interest without the environmental interactions as they are present in the liquid phase. Up to now, such investigations on dilute gas-phase targets and in particular on ions, were impeded by the absence of an appropriate light source delivering a sufficient photon flux. With the advent of Free Electron Laser light sources, like the **Free-electron LASer in Hamburg**, the molecular break-up dynamics after inner or outer valence shell ionization can be probed. Among others, the fast beam method has been shown to be an appropriate means giving access to all fragments emerging break-up processes triggered by valence shell ionization.

In order to study photodissociation and dissociative photoionization processes on molecular ions under xuv-conditions, the fast ion beam infrastructure TIFF (**T**rapped **I**on **F**ragmentation with an **FEL**) has been set up at FLASH facility. The ion beam with a typical kinetic energy of 2 – 8 keV is perpendicularly crossed with the laser beam. With three-dimensional imaging detectors the emerging photofragments, travelling on a forward cone around the parent ion beam, can be analyzed employing time and position resolution.

The first dissociative photoionization experiments at TIFF on the H_3O^+ and the Zundel ion H_5O_2^+ were done at photon energies of 92 eV and 90 eV, respectively [Ped09, Lam10]. The hydronium ion H_3O^+ was found to fragment into a dominant binary $\text{H}_2\text{O}^+ + \text{H}^+$ and a three-body $\text{OH} + 2\text{H}^+$ break-up channel. For H_5O_2^+ a prominent two-body fragmentation pathway $\text{H}_2\text{O}^+ + \text{H}_3\text{O}^+$ has been identified. In these studies neither the photoelectrons nor most of the heavy ionic fragments could be observed.

One critical aspect in assigning the fragmentation pathways, especially for larger systems, arises from the requirement of efficient detection of all break-up products. Within the framework of this thesis a new fragment detection system has been developed and successfully applied to detect a number of additional fragments arising from the break-up processes. Additionally a novel electrostatic saddle-point electron spectrometer has been commissioned and used to detect electron emission following photoionization in the optical and soft x-ray regime. The recent upgrade of the TIFF detection system, performed in the framework of this thesis, in fact allows coincident detection of all outgoing reaction products, from the incident photoelectron to the

neutral and all ionic fragments.

In the following, the background of molecular photodissociation and photoionization is discussed (chapter 2). The experimental setup and the newly developed components are introduced in chapter 3. In dedicated investigations of the photodetachment dynamics on a fast moving O^- beam at photon energies of 2.3 eV and 4.7 eV, using the newly built saddle-point spectrometer and also a magnetic-bottle electron spectrometer, methods have been developed to map the angular distribution of the photoelectron into the time-of-flight domain. The results revealing the properties of photoelectron spectroscopy on fast ion beams are presented in Chapter 4. Chapter 5 reviews the experimental results obtained for the dissociative photofragmentation of H_3O^+ at a photon energy of 56.7 eV. Here, the novel saddle-point electron spectrometer has been successfully brought into operation, allowing for the first time to detect the photoelectrons ionized from a fast-moving ion beam under xuv-radiation. Also the findings obtained with the new heavy charged fragment detection system are described. With this system a break-up channel resolved analysis of the photoelectron as well as the photofragment spectrum is possible. Within the experimental campaign the dissociative photofragmentation of H_5O_2^+ at a photon energy of 56.7 eV has also been investigated. Chapter 6 deals with the results which have been found therein. Among the manifold of possible fragmentation pathways two dominant channels have been identified in which the hydronium ion is split off as a stable structural unit. Moreover, photoelectrons could be detected also for this species. Chapter 7 provides a summary of the experimental results and gives an outlook on future experiments.

Chapter 2

Background

In the upcoming chapter the dissociation of polyatomic ions initiated by valence shell vacancies is discussed. Within the framework of the potential energy surface the process of photoionization and subsequent dissociation is qualitatively illustrated, whereas in the second half of the chapter the fast beam method applied to study the dissociation and photoionization mechanisms will be introduced.

2.1 Dissociative photoionization of polyatomic ions

2.1.1 Potential energy surface

A molecule comprises N bound electrons and more than one atom, where the electrons are shared among the core level and valence orbitals of the individual atoms. The core electrons, which are closest to the nuclei, exhibit the largest binding energies. In contrast to them, the valence electrons, which are shared among the inner and outer valence orbitals, participate in the bonding of the molecule. The Hamiltonian of a molecular system with N electrons can be written in the form

$$(T_N + T_e + V_c)\psi(\{\vec{R}\}, r_1 \dots r_N) = E\psi(\{\vec{R}\}, r_1 \dots r_N), \quad (2.1)$$

where the kinetic energy operators of the system's nuclei and electrons are represented by T_N and T_e , respectively. The potential energy of the system due to the Coulomb interaction is expressed by V_c . The coordinates of the nuclei are given by $\{\vec{R}\}$ and the position of each of the N electrons with respect to the center of mass of the system is denoted by r_i . Since the masses of the nuclei and electrons differ

significantly the time scale of the nuclear motion is much longer compared to the one of the electrons. In the Born-Oppenheimer approximation [Bor27] this effect is used in a way that the wave function of the molecule can be separated into a nuclear component $\chi(\{\vec{R}\})$ and an electronic one $\phi(\{\vec{R}\}, \vec{r})$. This well-known approach is treated in great detail in many textbooks about molecular physics and shall be illustrated only briefly at this point. The eigenfunctions $\phi_n(\{\vec{R}\}, \vec{r})$ of the electronic motion are determined for a fixed nuclear distance $\{\vec{R}\}$

$$(T_e + V_c)\phi_n(\{\vec{R}\}, r_1 \dots r_N) = E_n(\{\vec{R}\})\phi_n(\{\vec{R}\}, r_1 \dots r_N), \quad (2.2)$$

and the eigenenergies $E_n(\{\vec{R}\})$ of the electronic wave function, which include energy contributions from the Coulomb repulsion between the nuclei and the electronic binding, are used to formulate the nuclear Schrödinger equation

$$(T_N + E_n(\{\vec{R}\}))\chi_n(\{\vec{R}\}) = E\chi_n(\{\vec{R}\}). \quad (2.3)$$

and to derive the nuclear wave function $\chi_n(\{\vec{R}\})$. The total wave function of the molecule in an electronic state n is obtained by solving eq. (2.2) and eq. (2.3) for each nuclear configuration $\{\vec{R}\}$ as the product of $\phi_n(\{\vec{R}\}, \vec{r})\chi_n(\{\vec{R}\})$.

The electron energy $E_n(\{\vec{R}\})$ as a function of the nuclear coordinate $\{\vec{R}\}$ define in case of a diatomic molecule, the *adiabatic potential energy curve* and for a polyatomic system the *adiabatic potential energy surface* (PES), where the dimension of the configuration space $\{R\}$ is a function of the number of nuclei.

In case of a diatomic molecule a single internal coordinate R is relevant, representing the distance between the nuclei. For $(R \rightarrow 0)$ the potential energy is dominated by the Coulomb repulsion between the nuclei, and for $(R \rightarrow \infty)$ the constant value is given by the sum of the energies of the two atoms which are bound in the molecule. In the geometrical equilibrium R_0 , the potential energy curve exhibits a minimum and thus a vibrational motion of the nuclei is described as an oscillation around that minimum.

For a polyatomic system the dynamics of internal vibrations or reactions can be described within the potential energy surface (PES). For a two dimensional representation an appropriate coordinate like a bond length or an angle between two bonds has to be introduced to express the internal motion of the nuclei on the PES. Every molecule allows certain symmetry transformations, like a rotation around a selective axis of the system, which preserve the nuclear configuration, whereupon the same

type of atoms within the molecule are considered to be indistinguishable. The PES is characterized by the properties of the electronic wave function with respect to this symmetry transformation. By this, the electronic state can be classified through a symmetry group, which is usually expressed in the Schönflies notation [Dem03] and determines, among others, the allowed and forbidden transitions between different electronic states.

As illustrated above, in the Born-Oppenheimer approximation the electronic and nuclear motion are treated independently. For photoionization processes the kinetic energy of the nuclei can become large, which may lead to a breakdown of the Born-Oppenheimer approximation, i.e. the electronic and nuclear motion cannot be considered as decoupled anymore. The adiabatic potential curves are not allowed to cross [Neu29], so the coupling of the electronic and nuclear motion would lead to *avoided crossings*. In case of a polyatomic system the potential energy surfaces of two electronic states with identical symmetry can cross at a so called *conical intersection* [Ced04] with strong coupling of electronic and nuclear motion becoming visible in the vicinity of such intersections.

2.1.2 Photoionization of molecular ions

In the context of this thesis only such molecular cations are considered where an additional proton is attached to a neutral closed shell system, as for example $\text{H}^+ + \text{H}_2\text{O} \rightarrow \text{H}_3\text{O}^+$. Therefore, the following discussion of the ionization processes is focused on this type of singly charged molecular ions. For all experiments which are presented in the upcoming chapters the employed photon energies range from $E_\gamma = 2 - 100 \text{ eV}$, i.e., they are sufficient to ionize valence electrons only.

If the energy of a single photon of the irradiating light, $\hbar\omega$, exceeds the ionization threshold of either an inner or outer valence shell an electron can be removed from these orbitals. The time scale of the electronic motion is short compared to that of the nuclei. Thus, the ionization can be considered as a vertical transition between two potential energy surfaces where the dication is formed in a repulsive state. Depending on whether an inner or outer valence electron is removed different relaxation processes can occur, i.e., the system can either undergo a direct dissociation or may release further electrons via autoionization processes.

Fig. 2.1(a) illustrates the photoionization of an inner valence electron, which may

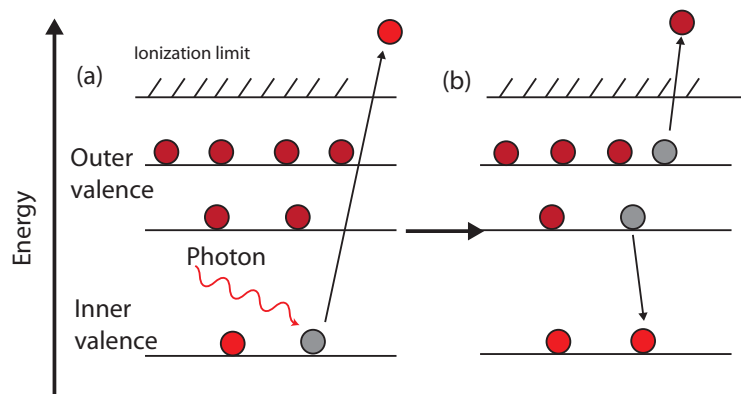


Figure 2.1: (a) Illustration of single photon inner valence shell ionization. (b) Auger autoionization process.

be followed by the Auger decay [Aug25] shown in fig. 2.1(b). Before the system dissociates the inner valence vacancy is refilled by an outer valence electron of less binding energy. The energy gain which is associated with the refilling is transferred to another outer valence electron which is then emitted. The Auger decay is considered as a process that takes place within a single molecule.

For larger systems such as water clusters (chapter 6) also different autoionization pathways like Intermolecular Coulombic Decay (ICD) may take place if an inner valence electron is ionized from the cluster. This process was first proposed by Cederbaum et al. in 1997 [Ced97]. In the following, the mechanism, illustrated in fig. 2.2, is briefly reviewed for the protonated water dimer according to the discussion given in [Mue05]. As it will be shown in chapter 6, the water molecules are arranged at about equal distance to each side of the central H^+ . An inner valence vacancy at one of the water molecules can be refilled by an outer valence electron of the same water molecule. Because of the valence vacancy on this water molecule, the binding energy of the remaining electrons is increased and autoionization is suppressed. However, the energy gain associated with the refilling process can be transferred to the remote site, leading to the ejection of an outer valence electron on the other water molecule. The secondary, slow electron thus reflects the orbital structure of the unionized water molecule.

2.1.3 Electron and heavy fragment energies

The upcoming paragraph deals with the energetics of the dissociative photoionization process for a polyatomic system ABC^+ initiated by outer valence shell ionization.

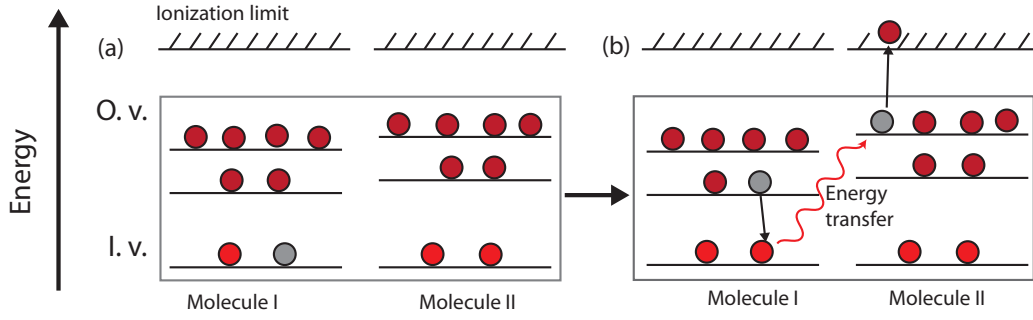


Figure 2.2: Illustration of ICD process. (a) Elevated binding energy due to inner valence vacancy. (b) The energy gain associated with the refilling of the inner valence vacancy is transferred to a neighboring water molecule where another outer valence electron is ionized.

The photoionization process of the molecular ion can be formally written as

$$\text{ABC}^+(\{v\}, J, n) + \hbar\omega \rightarrow \text{ABC}^{++} + e^-, \quad (2.4)$$

where $(\{v\}, J, n)$ are the vibrational, rotational and electronical quantum numbers of the monocation. Starting out from an initial state i with a certain vibrational level $\{v\}$ of the monocation, the ionization process promotes the system into a repulsive state of the dication ABC^{++} with a final state energy E_f . The probability $P(E_f)$ for such a process to take place is proportional to the Franck-Condon factor $\propto |\langle \chi_f | \chi_i \rangle|^2$, which is given by the overlap integral of the initial and final state nuclear wave functions χ_i and χ_f .

For illustration fig. 2.3 displays the dissociative photoionization process of a diatomic molecular ion $\text{AB}^+ + \hbar\omega \rightarrow \text{AB}^{++} \rightarrow \text{A}^+ + \text{B}^+$ along the repulsive potential curve $V_2(R)$ (blue line) into two singly charged atomic fragments. The energy balance for this reaction is

$$\hbar\omega + E_i = E_{(k, e^-)} + E_f + E(\text{A}^+ + \text{B}^+), \quad (2.5)$$

with $E_{(k, e^-)}$ the kinetic energy of the emitted electron and $E(\text{A}^+ + \text{B}^+)$ the energy of the dissociated system.

For the polyatomic system the discussion has to be carried out in the framework of a potential energy surfaces (PES). As mentioned in the previous section the dimension of the PES depends on the number of atoms which are bound in the parent molecule. Therefore, the relaxation of the dicationic state can proceed on this

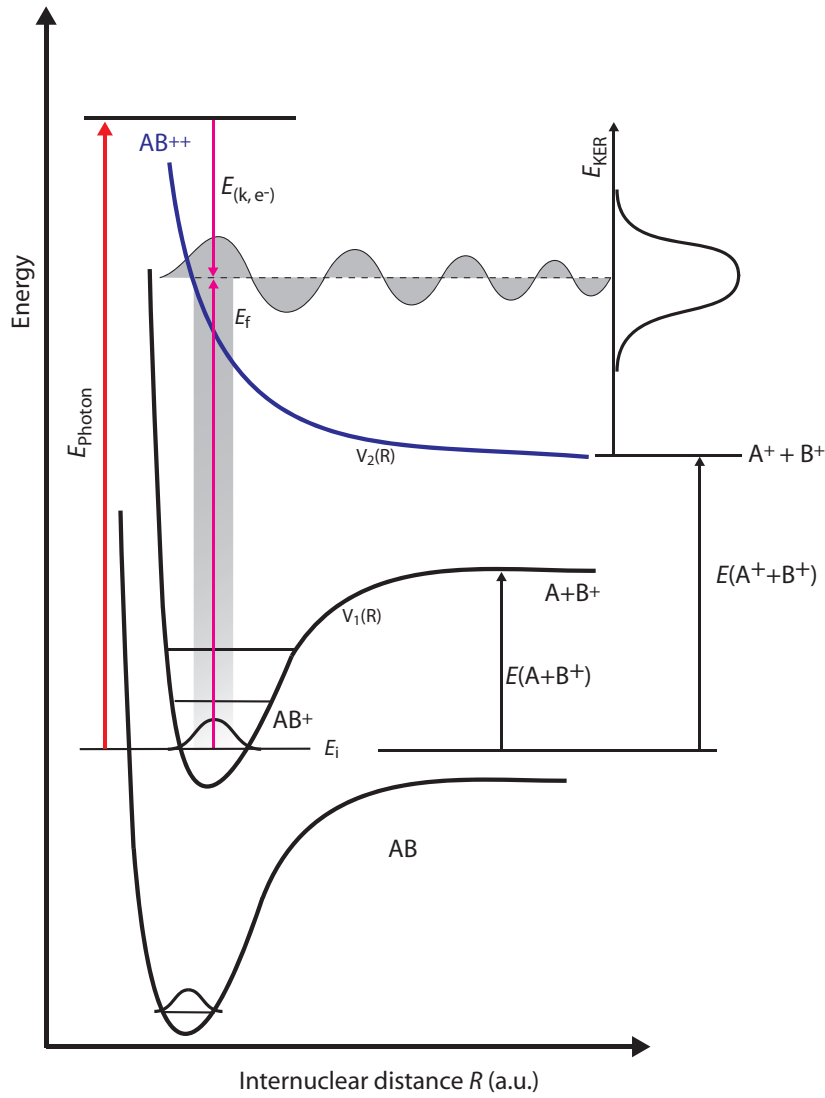


Figure 2.3: Potential energy curve of a diatomic molecule after valence shell ionization, assuming a repulsive state of the dication. The gray shaded area represents the Franck-Condon region. The red vertical arrow indicates the available photon energy.

multidimensional surface via several pathways into different final channels



Moreover, in this case the molecular fragments may include internal excitation energy as it is depicted in fig. 2.4. Considering reaction channel(2) in eq. (2.6), the energy

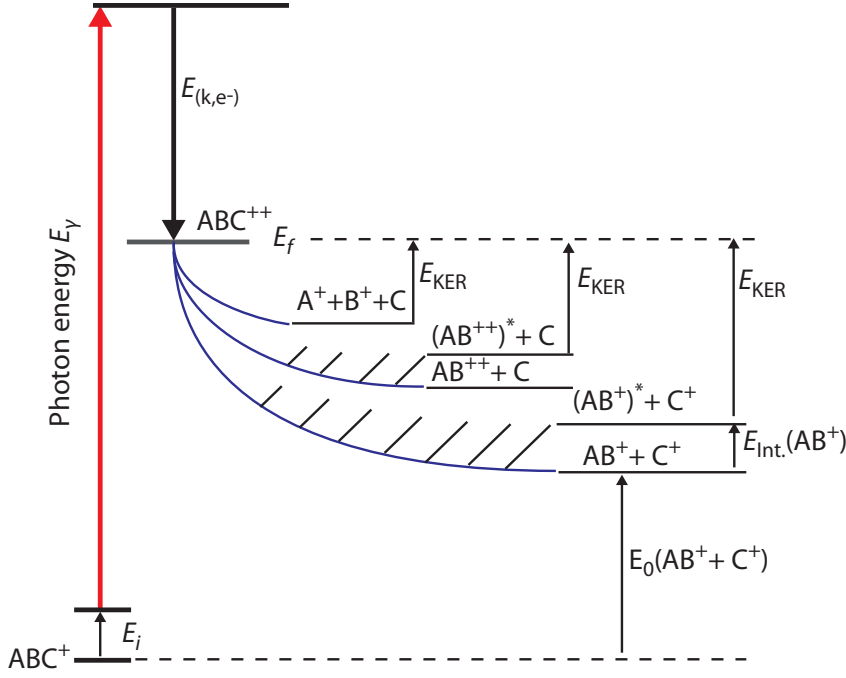


Figure 2.4: Energy level scheme for dissociative photoionization process of a polyatomic molecular ion ABC^+ into different channels.

balance of the dissociative photoionization is given by

$$\hbar\omega + E_i = E_{(k,e^-)} + E_f + E(AB^+ + C^+), \quad (2.7)$$

where $E_{(k,e^-)}$ expresses the kinetic energy of the emitted electron and E_i denotes the vibrational energy of the initial state. The energy of the dissociated system

$$E(AB^+ + C^+) = E_0(AB^+ + C^+) + E_{\text{Int.}}(AB^+) \quad (2.8)$$

is the sum of $E_0(AB^+ + C^+)$, when both break-up products are formed in their ground state and $E_{\text{Int.}}(AB^+)$, which reflects the internal excitation of the molecular fragment, see fig. 2.4. The dissociation energy E_f of the dicationic state is therefore transformed into internal excitation and kinetic energy of the fragments $E_f = E_{\text{Int.}}(AB^+) + E_{\text{KER}}$.

It is instructive to treat the dissociative photoionization process of the molecular system within a more classical description. For a heavy molecule with a high vibra-

tional excitation such a treatment is approximately correct [Nod82, Mul71, Adl82] and the position as well as the momentum of the nuclei are considered as simultaneously well-defined. The kinetic energy $E_{(k,e^-)}$ of an electron, ejected from the polyatomic system, is given by

$$E_{(k,e^-)} = h\omega - (V_2(\{\vec{R}\}) - V_1(\{\vec{R}\})), \quad (2.9)$$

with $V_1(\{\vec{R}\})$ and $V_2(\{\vec{R}\})$ being the local potential energies of the mono- and dication for a certain nuclear configuration $\{\vec{R}\}$. Here, the recoil of the molecule during the ionization process can be neglected. The kinetic energy of one ejected electron therefore reflects the initial and final potential energy surface for a certain nuclear configuration prevailing during the ionization process. Consequently, the spectrum of the photoelectrons manifests, within the Franck-Condon region, the shapes of the initial as well as the final potential energy surfaces. In case of the diatomic molecule the kinetic energy spectrum of the photoelectrons depends, again within the Franck-Condon region, on the shapes of the initial and final potential energy curves $V_1(R)$ and $V_2(R)$, see fig. 2.3.

For the earlier discussed break-up process (2) in eq. (2.6), the energy of the dicationic system

$$E_i(\{\vec{R}\}) + (V_2(\{\vec{R}\}) - V_1(\{\vec{R}\})) = E_{\text{KER}} + E(\text{AB}^+ + \text{C}^+) \quad (2.10)$$

is shared among the fragments as kinetic energy E_{KER} according to eq. (2.10). Thus, the kinetic energy E_{KER} measured in the photofragment spectrum reflects the potential energy surfaces of the initial and final states as well as the amount of energy which is transferred into internal excitation of the molecular fragments.

2.2 Fast beam fragmentation

One experimental approach to study photodissociation or dissociative photoionization processes is the fast ion beam technique. Typical beam energies range from 2 keV to 100 keV where the species of interest is separated from the main beam by using magnetic or electrostatic mass spectrometers. The photon and ion beams are overlapped in an interaction region in either crossed or collinear fashion, see sec. 3.1. The first experiments on photodissociation of fast ion beams were done with an

arc lamp used as a light source in the early seventies [Bus72]. As the laser found its way as a common means in experimental physics they have also been employed as a light source in photodissociation experiments [Oze72, Van74]. The detection systems which have been used in these setups were only sensitive to the fragments emitted along the ion-beam direction. Thus, mainly photodissociation cross sections were derived in these experiments. A milestone for the fast beam method was the advent of 3-dimensional imaging detectors like multi-channel plates with delay-line anodes for position resolution (see sec. 3.3). These detectors allow a position sensitive measurement of the arrival times of the different neutral or multiply charged fragments emerging from a break-up process in the fast beam geometry. By this, relevant physical quantities like the total energy release E_{KER} or the emission angle θ_{F} of the fragments relative to the laser polarization can be deduced. For some species a limitation of the method is imposed by the rather dilute target densities and the photon flux delivered by classical light sources such as synchrotron radiation or lasers not being sufficient to yield acceptable event rates. The advent of Free Electron Lasers with not only high photon flux but also high energetic photons allowed to explore a new range of targets like the small protonated water clusters studied in the context of this thesis.

2.2.1 Break-up process

The experimental observables of each break-up event are the time-of-flight t and the impact position R of the various fragments on imaging detectors. In this section the approach of how the relevant physical quantities can be deduced from these observables will be introduced. The ion beam propagates with velocity v_0 along the laboratory z -axis, see fig. 2.5. A polyatomic molecule is assumed to dissociate into a certain number i of break-up products, which travel in the laboratory frame with the velocity

$$\vec{v}_{(i, \text{lab})} = v_0 \mathbf{e}_{\mathbf{z}} + v_{(i, \text{cm})} \begin{pmatrix} \sin \theta_{i, \text{cm}} \cos \phi_{i, \text{cm}} \\ \sin \theta_{i, \text{cm}} \sin \phi_{i, \text{cm}} \\ \cos \theta_{i, \text{cm}} \end{pmatrix}. \quad (2.11)$$

θ_{cm} represents the angle between the fragment and the ion beam velocity in the center of mass (cm) frame, and ϕ_{cm} , the azimuth angle between the projection of $v_{(i, \text{cm})}$ onto the $x - y$ -plane (see fig. 2.5). The time-of-flight t thus contains the

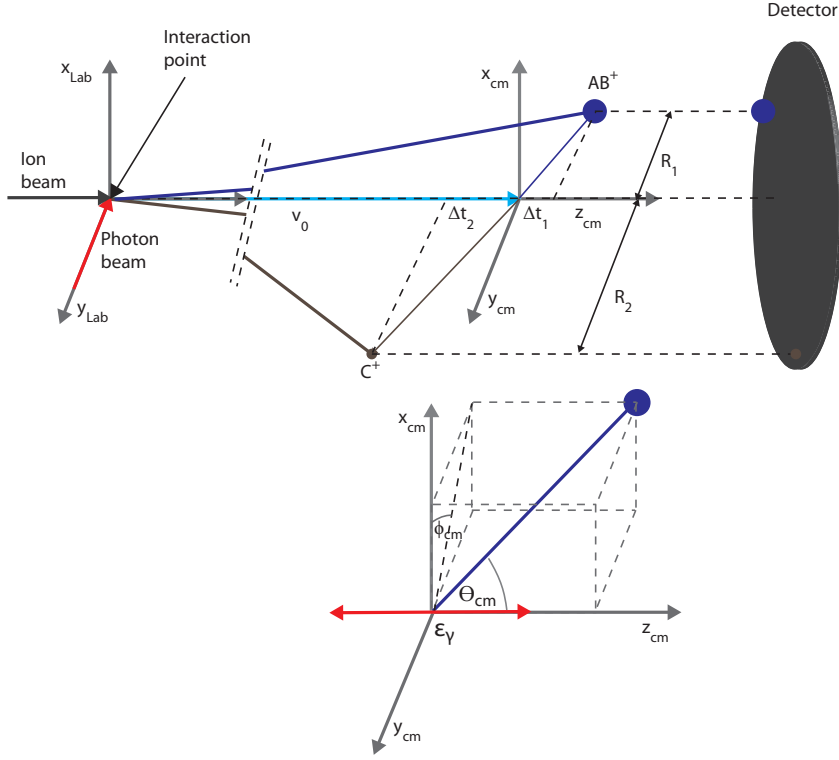


Figure 2.5: Illustration of the kinematics of a two-body break-up process, where the ion beam is assumed to propagate with v_0 along the laboratory z -axis. The observables in the experiment are the time-of-flight t and the radial impact position R on the imaging detector.

longitudinal cm velocities

$$t_i = \frac{L}{v_{(i,z,\text{lab})}} = \frac{L}{v_0} \frac{1}{1 + (v_{(i,\text{cm})}/v_0) \cos \theta_{i,\text{cm}}}, \quad (2.12)$$

whereas the radial position

$$R_i = t_i \sqrt{(v_{(i,x,\text{cm})})^2 + v_{(i,y,\text{cm})}^2} \quad (2.13)$$

is determined by the transverse cm velocities. Additionally, momentum conservation yields for the momenta of the fragments

$$\sum_i m_i v_{(i,\text{cm})} = 0. \quad (2.14)$$

From eqs. (2.12) and (2.13) the total kinetic energy release can be derived

$$E_{\text{KER}} = \sum_i \frac{1}{2} m_i \frac{(L - t_i v_0)^2 + R_i^2}{t_i^2} = \frac{1}{2} m_i \left((v_{i,\text{cm}}^{\parallel})^2 + (v_{i,\text{cm}}^{\perp})^2 \right). \quad (2.15)$$

Under the present conditions, the parallel $v_{i,\text{cm}}^{\parallel} = v_{(i,z,\text{cm})}$ and perpendicular $v_{i,\text{cm}}^{\perp} = \sqrt{(v_{(i,x,\text{cm})})^2 + (v_{(i,y,\text{cm})})^2}$ velocities are defined by the original ion beam direction and the detector plane, respectively.

As given in [Ped09] a set of generalized coordinates can be introduced. The time-of-flight t and the radial position R are normalized to the drift length L and the ion beam velocity v_0 according $\tau_i = (t_i/L)v_0$ and $\rho_i = R_i/L$. With eq. (2.12) and (2.13) these coordinates can be expressed by

$$\begin{aligned} \tau_i &= 1/(1 - v_{i,\text{cm}}^{\parallel}/v_0), \\ \rho_i &= (v_{i,\text{cm}}^{\perp}/v_0)/(1 - v_{i,\text{cm}}^{\parallel}/v_0), \end{aligned} \quad (2.16)$$

and the normalized longitudinal and transversal cm velocities are

$$\begin{aligned} (1 - 1/\tau_i) &= v_{i,\text{cm}}^{\parallel}/v_0, \\ \rho_i/\tau_i &= v_{i,\text{cm}}^{\perp}/v_0. \end{aligned} \quad (2.17)$$

Two-body break-up

A special case arises if the molecule dissociates into two fragments, as illustrated for the reaction $\text{ABC}^{++} \rightarrow \text{AB}^+ (1) + \text{C}^+ (2)$ in fig. 2.5. Under such conditions momentum conservation yields

$$\vec{p}_{1,\text{cm}} = -\vec{p}_{2,\text{cm}}, \quad (2.18)$$

which can be used to determine the kinetic energy as

$$E_{\text{KER}} = \frac{1}{2} \frac{m_i^2}{\mu} \left((v_{i,\text{cm}}^{\parallel})^2 + (v_{i,\text{cm}}^{\perp})^2 \right), \quad (2.19)$$

where $\mu = \frac{m_1 m_2}{m_1 + m_2}$ represents the reduced mass. Thus, the complete kinematics of a two-body break-up can be obtained, if the 3D coordinate of only one product is accessible. Combining eqs. (2.19) and (2.17), the total kinetic energy as a function of

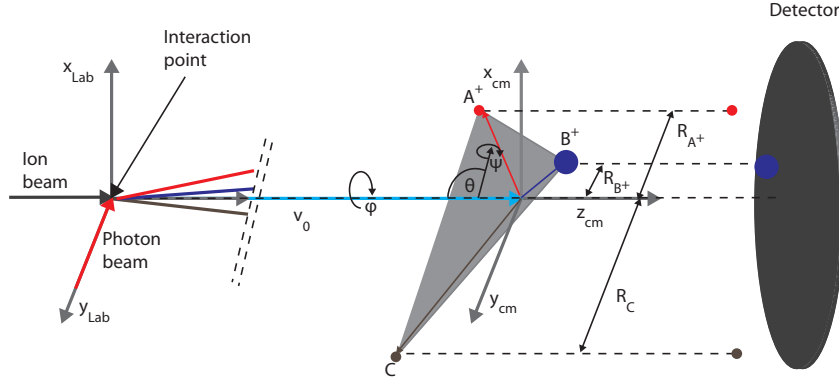


Figure 2.6: Illustration of the kinematics for a three-body break-up process, where the ion beam is assumed to propagate with v_0 along the laboratory z -axis. The observables in the experiment are the time-of-flight t and the radial impact positions R on the imaging detector.

the generalized momenta translates into

$$\left(\frac{2\mu E_{\text{KER}}}{v_0^2 m_i^2} \right) = (1 - 1/\tau_i)^2 + (\rho_i/\tau_i)^2. \quad (2.20)$$

Fragments which are formed in a two body break-up will appear within the normalized momentum plane spanned by $1/\tau_i$ and ρ_i/τ_i on a half circle with a radius given by the relation (2.20).

Three-body break-up

In the third reaction sequence, expressed in relation (2.6), the polyatomic system is assumed to fragment into a three body break-up channel $ABC^{++} \rightarrow A^+ + B^+ + C$. Momentum conservation in the center-of-mass frame forces the fragments of a three-body break-up process to move in a dissociation plane, indicated by the gray shaded area in fig. 2.6, which is spanned by the momentum vectors p_i of the different products. With respect to the laboratory coordinate system, the orientation of the plane can be expressed by the Euler angles Φ , θ , ψ (c.f. fig. 2.6).

Dalitz plots

The geometry of the triangle, which is spanned by the momentum vectors p_i of the fragments, can be visualized within the Dalitz plane. The set of Dalitz coordinates

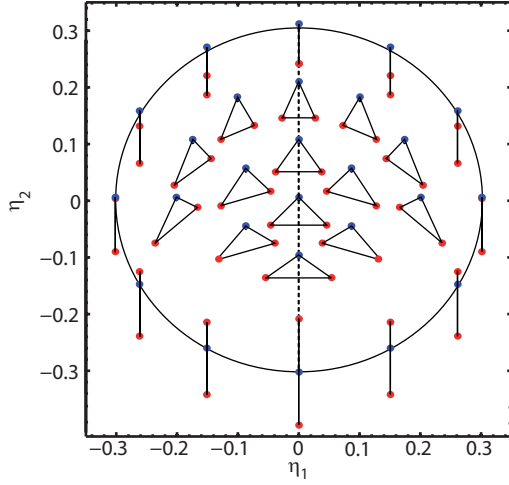


Figure 2.7: Dalitz plot of the three body break-up of H_3O^{++} into $\text{OH} + \text{H}^+ + \text{H}^+$. The break-up geometry of the system is indicated by small triangles, where the blue point represents the OH molecule, and the red points express the H^+ fragments.

was first introduced by R. H. Dalitz in 1953 [Dal53]. For the three-body break-up, $\text{H}_3\text{O}^+ + \gamma \rightarrow \text{H}_3\text{O}^{2+} + e^- \rightarrow \text{OH} + \text{H}^+ + \text{H}^+$ (c.f. sec. 5.3.4) the coordinates, η_1, η_2 are defined as follows

$$\eta_1 = \sqrt{\frac{M}{3m_{\text{OH}}}} \frac{E_{\text{H}_1} - E_{\text{H}_2}}{\sqrt{3}E_{\text{KER}}}, \quad (2.21)$$

$$\eta_2 = \frac{M}{3m_{\text{H}}} \frac{E_{\text{OH}}}{E_{\text{KER}}} - \frac{1}{3}, \quad (2.22)$$

where E_{KER} denotes the total kinetic energy release of the break-up. Since the two protons are non-distinguishable the Dalitz plane exhibits a mirror symmetry on the η_1 -axis. In addition momentum conservation confines all events within the inner part of a circle with a $1/3$ radius around the center of the plane. The events, represented within the Dalitz plane are normalized to the total kinetic energy release E_{KER} of the break-up, allowing a universal representation of this reaction's break-up geometries, independent of the total kinetic energy release.

2.2.2 Photofragment angular distribution

Besides the kinetic energy release, the emission angle θ_i of the fragments relative to the laser polarization can yield important information on the break-up dynamics. In the following, the ion flight direction along the laboratory z -axis is assumed to be

collinear with the laser polarization ϵ_γ . The emission angle can thus be expressed

$$\theta_i = \begin{cases} \arctan\left(\frac{R_i}{|L-t_i v_0|}\right), & (L-t_i v_0) > 0 \\ \pi - \arctan\left(\frac{R_i}{|L-t_i v_0|}\right), & (L-t_i v_0) < 0 \end{cases}. \quad (2.23)$$

The theoretically expected angular distribution of photofragments, emerging from a photon induced dissociation process of initially randomly oriented molecules was first stated by [Coo68, Zar72, Gre82]. For an electrical dipole transition and a molecular break-up, in which only one fragment is detected while neglecting the others, the distribution of emission angles is given

$$P(\theta, \phi) d\Omega = \frac{1}{4\pi} (1 + \beta P_2(\cos \theta)) d\Omega, \quad (2.24)$$

with $P_2(\cos \theta) = \frac{1}{2}(3 \cos^2 \theta - 1)$ being the second order Legendre polynomial. The solid angle can be expressed as $d\Omega = \sin \theta d\theta d\phi$, which transforms eq. (2.24) into

$$P(\theta) d\theta = \frac{1}{2} \left(1 - \frac{\beta}{2}\right) \sin \theta + \frac{3}{4} \beta \cos^2 \theta \sin \theta d\theta. \quad (2.25)$$

Under the assumption that the laser is polarized along the laboratory z -axis, i.e. collinear with the ion flight direction

$$\cos \theta = \hat{\mathbf{n}}_v \cdot \epsilon_\gamma = \cos \theta_{\text{cm}} \epsilon_{\gamma,z}, \quad (2.26)$$

and with $d \cos \theta_{\text{cm}} / d\theta_{\text{cm}} = \sin \theta_{\text{cm}}$, the angular distribution as a function of the emission angle θ_{cm} can thus be rephrased into

$$P(\theta_{\text{cm}}, \beta) d(\cos \theta_{\text{cm}}) = \left[\frac{1}{2} - \frac{\beta}{4} + \frac{3\beta}{4} \cos^2 \theta_{\text{cm}} \right] d(\cos \theta_{\text{cm}}). \quad (2.27)$$

A detailed discussion of the characteristic angular distribution for certain values of the asymmetry parameter β is given in sec. 2.3.

Cross section

The total cross section σ_{Ion} describes the probability of a photon-induced break-up reaction. Since the interaction point is not located in the focus of the FEL beam (c.f. sec. 3.2.1), it can be assumed that during the FEL pulse duration (70 fs) the

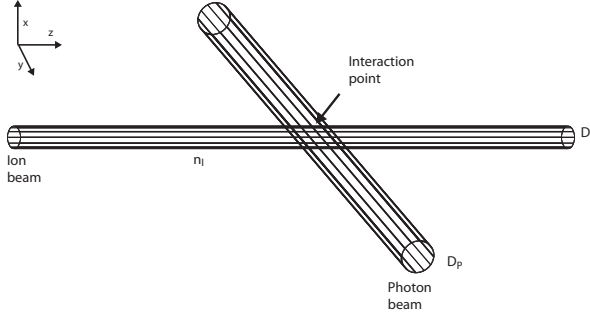


Figure 2.8: Illustration of crossed beams interaction point.

target density remains constant. Moreover, the forward motion of the ions can be considered as being frozen. The experimental observable, the number of events R_{Ion} of a certain ion species per FEL pulse, is linked in a crossed beams experiment to the total cross section via

$$R_{\text{Ion}} = \sigma_{\text{Ion}} N_{\gamma} n_I / \max\{D_I, D_P\}, \quad (2.28)$$

where $n_I = I/(v_0 q_I)$ represents the linear particle density and N_{γ} the number of photons per FEL pulse. For uniform, circular beam profiles the maximal height of either the ion or the photon beam has to be taken into account, see fig. 2.8.

In case of Gaussian shaped beam profiles of photon and ion beam, $g_I(x)$ and $g_P(x)$, a convolution factor F has been introduced [Ped09]

$$F = \int g_I(x) g_P(x) dx. \quad (2.29)$$

With the total number N_{Ion} of a certain fragment species, the absolute cross section for the production of that particular product can be determined according to

$$\sigma_{\text{Ion}} = \frac{N_{\text{Ion}}}{F} \sum_{n_S} (N_{\gamma} n_I), \quad (2.30)$$

where the sum extends over all signal cycles n_S .

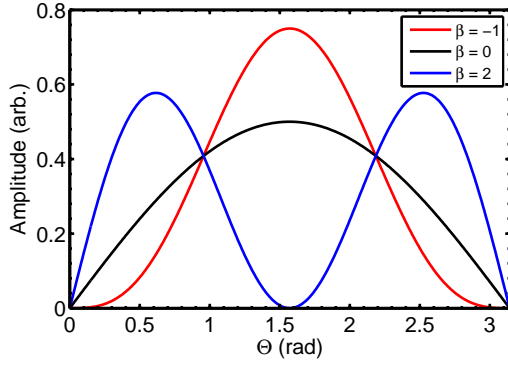


Figure 2.9: Computed photoelectron angular distribution for different β parameters.

2.3 Photoelectron detection with fast beams

2.3.1 Photoelectron angular distribution

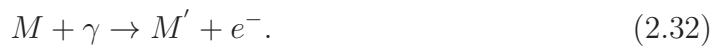
If one electron is ionized from a randomly oriented molecule, the distribution of emission angles of the photoelectrons relative to the laser polarization can be described, in analogy to eq. (2.27) by the formula [Coo68]

$$P(\tilde{\theta}, \beta) d(\cos \tilde{\theta}) = \left[\frac{1}{2} - \frac{\beta}{4} + \frac{3\beta}{4} \cos^2 \tilde{\theta} \right] d(\cos \tilde{\theta}). \quad (2.31)$$

Here, $\tilde{\theta}$ represents the emission angle relative to the laser polarization (here $\mathbf{e}_\gamma = \mathbf{e}_x$, c.f. fig. 2.10), where $\beta \in [-1; 2]$ is the anisotropy parameter. In fig. 2.9 the distribution of the emission angles for characteristic values of the asymmetry parameter β are shown. For ($\beta = -1$) the photoelectron is preferably perpendicular ejected to the laser polarization, whereas ($\beta = 2$) yields an emission along the polarization.

2.3.2 Photoelectron velocities

The discussion in the previous section, is based on the fact that the target is at rest during the photoelectron emission, i.e. eq. (2.31) describes the angular distribution of the photoelectrons in the center-of-mass frame. Now, the kinematics of the photoionization process of a moving anionic, neutral or cationic target M is considered



Depending on the charge state of the target, a neutral, singly or doubly negatively charged molecule M' is formed. The ion beam propagates with v_0 along the labo-

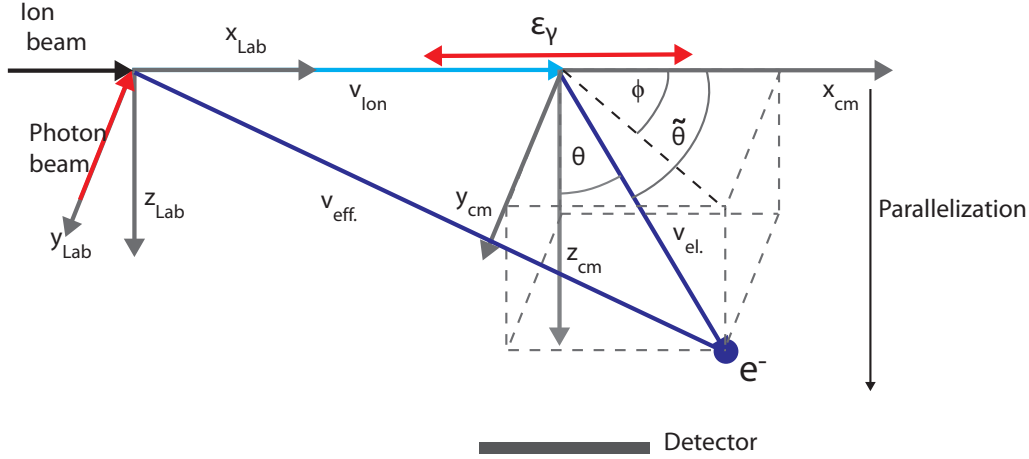


Figure 2.10: Definition of angles and vectors, which are introduced to describe the detachment process on a moved target. A complete account for the whole setup is given in fig. 3.21.

ratory x -axis. The coordinate system indicated in fig. 2.10 is chosen such that the laboratory z -axis is collinear with the axis of rotational symmetry of the employed electron spectrometer (c.f. sec. 3.2) and the detection unit lies in the $x - y$ -plane of the respective device. An electron is assumed to appear in the center of mass frame with a certain kinetic energy $E_{(\text{cm},e)}$.

The fast motion of the ions modifies the observable electron energies in the laboratory frame by a Doppler shift that depends explicitly on the angle of emission relative to the ion motion. The momentum of the photon with respect to that of the ion can be neglected (i. e. $E_\gamma/(m_i v_i c) \approx 0$). A photoelectron emitted from the target, propagating at speed $\vec{v} = v_0 \mathbf{e}_x$ emerges with a total laboratory velocity $\vec{v}_{(e,\text{lab})}$ given by

$$\vec{v}_{(e,\text{lab})} = v_0 \mathbf{e}_x + v_e \begin{pmatrix} \sin \theta \cos \phi \\ \sin \theta \sin \phi \\ \cos \theta \end{pmatrix}, \quad (2.33)$$

which can be rephrased into

$$\vec{v}_{(e,\text{lab})} = v_0 \mathbf{e}_x + v_e \hat{\mathbf{n}}_e = v_e^\perp + v_e^\parallel, \quad (2.34)$$

with $v_e = \sqrt{2E_{(\text{cm},e^-)}/m_e}$ and $\hat{\mathbf{n}}_e = \sin \theta \cos \phi \mathbf{e}_x + \sin \theta \sin \phi \mathbf{e}_y + \cos \theta \mathbf{e}_z$ being the unit vector in the direction of electron emission in the rest frame of the target. θ and ϕ represent the inclination and azimuth angles of the spherical coordinate system.

With the present definition of the coordinates, v_e^\perp lies in the $x - y$ -plane and v_e^\parallel is parallel to the z -axis, i.e. points towards the detection unit.

Time-of-flight observation

The parallelization describes the process where the momentum vector of the detached electron is bent towards a detector unit, indicated in fig. 2.10. For both devices, the magnetic-bottle and saddle-point spectrometer, the detector is at a distance L from the interaction point symmetrically arranged around the z -axis. A detailed description of both devices is given in sec. 3.2.2. In the following the parallelization process for a magnetic bottle spectrometer is described, but the concept can also be partly applied for the saddle-point electron spectrometer (see end of this section).

In an idealized representation of a magnetic bottle spectrometer all photoelectrons are instantaneously parallelized, while maintaining their kinetic energy. In this step, the transverse momentum mv_e^\perp with $v_e^\perp = \sqrt{v_i^2 + v_e^2 \sin^2 \theta + 2v_i v_e \sin \theta \cos \phi}$ is transferred by the magnetic field into longitudinal momentum towards the detection unit, a process known as parallelization [Kru83].

The effective velocity in the laboratory frame after the parallelization is given

$$v_{\text{eff}}^\parallel = \sqrt{(v_e^\parallel)^2 + (v_e^\perp)^2} = \sqrt{v_i^2 + v_e^2 + 2v_i v_e \sin \theta \cos \phi}. \quad (2.35)$$

Moreover, since the laser is horizontally polarized $\epsilon_\gamma = (1, 0, 0)$ the ejection process can be described by $\tilde{\theta}$ the electron emission angle with respect to the laser polarization (see fig. 2.10) according to

$$\epsilon_\gamma \cdot \hat{\mathbf{n}}_e = \sin \theta \cos \phi = \cos \tilde{\theta}. \quad (2.36)$$

The time-of-flight of a photoelectron towards a detector can thus be written as

$$t = L / \sqrt{v_i^2 + v_e^2 + 2v_i v_e \cos \tilde{\theta}}, \quad (2.37)$$

with L being the total distance from the interaction point to the detector. Finally, combining eqs. (2.31) and (2.37), the following formula for the photoelectron time-

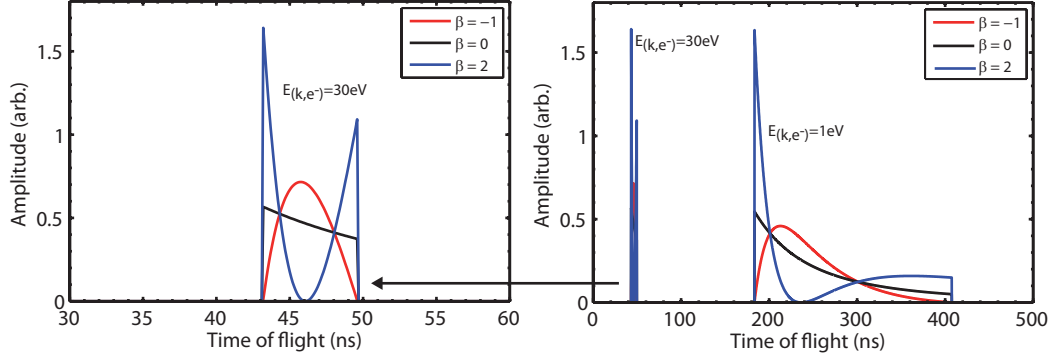


Figure 2.11: Time of flight distribution computed according to eq. (2.38) for different β parameters and an electron with kinetic energy of $E_{(k,e)} = 30$ eV and $E_{(k,e)} = 1$ eV, ionized from a target propagating with a velocity $v_0 = 232$ mm/ μ s along the laboratory x -axis.

of-flight distribution as a function of the asymmetry parameter β can be derived:

$$\begin{aligned}
 P(t, v_e, v_i, \beta) dt = & \\
 & \frac{1}{2} \left[1 - \frac{\beta}{2} + \frac{3\beta}{8} \left(\frac{v_e}{v_i} \right)^2 \left[1 + \left(\frac{v_i}{v_e} \right)^2 - \left(\frac{L}{tv_e} \right)^2 \right]^2 \right] \\
 & \times \frac{v_e}{v_i} \left(\frac{L}{tv_e} \right)^3 \frac{v_e dt}{L}, \quad (2.38)
 \end{aligned}$$

which was published in [Dom10]. The idealized eq. (2.38) is only defined on the interval $t \in [L/(v_e + v_i); L/(v_e - v_i)]$ and zero elsewhere. The total temporal width where the distribution is non-zero is given by

$$w = \frac{2L \times \min(v_i, v_e)}{|v_e^2 - v_i^2|}. \quad (2.39)$$

As mentioned, eq. (2.38) relies on the assumptions of complete and instantaneous parallelization and on the laser being horizontally polarized (i.e. $\epsilon_\gamma = \mathbf{e}_x$). Eq. (2.38) shows explicitly, how the time-of-flight distributions of photoelectrons map both the electron energy by the temporal range covered and the emission anisotropy by the shape of the distribution. Fig. 2.11 displays the time-of-flight distributions for characteristic values of the asymmetry parameter and two different electron energies of $E_{(k,e)} = 30$ eV and $E_{(k,e)} = 1$ eV. The detection unit is located 0.15 m away from the interaction point. An isotropic distribution ($\beta = 0$) appears as a decreasing t^{-3} function between two sharp edges (black curve in fig. 2.11). The distribution

corresponding to ($\beta = 2$) shows a minimum between the two edges (blue curve in fig.2.11) and finally ($\beta = -1$) leads to a distribution which is zero at the edges and reveals a maximum in between.

In case of the electrostatic spectrometer, the saddle-point potential bends the momentum vector of the photoelectrons towards the detection unit. To ensure an effective parallelization process, a certain depth of the saddle-point is required. Therefore, the electrons gain additional kinetic energy due to the saddle-point potential (c.f. sec.3.2), i.e. the kinetic energy is not preserved during the bending process. Considering the bending process as ideal and including an additional energy qU_S due to the saddle-point potential, i.e. assumes an infinitesimal saddle-point region, the following expression for the electron velocity can be derived (c.f. sec.3.2)

$$t = L_{\text{eff.}} / \left(\sqrt{(v_{\text{eff.}}^{\parallel})^2 + \frac{2qU_S}{m_e}} \right). \quad (2.40)$$

Here, the effective drift length $L_{\text{eff.}} = L + \Delta L$ accounts for oversimplifying assumption of an infinitesimal saddle-point region, since it takes the electron a certain time to leave interaction region (see sec.3.2).

Chapter 3

Experimental technique

3.1 Trapped Ion Fragmentation setup at FLASH (TIFF)

The upcoming sections give an overview on the basic elements and concepts which are used at the fast ion beam infrastructure TIFF. With the advent of the Free electron Laser light sources like FLASH (**F**ree **E**lectron **L**ASer in **H**amburg), a basically unexplored wavelength range delivered by these machines, opens the way to a completely new type of experiments. The photon flux of FEL light sources exceeds the one of synchrotron radiation sources by orders of magnitude, hence allowing for studies on extremely dilute targets. To investigate photofragmentation processes of molecular ions after valence shell excitation or ionization, the crossed beams ion beam infrastructure TIFF was set up in 2005 and successfully brought in operation in 2007 [Ped07]. The fast beam method was chosen to obtain, besides the charged fragments also the neutral break-up products. The kinetic energy of 2 – 8 keV yields for most of the studied singly charged molecular targets an energy of at least $\frac{50 \text{ eV}}{\text{Nucleon}}$. Thus, the fragments travel on a forward explosion cone around the mother beam. In addition, the kinetic energy of the ions still allows that the beam can be controlled via electrostatic elements, like Einzel lenses and quadrupoles. By this, TIFF offers versatile possibilities in terms of target preparation, but still keeps the set up rather compact.

A schematic drawing of the TIFF setup is shown in fig. 3.1. The ions are produced with a hollow cathode ion source on a platform potential of 4.2 keV. After the source, the ion species of interest is separated from the main beam by a separator magnet, which bends the separated beam towards an ion trap. The trap allows for the possibility to store the ion beam for several seconds to vibrationally cool the target

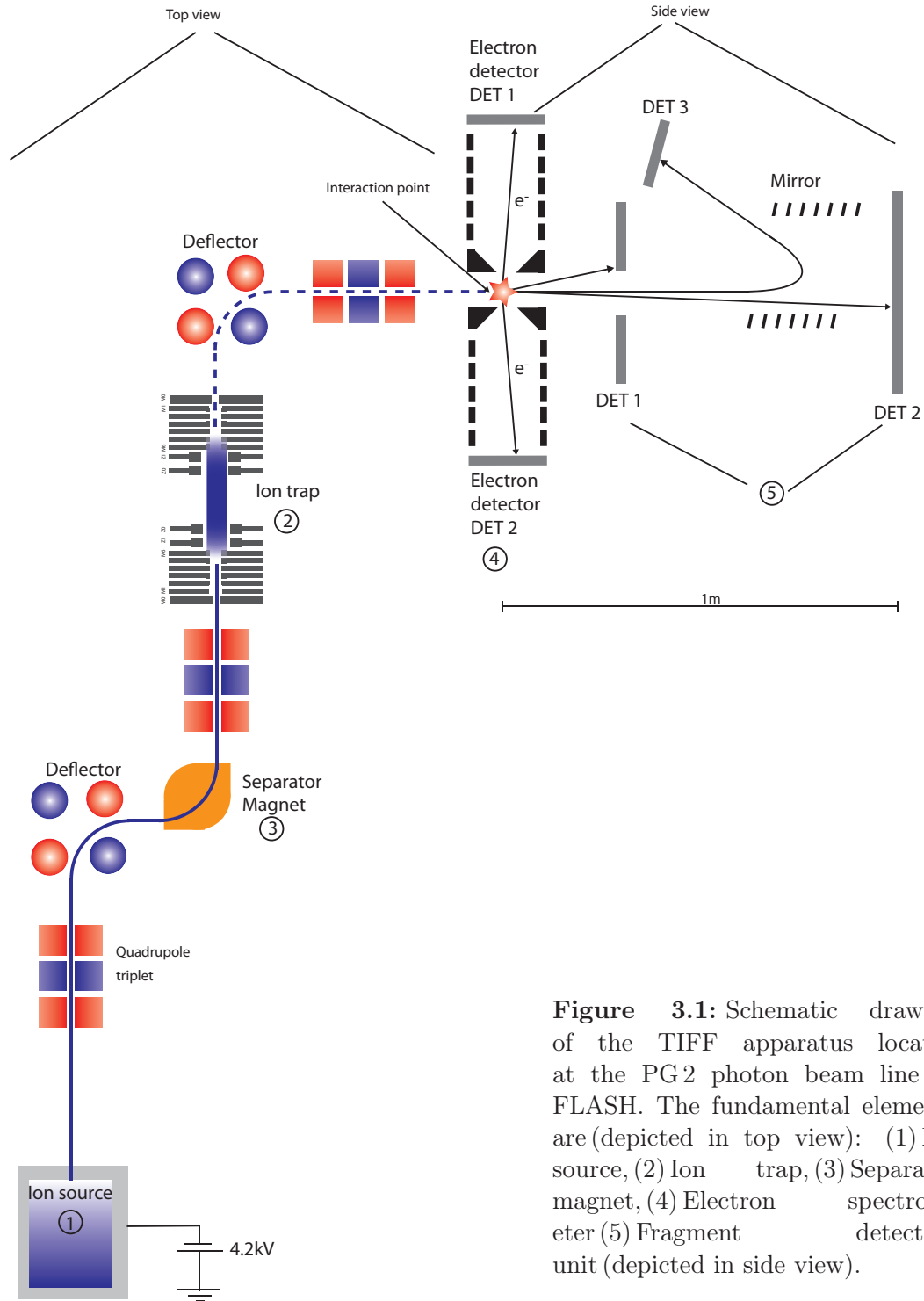


Figure 3.1: Schematic drawing of the TIFF apparatus located at the PG2 photon beam line at FLASH. The fundamental elements are (depicted in top view): (1) Ion source, (2) Ion trap, (3) Separator magnet, (4) Electron spectrometer (5) Fragment detection unit (depicted in side view).

prior to irradiation. In a direct transfer mode, the trap is used to chop the DC beam

in bunches of $1\,\mu\text{s}$ length and in addition to match these bunches in time with the FEL light propagating through the interaction region.

With another quadrupole deflector the ion beam is then bent on the part of the beam line, where the interaction region the electron- spectrometer and fragment detection system is situated. Within the inner part of the electron spectrometer the ion and photon beams are crossed perpendicularly. Under ideal conditions the interaction point is in the saddle point of the electron spectrometer. The saddle point potential leads to a parallelization of the electron momentum vector towards the position sensitive electron detectors. The trajectory of the fragments is unaffected by the saddle-point. Thus, after leaving the interaction region the forward explosion cone of the fragments is intersected with the cylindrical symmetric serial arrangement of the fragment detectors around the ion beam axis. Both detectors allow for a time and position sensitive analysis of each fragment impact. The first detector with a central hole of 10 mm radius is sensitive to all charged and neutral fragments which are emitted with sufficient transversal momentum. Behind the first detector (DET 1) the main beam and all charged fragments, which escaped from detection are deflected towards a beam dump. Thus, only neutral fragments can reach the second detector (DET 2).

During the upgrade of TIFF in summer 2011 a new heavy charged fragment detection system was installed between DET 1 and DET 2. Here, all heavy charged break-up products, which were up to now lost for detection on DET 1 enter a set of electrostatic mirrors and are deflected towards a third non position sensitive multi-channel plate detector. The entire detection unit for the fragments, as well as for the electrons, allows for full coincident data acquisition on an event by event basis. In the following paragraphs the different elements of the TIFF apparatus are introduced in more detail.

3.1.1 Hollow cathode ion source

For both experiments, using the optical and the free-electron-laser respectively, the ions are produced with a hollow cathode ion source. During operation the source is lifted on a platform potential of 4.2 keV. The discharge power supply applies a potential drop over the gap between anode and cathode. With a controllable valve, water vapor is leaked into the ion-source. By this, the typical pressure inside the source is increased up to 1.5 Torr. Before the plasma is initiated the resistance of

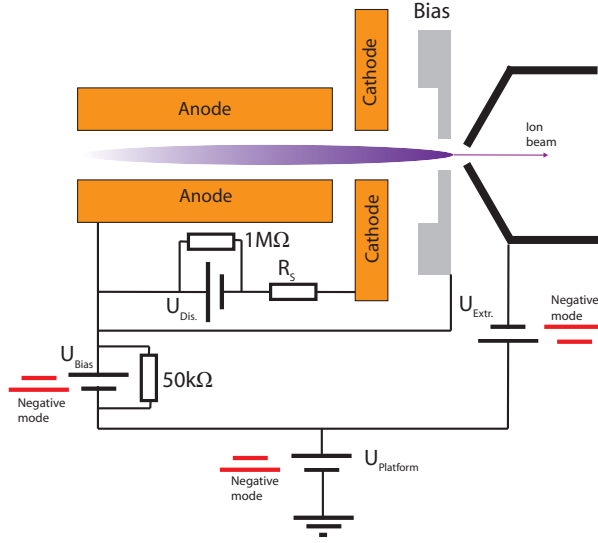


Figure 3.2: Schematic illustration of the ion source and electrical connections. In negative mode (anion production) the polarity of the platform-, extraction- and bias-power supply is changed.

the water vapor in the source, which also fills the gap between anode and cathode, is much larger than R_s . Once the plasma is lighted the resistance between anode and cathode dramatically decreases and R_s serves as a base load for the discharge power supply. In order to establish a potential well to ensure a diffuse motion of the ions inside the source the bias electrode is kept on the platform potential. A large fraction of the ions is mainly produced within the negative glow of the discharge [Alt03]. With the extraction potential of $U_{\text{Ext.}} \approx 3 \text{ kV}$, the ions are pre-accelerated and pre-focused. The potential on which the ions are generated inside the discharge is expressed by U_{Ion} . It can be shown that $U_{\text{Ion}} \approx U_{\text{Anode}}$, which yields in our case $U_{\text{Ion}} \approx 4.2 \text{ keV}$.

Ion yields

After the source, the integrated ion beam with a current of about $1.5 \mu\text{A}$, is guided towards a mass separating magnet. The charge to mass ratio is obtained via the following relation:

$$\frac{m}{q} = \frac{r^2 B^2}{2 U_{\text{Platform}}}, \quad (3.1)$$

where B denotes the magnetic field inside the separator magnet typically ranging from 0 – 500 mT. To obtain the mass spectra for a certain setting of the source, the magnetic field is swept through its range and simultaneously the ion current on a Faraday cup after the magnet is recorded. In fig. 3.3, the ion yield is shown when the source is operated in positive mode. If one assumes within the discussed mass

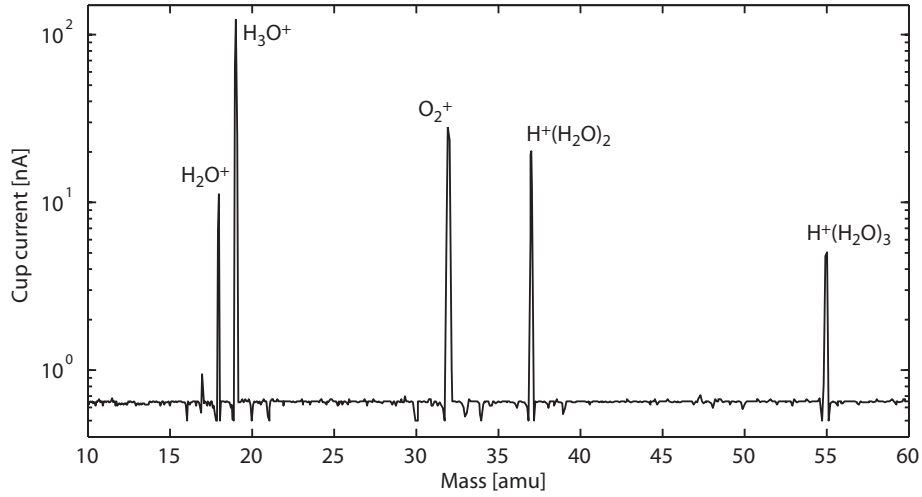


Figure 3.3: Mass scan taken for cations, when source was operated in positive mode.

range the transmission of the beam line to be equal, the observed ionic species can be assigned to stem from singly charged ions with the mass of $(\text{H}_2\text{O})\text{H}_{n=1..4}^+$, $(\text{H}_2\text{O})^+$ and O_2^+ , respectively.

For the negative mode of operation fig. 3.4 displays the yield of the anion production. The dominating species for these conditions can be addressed to originate from O^- , OH^- , F^- and O_2^- .

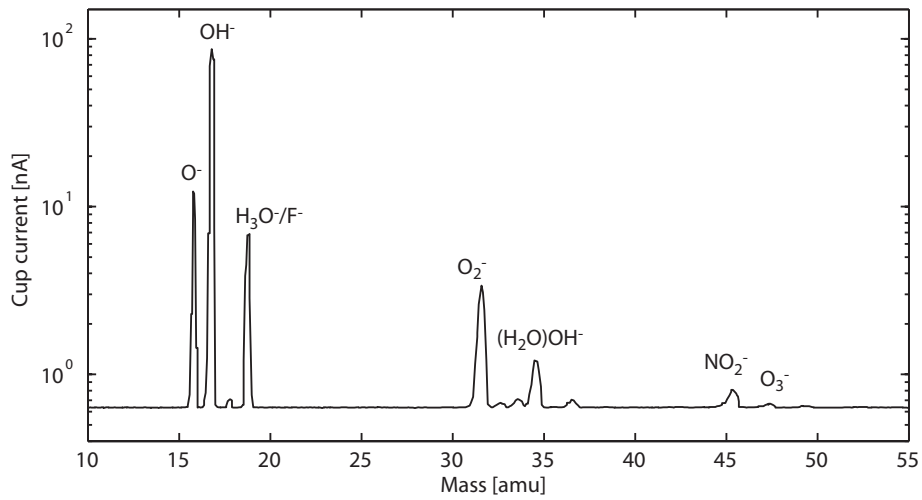


Figure 3.4: Mass scan taken for anions, when source was operated in negative mode.

Electrostatic ion trap

In order to vibrationally cool the ions prior to irradiation an electrostatic ion trap is implemented in the TIFF beam line. The system was constructed in analogy to the first ion-trap of this kind built by D. Zajfman et al. [Zaj97]. A detailed description of the technical aspects of the ion trap, and how to operate the system, are given in [Alt07]. Each side of the trap consists of a set of seven cylindrical symmetric electrostatic mirrors M0-M6 and two Einzel lens electrodes Z0-Z1. During operation the barrier imposed by electrode M1 has to be sufficient to inverse the motion of the ions along the trap axis. For a beam energy of 4.2 keV, M1 is set to $V_{M1} = 4600$ V and the potential is linearly divided among the electrodes M2-M5 to induce a gradient towards electrode M1. The electrodes M6 and M0 are grounded to reduce the stray field outside the trap. For field free propagation of the charged particles inside the resonator Z0 is also kept on ground potential. Depending on the mode of operation, Z1 is set to a potential ranging from 3200 – 4800 V. In addition the entrance and exit mirrors M1 are connected to two independently switchable power supplies, with typical potentials for high and low level of $V_{M1,low} = 2.8$ kV and $V_{M1,high} = 4.2$ kV. When the lower voltage is for instance applied to the mirror plates they are transparent for the beam and ions can either be loaded or extracted from trap. After the upgrade of FLASH, a bunch train, constituting of fifty bunches at a repetition rate of 200 kHz can be delivered. To meet such a time structure with the extracted ion bunches the switchable power supply on the exit of the trap had to be adapted such that a reasonable stability of the high and low level and a fast transition of about 100 ns between the levels was still given.

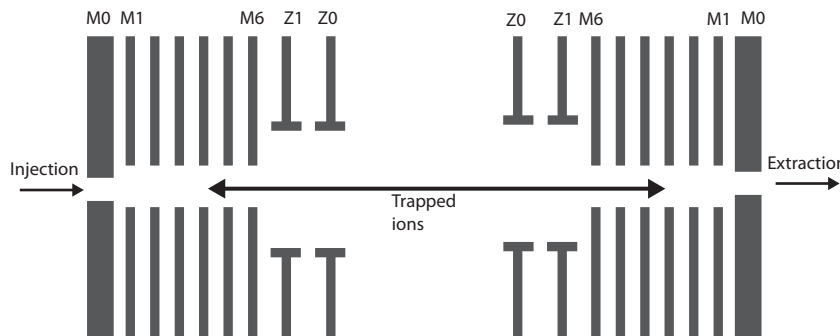


Figure 3.5: Schematic drawing of ion trap, adapted from [Dah97].

Beam steering

At TIFF and TIFF jr. two different types of electrostatic elements are used to steer and to focus the ion beam along the beam line. One set consists of a combination of an Einzel lens with horizontal/vertical deflection plates.

The second element comprises a serial arrangement of three electrostatic quadrupoles. For every quadrupole module the opposing electrodes have the same, whereas neighboring ones have alternating polarity. Thus, each quadrupole element defines the

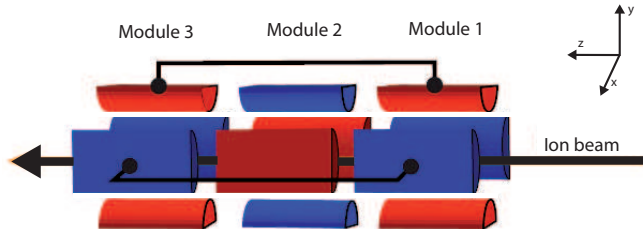


Figure 3.6: Schematic of quadrupole triplet unit and electrical wiring [Alt07].

focus in either the x- or y-plane. For that device, the ability to steer the beam is implemented by the possibility to apply a slightly asymmetric potential to facing electrodes of the third module. The gradient resulting from such a configuration allows deflecting the ion beam along the particular direction. In fig. 3.6 a schematic of the quadrupole triplet unit with the realized electrical wiring is shown.

3.1.2 Fragment detection system

The fragment detection unit before the upgrade is depicted in fig. 3.7. The ring-shaped detector for light fragments DET 1 consists of a MCP stack in chevron configuration with a specially designed delay line anode [Spi01]. The central hole has a radius of $r_H = 10$ mm and the overall radius of the MCP is $r_D = 40$ mm. The active area of the MCP of DET 1 is covered by three delay line layers with a relative angle of 60° around the central hole. For field free propagation of the mother beam through the central hole an insulating tube with a grounded metallic layer on the inside shields the stray field emerging from the potential applied to the delay lines. As a consequence of the geometrical boundaries of the detector and its distance from the point of interaction, charged and neutral fragments emitted in the explosion cone of $(38 \geq \theta_F \geq 150 \text{ mrad})$ are mapped on DET 1.

The second detector also consists of a MCP stack in chevron design. The active area is covered by two delay line layers with a relative angle of 90° . Since all charged

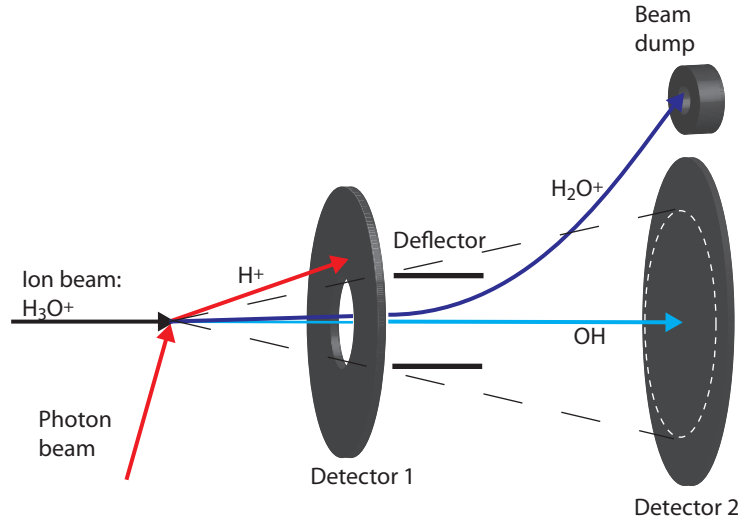


Figure 3.7: Schematic drawing of the fragment detection unit before the upgrade. The ring shaped detector is sensitive to all neutral and charged fragments, emitted in an explosion cone with ($38 \geq \theta_F \leq 150 \text{ mrad}$) opening angle. The second detector is fully sensitive to all neutral fragments emitted with a solid angle of $0(\geq \theta_F \leq 38 \text{ mrad})$.

particles are deflected towards a beam dump the second detector is only sensitive to neutral fragments emitted within a cone of $0(\geq \theta_F \leq 38 \text{ mrad})$. The position sensitivity is described in more detail in sec. 3.3.

3.1.3 New heavy charged fragment analyzer

The serial arrangement of the ring shaped detector (DET 1) and the normal second detector (DET 2) allows, due to geometrical limitations, only for the detection of ionic fragments which are released with a certain transversal momentum, i.e. most of the heavy charged fragments are lost for detection. One approach to compensate for that deficiency is the use of a set of reflective electrostatic mirrors. For a given kinetic energy per nucleon of the incident beam, the different mirror plates can be biased in a way that they are transparent for the parent beam, but reflect ionic fragments of a certain charge to mass ratio towards a third detector (DET 3).

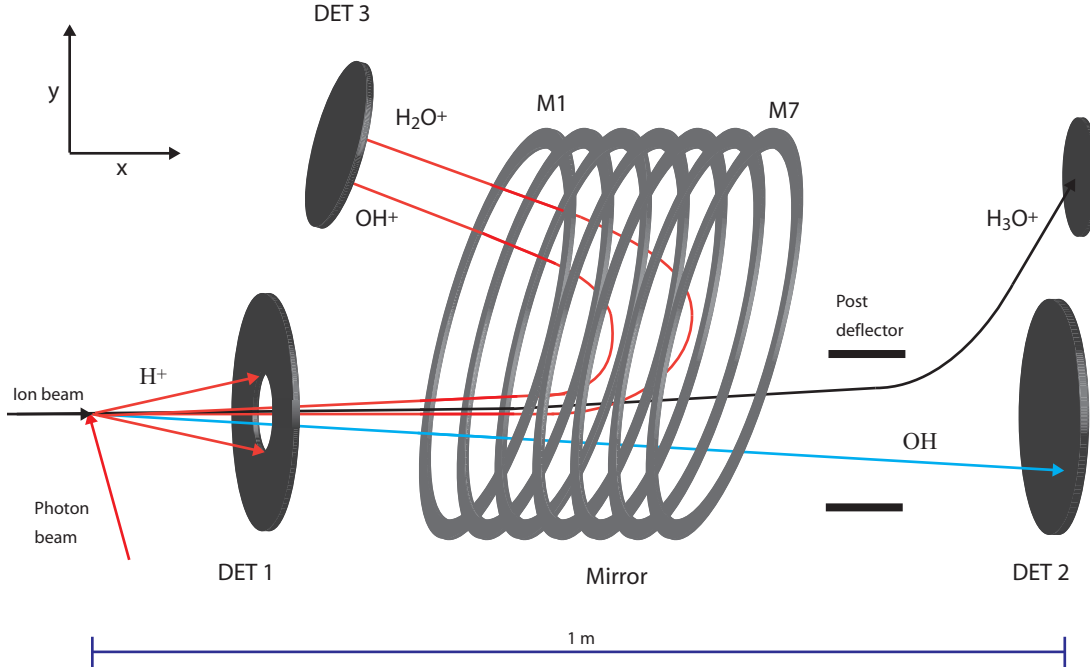


Figure 3.8: Illustration of new detection unit, with pre- and post-deflector and electrostatic mirror. The pre-deflector is used to steer the parent ion-beam into the mirror system. The post deflector steers the unreacted ion-beam towards the beam dump.

Technical aspects

The kinetic energy of the ion beam at TIFF ranges from 2 – 8 keV. Thus, to ensure a wide dynamic range of operation, the mirror has an inner diameter of 210 mm, where the plates are spaced by 18 mm and insulated with ceramic tubes. Each of the mirror plates, M1 – M7, can be individually biased with a potential in the range of 0 – 6 kV. The pre- and post-deflector units are used to steer the beam into the mirror. All elements are situated within a CF 300 vacuum chamber which is directly attached to the TIFF beam line. In the first phase, the system was equipped with a non-position sensitive multi-channel plate detector with 40 mm diameter, although the openings of the entrance and exit grids have a diameter of 80 mm to work with a larger detector to be installed for the upcoming beam-time.

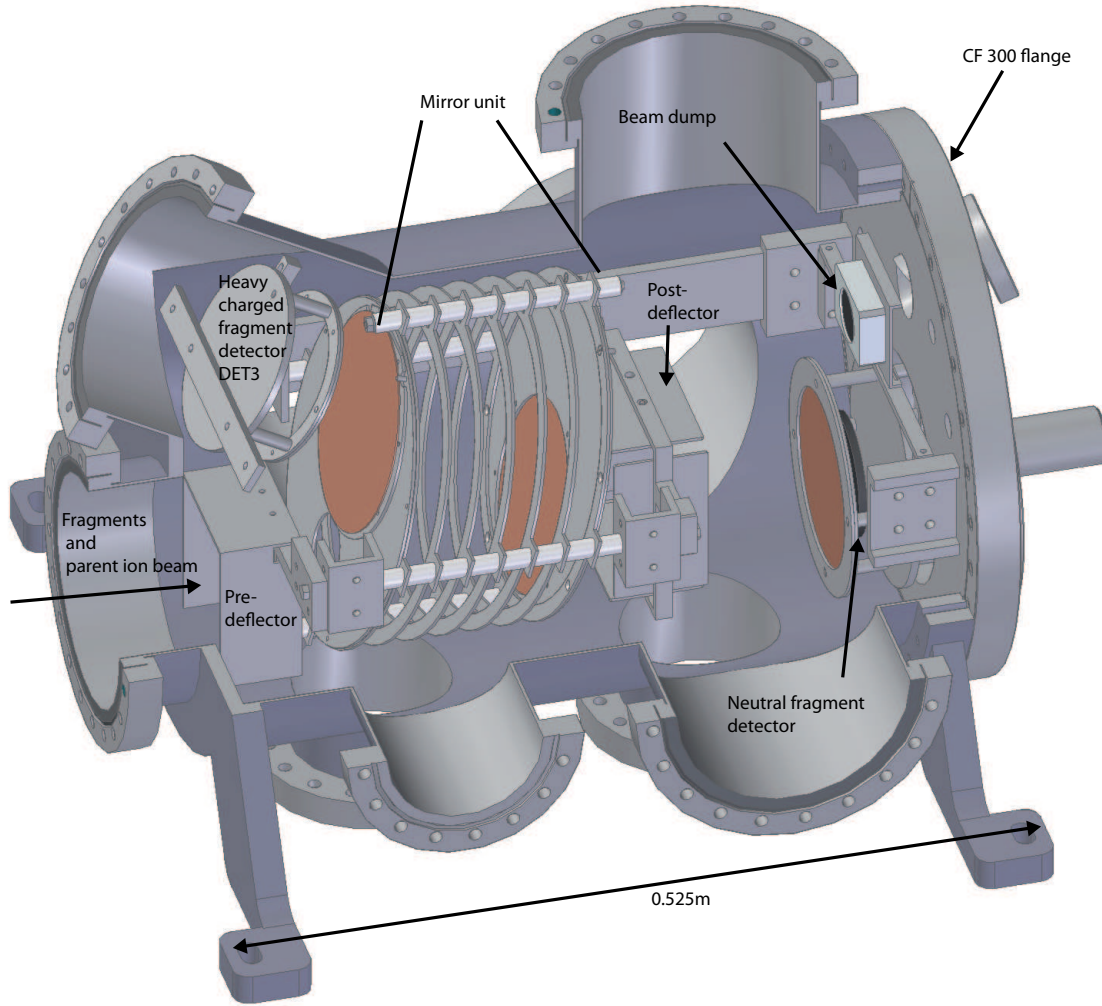


Figure 3.9: Technical drawing of CF 300 vacuum chamber with the different components inside. The key elements, like pre- and post-deflector mirror-unit and the detectors are directly mounted on the CF 300 flange.

Performance

The complete mirror unit including the pre- and post-deflector is modeled with SIMION. For the optimal design of the system the performance of the mirror, i.e. the transmission as a function of the kinetic energy release of the break-up, but also the kinematical properties are extracted from a SIMION based Monte Carlo simulation. In fig. 3.10 the transmission of the system for different kinetic energy releases of an ionic fragment (H_2O^+), emerging from a two body break-up of H_3O^{++} is shown. Emission processes preferably along the ion beam axis ($\beta = 2$) are mapped with the

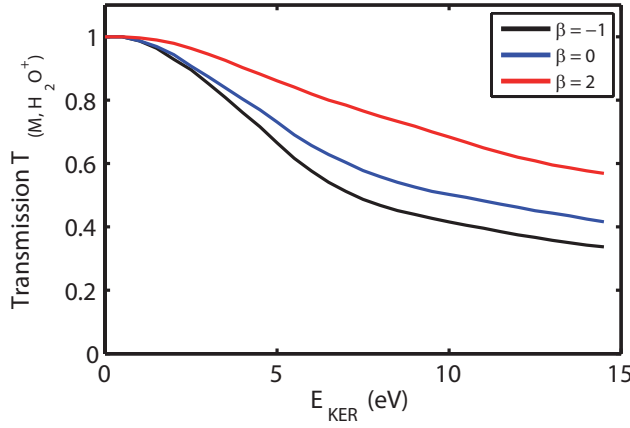


Figure 3.10: Simulated transmission of mirror system for different energy releases of two body break-up $\text{H}_3\text{O}^+ \rightarrow \text{H}_2\text{O}^+ + \text{H}^+$.

best transmission on DET 3. Even for a kinetic energy release of 10 eV about 70 % of the fragments can still reach the Detector. For $(\beta < 2)$ the transmission is somewhat worse since the widening of the explosion cone yields that more and more particles can still propagate through the mirror, but miss the detector. As mentioned above, DET 3 is only an intermediate detector. The appropriate, position sensitive detector, for which the mirror is optimized for, will be installed and used in upcoming beam times.

As illustrated in sec. 2.2.1, under ideal conditions the longitudinal and transversal momentum in the center of mass frame are preserved. In fig. 3.11 the longitudinal momenta of H_3O^+ and H_2O^+ fragments emerging from a two body break of $\text{H}_5\text{O}_2^{2+}$ with an kinetic energy release of 2 eV are shown. For the ideal case the events appear on a straight line with a negative slope, see fig. 3.11. In comparison, the events which passed through the mirror are shown in the left of fig. 3.11. To model the dispersion

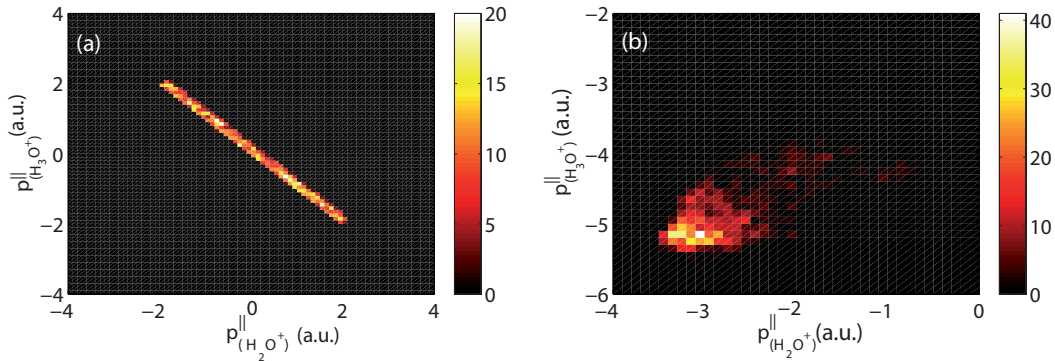


Figure 3.11: Longitudinal center-of-mass momentum sharing between the fragments emerging from a two body break-up of $\text{H}_5\text{O}_2^{2+} \rightarrow \text{H}_3\text{O}^+ + \text{H}_2\text{O}^+$. The ideal case is shown in (a) and (b) displays the situation for events which passed the mirror.

of the mirror an effective drift length has to be used. Therefore the events appear not centered around the zero point of the two-dimensional scatter plot. Moreover, due to the focusing of the mirror, longitudinal and transversal momentum are mixed, leading to a distorted kinematical correlation. A detailed investigation of this effect will be performed once the new position sensitive detection unit is installed.

3.2 Electron spectrometer

One important question to address with the dissociative photoionization is the kinetic energy of the photoelectron which is in the initial step ionized from the molecular system. In the upcoming section two different types of electron spectrometer devices are presented. At first, the conceptually new saddle-point electron spectrometer is introduced and in the second part the functioning of a magnetic bottle spectrometer will be illustrated.

3.2.1 Saddle point electron spectrometer

Doing photoelectron spectroscopy measurements under xuv conditions is a challenging task with respect to many aspects. In the wavelength range of 13.5 – 30 nm, the photon energy is larger than the ionization potential of the different constituents of the residual gas. Hence, one major problem arises from background electrons induced by the photoionization of the residual gas while the FEL light propagates through the spectrometer. One aspect for the design of the new spectrometer is to suppress the rest gas induced electrons, i.e. to confine the acceptance volume of the spectrometer to a small volume around the interaction point.

General layout

The saddle-point spectrometer is an electrostatic device where the parallelization and stabilization of electron motion towards the detection unit is sustained via electrostatic fields. In fig. 3.12 the side view of the spectrometer is shown. The spectrometer electrodes can be classified in the center unit, the ion trap and the drift unit. The interaction point of the photon- and ion-beam is located in the center of the spectrometer. The four electrodes of the central unit determine the shape and consequently the acceptance volume of the spectrometer. The spectrometer obeys

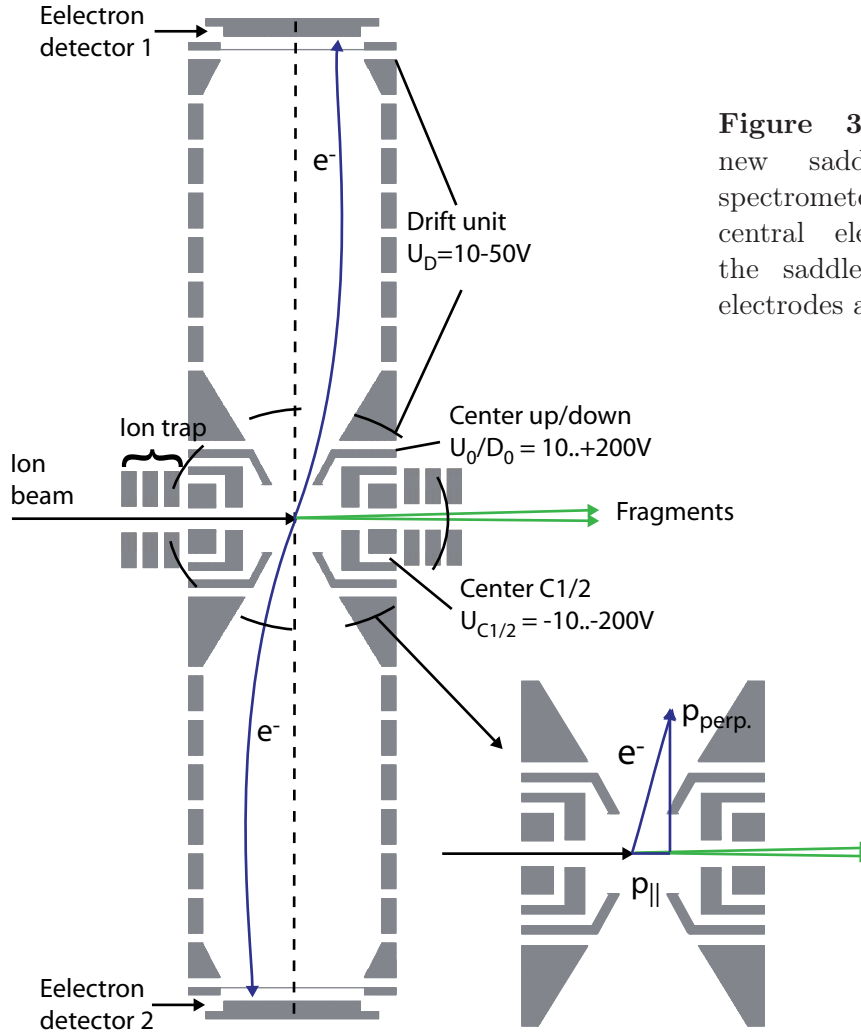


Figure 3.12: Schematic of new saddle-point electron spectrometer for FLASH, with central electrodes to form the saddle point, ion trap electrodes and drift unit.

two symmetries, one rotational symmetry along the vertical spectrometer axis and a mirror symmetry on the plane, defined by the incoming photon and ion beam, respectively. The detection system on the top and the bottom of the spectrometer comprises two multi-channel plate detectors with delay-line anodes for position sensitivity.

Ion trap

One outstanding feature of the device is the capability to trap ions on orbits crossing the interaction point which allows for instance to probe the lifetime of the trapped particles by observing the decay of the electronic signal.

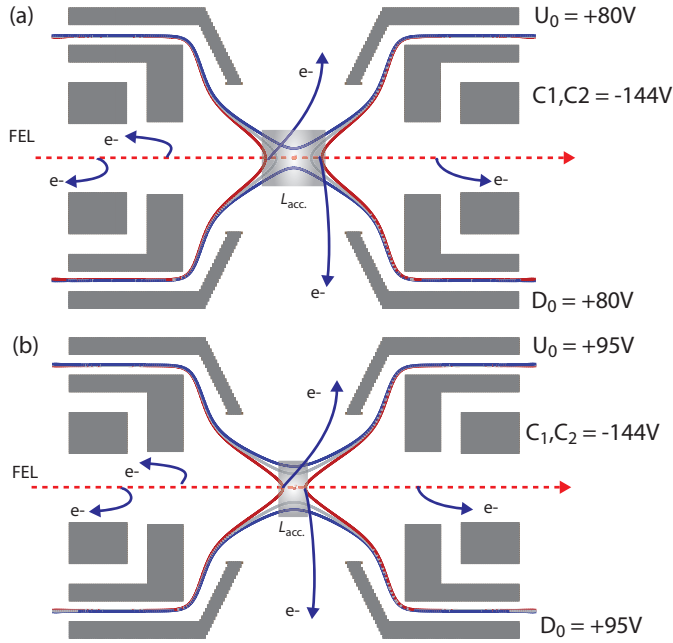


Figure 3.13: Saddle point for fixed potential of $C_1, C_2 = -144$ V as a function of U_0, D_0 . (a) 80 V. (b) 95 V. Contour depicted for: Red -35 V; Gray -30 V; Blue -25 V. The gray shaded area illustrates the acceptance volume of the spectrometer.

Saddle point mode of operation

When the center electrodes of the spectrometer are kept on ground potential only those electrons emitted in the direction of the multi-channel plates are detected. If one assumes an isotropic emission, the fraction $2 \cdot \frac{\Omega_{Spec}}{4\pi} \approx 0.1$ of the total number of electrons can reach the detection unit. In normal saddle point mode of operation C_1/C_2 is biased with $-10 \dots -200$ V and U_0/D_0 with $+10 \dots +150$ V. In fig. 3.13 the side view on the saddle point is shown. Here the potential of U_0/D_0 is varied from $+80$ V (fig. (a)) and $+95$ V (fig. (b)). By this, the depth of the saddle point and consequently the acceptance volume, indicated by gray shade areas, is influenced. Since the spectrometer exhibits rotational symmetry along the vertical spectrometer axis, the momentum vector of an emitted electron can be separated in a parallel p_{\parallel} and a perpendicular component p_{\perp} (c.f. sec. 2.3.2). For a given electron energy E_e the depth of the saddle point has to be chosen such that the perpendicular momentum component is bent towards the detectors. An effective parallelization process requires the electrons to be created within a certain acceptance volume, i.e. the electrons which are induced by the ionization of residual gas molecules outside the spectrometer are not effectively bent towards the detectors and are thus rejected.

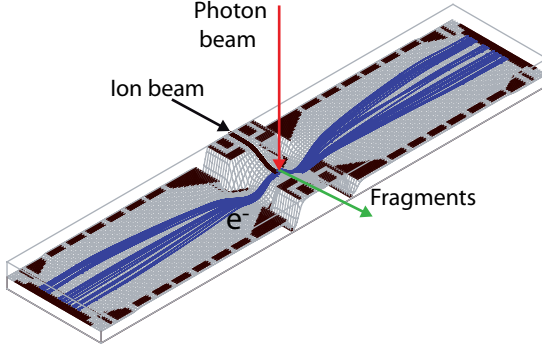


Figure 3.14: Potential landscape for spectrometer operated in saddle-point mode.

Biased interaction region

Besides the normal spectrometer operation the central unit can be biased ($C_1 = C_2 = U_0 = D_0 = U_C$) such that the parent beam and hence the charged fragments have to overcome a potential barrier. If one neglects the extend of the interaction region, the velocity of the mother beam and the neutral fragments at the interaction point is thus given by

$$v_{neutral}^{\parallel} = \sqrt{v_0^2 - (2q/m)U_B}. \quad (3.2)$$

Here, U_B states the depth of the barrier. The polarity of the barrier potential U_B and the charge state of the break-up products define whether the fragment gains or loses energy while leaving the biased interaction zone. Hence, the velocity of the charged fragments after the interaction zone depends on their charge to mass ratio

$$v_{charged}^{\parallel} = \sqrt{v_0^2 - (2q/m)U_B + 2 \frac{q_F}{m_F} U_B}. \quad (3.3)$$

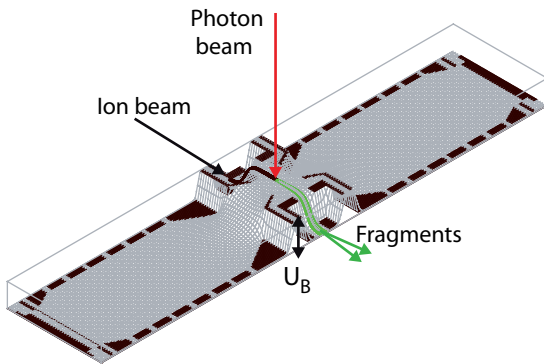


Figure 3.15: Potential landscape for biased interaction region.

Drift unit

After the momentum vector of the electrons is parallelized they enter the drift unit of the spectrometer (c.f. fig. 3.16). In order to sustain the motion of the electrons along

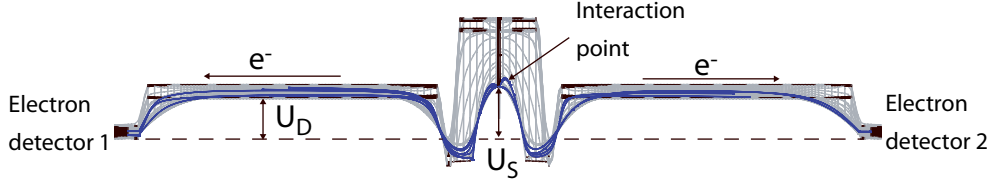


Figure 3.16: Potential landscape of spectrometer (side view) when operated in saddle-point mode and a retardation potential U_D is applied to drift-unit.

the spectrometer axis a potential of typically $U_D = -10 \dots -50 \text{ V}$ is applied to these electrodes. In sec. 2.3, it has been shown that for an idealized parallelization process the effective velocity, v_{eff} of a photoelectron emerging from a ionization process on a moved target, explicitly depends on the emission angle of the electron relative to the laser polarization. If one assumes in the present discussion an idealized parallelization process, the velocity of the electrons once they have reached the drift unit is given

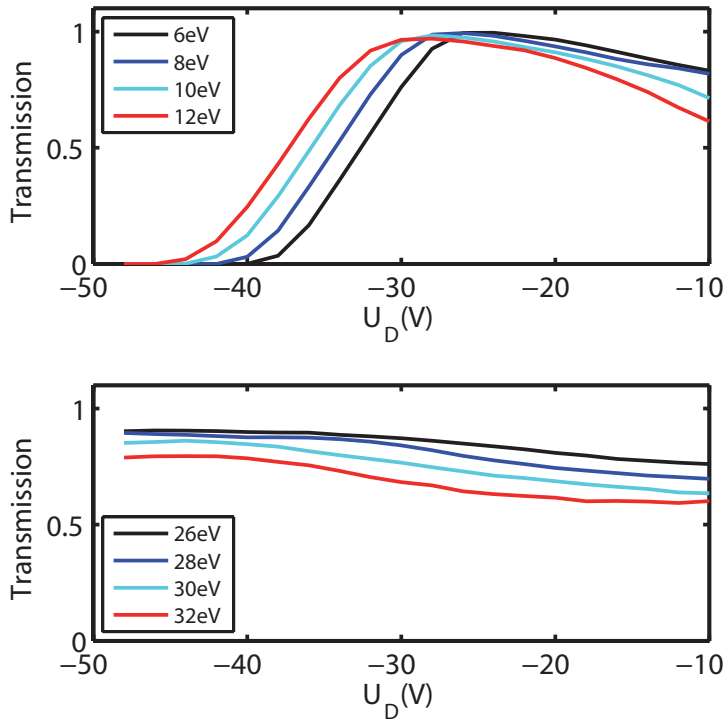


Figure 3.17: Simulated transmission of the electron spectrometer for different electron energies and retardation modes used for the FEL experiments.

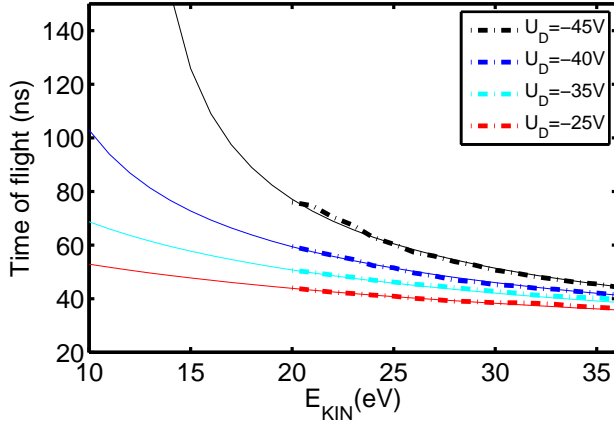


Figure 3.18: Energy to time-of-flight conversion for different retardation potentials used in the FLASH experiments. The dashed lines indicate the time-of-flight as obtained from Monte Carlo Simulations. The solid lines express the expected flight time according eq. 3.4.

by (c.f. eq. 2.40)

$$v_D \approx \sqrt{v_{\text{eff}}^2 + \frac{2q(U_S - U_D)}{m_e}}, \quad (3.4)$$

where U_S denotes the depth of the saddle point and U_D the potential which is applied to the stack of the drift electrodes. By this means, it is consequently possible to partly compensate for the additional energy the electrons gain, while they are generated in the saddle point. To ensure a tolerable transmission of the spectrometer, the well of the saddle point has to be larger than the barrier imposed by the drift unit $U_S \geq U_D$. Eq. 3.4 can be used to derive the energy to time-of-flight conversion of the spectrometer. Here an effective length has to be introduced to compensate for the oversimplifying assumption of an idealized parallelization process (c.f. sec. 2.3.2). As it is shown in fig. 3.18, the energy resolution of the spectrometer depends for a fixed saddle point on the retardation potential, i.e. the best resolution is given for $U_D = -45V$.

Stray light protection

According to the photoelectric effect, an electron can be ejected from a metal once the photon energy of the irradiating light is larger than the work function $\hbar\omega \geq \Phi$ of the material. Under normal operational conditions, the photon energy delivered by FLASH, exceeds by far the work function of the materials used for the different components of the spectrometer, i.e. each photon hitting the surface of the electrodes can therefore eject a high energetic electron. If such an electron reaches the acceptance volume of the spectrometer, it will be guided towards one of the electron detectors. In order to prevent stray light from entering the inner part of the

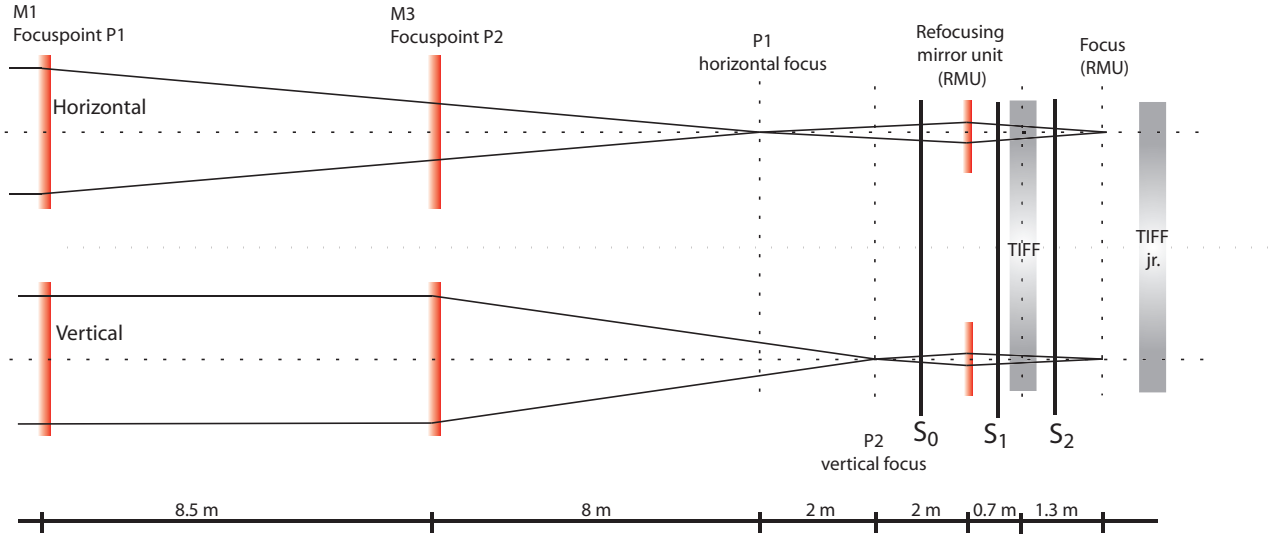


Figure 3.19: Schematic of plain grating monochromator beam-line two at FLASH. Focal length of different elements taken from [Mar06]. The position of the different stray-light protection units is indicated by S_{0-2} .

spectrometer, a novel stray light protection system has been developed. In fig. 3.19, the principle layout of the plain grating monochromator beam line two at FLASH is shown. The main elements of interest for designing a stray light protection system are the toroidal Mirrors M1 and M3 which define the horizontal and vertical focusing of the photon beam in front of the refocusing mirror unit (RMU). As the horizontal and vertical diameter of the laser beam differ in front of the RMU unit, a cross with four independently moveable protection plates was installed one meter in front of the RMU unit. This guard unit S_0 is used to collimate the beam to an appropriate diameter d_1 . The collimation of the beam with guard unit S_0 inevitably generates stray light emerging from the edges of the guards plates while they actively cut into the beam. The second guard system S_1 is thus installed as close as possible to the entrance of the TIFF vacuum chamber to prevent that stray light from entering the interaction region. Since TIFF and TIFF jr. are operated in parallel backscattered light from FLASH hitting a beam tube of TIFF jr. might also enter the spectrometer. Therefore, as a last protection unit a third system of four independently moveable guard plates S_2 is installed at the exit of the TIFF vacuum chamber.

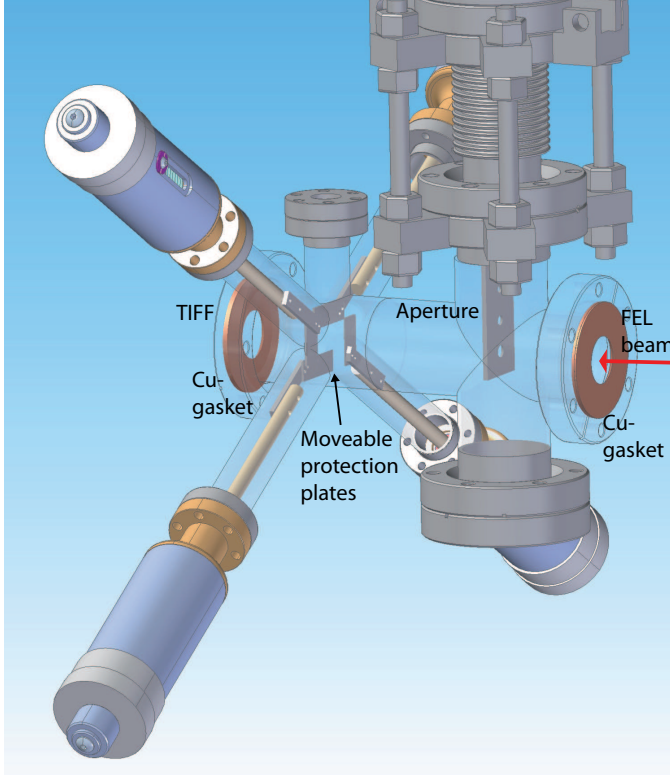


Figure 3.20: Technical drawing of stray light protection system S_1 . The key elements are two copper gaskets with a central hole of 10 mm radius and the set of four independently movable guard plates. To make the hole system fit into the gap between the RMU and the TIFF vacuum chamber, the feedthroughs are arranged under an angle of 30° .

3.2.2 Magnetic bottle electron spectrometer

The second electron spectrometer which was used for the photodetachment measurement of O^- (chapter 4), is the magnetic bottle spectrometer. In such a device the parallelization and the stabilization of the electron motion towards the detection unit is realized with a strong and a weak magnetic field. In the first section a strong permanent magnet bends the momentum of the electron towards the drift unit. Within the drift tube of about 600 mm length, a weak homogenous magnetic field guides the electrons towards the 40 mm multi-channel plate detector. Inside the drift unit a solenoid maintains a field with a typical strength of about (~ 2 mT). The aperture on the entrance is electrically insulated from the drift tube and can be biased, typically $U_A = 0.. + 20$ V. By this, the time-of-flight of the electrons is shifted, allowing to determine the kinetic energy of the observed photoelectrons. A detailed description of the technical aspects of the magnetic bottle spectrometer are given in [Muc12, Muc11, For12].

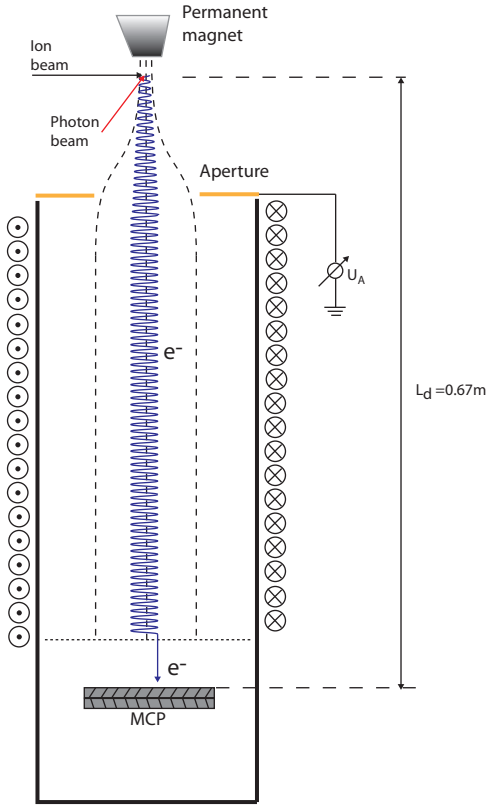


Figure 3.21: Schematic of magnetic bottle spectrometer with permanent magnet and solenoid around the drift tube. The aperture at the entrance of the drift tube can be electrically biased.

3.3 Position sensitive fragment detectors

3.3.1 Multi-Channel Plate

A multi-channel plate (MCP) consists of a thin glass plate with an array of parallel oriented capillaries inside. Front and back side of the glass plate are covered with a resist to lower the resistance which allows to apply a potential between the front and back of the glass plate. When a fragment impacts on the front side of the capillary, an electron is ejected from the surface. The external field further accelerates the electron inside the micro channels and after multiple hits a cascade of secondary electrons is generated. Depending on the mode of operation, about 2 kV are applied between MCP front and back. This yields about $10^3 - 10^4$ electrons which are stripped off from the MCP. On a timescale of about 50 ns the power supply cannot deliver the removed charged and thus the potential drop of MCP power supply can be used to detect an impact of a break-up product on the MCP. A normal MCP can hence be used to measure the time-of-flight of the either neutral or charged fragment [Jag02].

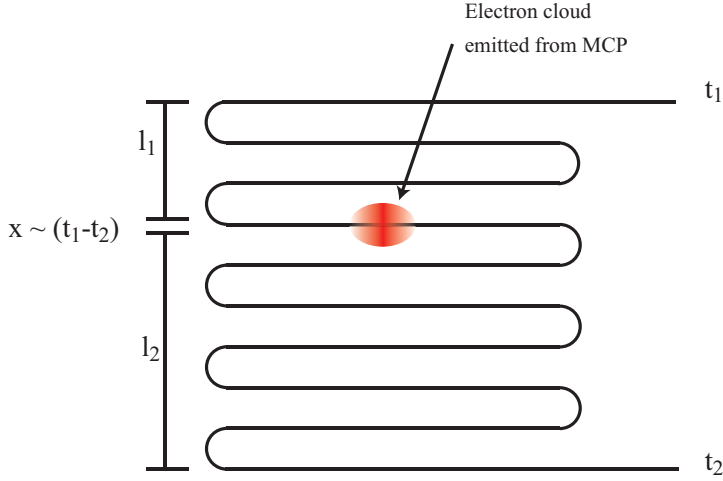


Figure 3.22: Illustration of delay line principle, with a meander shaped delay-line structure.

3.3.2 Delay line detection principle

For a kinematical complete investigation of the fragmentation process of the molecule, the momentum change in the center of mass frame of the break-up products has to be accessible. To reconstruct the 3D coordinate of the break-up, the position of the impinging particle relative to the parent ion-beam is of crucial interest. Several approaches allow for position sensitive fragment detection. One is to make use of the finite travel time an electrical signal needs to propagate through a conductor. When a charged particle hits a normal multi-channel plate, an electron cloud is generated. If that charge is dumped on a positively biased wire, a signal with finite travel time to both ends of the wire can be observed. Thus the propagation time of the signal to both ends of the conductor yields for one dimension information on the impact position. Among others, for a simple position reconstruction a meander shaped geometry of the electrical wiring can be used (see fig. 3.22). In order to obtain the impact position for a second dimension, another for instance perpendicularly crossed meander structure is necessary. When the clock is started, once the FEL light was present in the interaction region, the arrival time of the signal on each end of the two wire systems (u , v) is given by,

$$T_{u,1}(i) = t(i) + P_{u,1}(i), \quad (3.5)$$

$$T_{u,2}(i) = t(i) + P_{u,2}(i), \quad (3.6)$$

$$T_{v,1}(i) = t(i) + P_{v,1}(i), \quad (3.7)$$

$$T_{v,2}(i) = t(i) + P_{v,2}(i), \quad (3.8)$$

where $t(i)$ denotes the time-of-flight of the particle from the interaction point to the detector and $P([u, v], [1, 2])$ expresses the propagation time of the signal along the wires. The position can therefore be obtained by measuring the arrival times of the signal on the four ends of the two wire systems. A complete set of information for a fragment impact on a normal position sensitive multi-channel plate thus constitutes of five time information, one for each end of the wire and the MCP signal. A constant for each event i , which characterizes a complete set of information is given by the time sum

$$\sum (i)_k = T_{k,1}(i) + T_{k,2}(i) - 2T_d(i), \quad (3.9)$$

where $T_d(i)$ expresses the signal arrival time measured with the multi-channel plate. The time difference thus contains the information on the impact position along the axis $k = (u, v)$

$$\Delta_k(i) = T_{x,1}(i) - T_{x,2}(i). \quad (3.10)$$

With the following relation the,

$$\delta_k(i) = \alpha_k[\Delta_k(i) + \beta_k] \quad (3.11)$$

position of the impact is calculated. The typical propagation time of the electrical signal along the delay line is given by $\alpha_k \propto 0.5 \text{ mm/ns}$. The offset of time zero of the delay line, due to the geometrical crossing, is accounted for with β_k . For (DET 2) the orientation of the delay lines coincides with the laboratory x-y frame, hence $\delta_k(i)$ states already the x or y position of the event.

For the second detector, DET 2, the situation is somewhat more complex since three delay line systems $k = (u, v, w)$ are used. In addition the delay lines (u, v, w) are oriented under 0° , 60° and 120° with respect to the laboratory y-axis. Each system covers two rectangular regions of the active area around the central hole. Therefore eq. 3.11 has to be extended to

$$\delta_k(i) = \begin{cases} [\Delta_k(i) + \beta_k^+], & \Delta_k(i) \geq 0 \\ [\Delta_k(i) - \beta_k^-], & \Delta_k(i) \leq 0. \end{cases} \quad (3.12)$$

Under these conditions $\beta_k^{+/-}$ accounts for a likely asymmetric arrangement of the delay lines around the center. The transformation into the laboratory x-y frame is then obtained by applying the standard two dimensional rotation operator $\mathbf{R}_{S(j)}$ for a rotation of 60° and 120° , respectively. The position in the lab frame is thus given

through

$$\begin{pmatrix} x(i) \\ y(i) \end{pmatrix} = \mathbf{R}_k \delta_k(i) + \begin{pmatrix} x_{k,0} \\ y_{k,0} \end{pmatrix}. \quad (3.13)$$

Due to the geometrical overlap of the delay lines on DET 1 some parts of active area are covered by three delay line layers. For such a scenario the time sum has to be used as a criteria to identify the system which yields the most precise information on the impact position.

3.4 The Free-Electron Laser FLASH

A **Free Electron Laser** (FEL) is a light source where free, pre-accelerated electrons interact with their own synchrotron radiation, allowing to generate coherent light. In contrast to a classical laser where the wavelength is imposed by the properties of the resonator, an FEL covers within certain boundaries, a tunable wavelength range. The achievements in this field are manifest in the accessible wavelength range. The first FEL operated in 1975, reached $10.6 \mu m$ whereas a state of the art machine can nowadays reach 1.2 \AA [Eli76, Emm10, Ack07]. Common to all FELs are the three basic components, namely the pulsed electron source, a linear accelerator and the undulator unit [Sal00, Kon80]. In fig. 3.23, the basic operation principle of FLASH is shown. An electron gun delivers the free electrons which are transported to a linear accelerator. There, the kinetic energy of the electrons is increased to almost relativistic velocities. At 150 MeV and 450 MeV the bunch length is compressed to reach a current of 2.5 kA. The now following undulator comprises serially arranged magnetic dipoles with alternating polarity. The vertical magnetic field inside the undulator imposes a transversal acceleration on the electrons forcing them on a sinusoidal trajectory along the undulator. By this, each electron emits spontaneous radiation. Since the electrons are propagating at almost relativistic velocities ($\beta = v/c \approx 1$), the amplitude of the elongation is relative small. The emitted radiation is thus confined to a narrow forward cone with an opening angle of $1/\gamma$, which depends on the ratio of relativistic and rest mass [Kin77]. The emitted radiation can hence interact with the electrons travelling ahead. The wavelength of the emitted radiation is given by

$$\lambda = \frac{\lambda_U}{2\gamma^2} (1 + K^2/2), \quad (3.14)$$

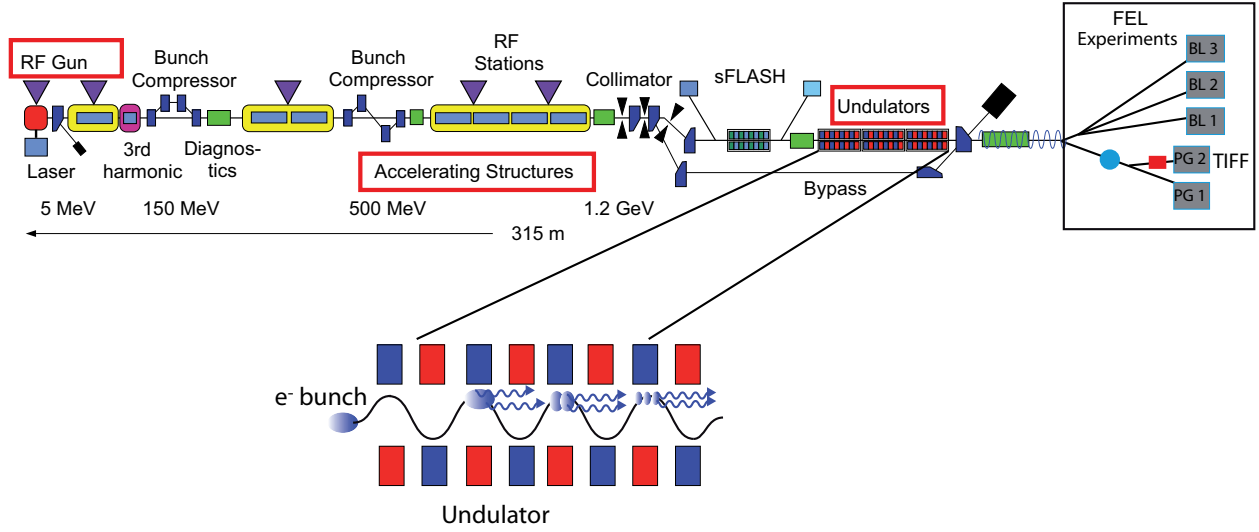


Figure 3.23: Layout of FLASH facility with fundamental units: Radio frequency electron gun, bunch compressor, accelerators, undulators and experimental hall. The pre-accelerated electron bunch is injected into the undulator unit, there the strong magnetic field forces the electrons on a sinusoidal trajectory. By this, the electrons interact with their own synchrotron radiation leading to a micro bunching. After the undulator all electrons emit coherently and five end station within the experimental hall can be provided with the laser light.

where λ_U represents the undulator period and $K = \frac{e B_0 \lambda_U}{2\pi m c}$ the undulator parameter, which depends on the magnetic field strength B_0 inside the undulator. The parameters of the undulator, like the periodicity and field strength, but also the energy of the electrons, can be used to tune the wavelength of the FEL radiation.

Self-stimulated spontaneous emission

The small relative velocity between the synchrotron radiation, emerging from the electrons' spontaneous emission and the bunch itself, leads to an interaction between the both. To outline the conditions for an optimal energy transfer between the electron beam and the radiation, some considerations are dedicated to the processes in the undulator unit. In the following, the electron beam is assumed to propagate along the y-direction. For an optimal energy transfer it can be shown that during a half cycle of the electrons motion, the radiation has to pass a distance which is longer than half the wavelength of the electron propagation [Sch08]. Thus the

runtime difference is

$$\Delta t = t_e - t_{rad.} = \left[\frac{1}{v_y} - \frac{1}{c} \right] \frac{\lambda_U}{2}. \quad (3.15)$$

With the condition for an optimal energy transfer $c \Delta t = \lambda_{rad.}/2$, the wavelength is given through

$$\lambda_{rad.} = \frac{\lambda_U}{2\gamma^2} (1 + K^2/2) \quad (3.16)$$

When the electron bunch is injected into the undulator unit, only a part of them fulfill the conditions for a positive energy transfer. The position of a single electron within the undulator can be stated by

$$y(t) = v_y t + \frac{\phi(t) + \pi/2}{k_{rad.} + k_U}. \quad (3.17)$$

The first part of the equation expresses the position of the bunch within the undulator unit, whereas the second one states the position of an electron within the bunch. The pandermotive phase therein is given by $\phi = (k_{rad.} + k_U)z - \omega_{rad.}t + \phi_0$. At time zero when the electron package enters the undulator $\phi = \phi_0$ and can be assumed as homogeneously distributed. The phase dependence of the electron energy,

$$\frac{dW_e}{dt} \propto -\cos(\phi), \quad (3.18)$$

leads to an exchange of energy between the field and electron bunch. As a consequence, the electrons which obey a phase $|\phi_0| > \pi/2$, donate energy to the field. In contrast, the ones with $\pi/2 < |\phi_0| < \pi$, gain energy from the field. Thus, the electron density is increasing in a vicinity of maximal energy exchange. The so called self-amplified spontaneous emission leads to a micro-bunching of the electron bunch inside the undulator unit. After the electrons have passed the undulator unit, they emit coherently with an intensity proportional to the square of the number of injected electrons, N_e^2 .

3.5 Data acquisition and analysis

In the above sections, the TIFF apparatus as well as the key elements of the photon beam-line have been introduced. In the upcoming paragraph a brief outline of the data acquisition system and the basic steps of the data analysis procedure are given.

3.5.1 Data acquisition

The high voltage power supplies for the elements of the ion beam line the mirror and the spectrometer are controlled via a LabView program. The Data-acquisition (DAQ) system is triggered by a TTL pulse delivered from the FLASH facility. Depending on the target of interest, these timers have to be shifted to match the arrival times of photon and ion beam within the interaction region.

In total four RoentDek 3D-imaging detectors are used at TIFF, where each of them is read out with a RoentDek module. The unit comprises built in differential amplifiers with an integrated constant fraction discriminator (CFD) circuit for each channel which transform the electrical signal of the delay lines and the multi-channel plates into logical pulses (NIM). The system allows for a pulse-pair resolution of 20 ns. Here, the threshold of the CFD of each channel has to be adapted to suppress ringing and to let the real hits pass through.

The exact arrival time of the FEL pulse in the interaction region is monitored with an electrically biased photon beam dump. That signal and the one from DET 3 have to be externally converted into a logical pulse sequence.

The various logical signals of the detectors are then fed into the two VME based time to digital converter (TDC) cards with 16 channels per card and a time resolution of 24 ps. In the current status of TIFF 28 channels of the TDC cards are occupied. The readout of the TDC unit is also organized via a LabView control panel. To acquire the analog signals as the intensity of the ion and photon beam a 12 channel analog to digital (ADC) converter is also implemented in the DAQ system. In addition, another 8 channel ADC unit is used to monitor the status of the different high voltage elements of the beam line.

A typical time structure of FLASH is depicted in fig. 3.24. The macro bunch train arrives with a repetition rate of 20 Hz. The micro bunches can be delivered with a repetition rate between 200 kHz and 1 MHz. The time structure of the FEL micro pulse train as, it is requested for the experiment, is determined by the time of flight of the particles to the different fragment detectors, typically $1 - 10 \mu\text{s}$. When the trap is operated in direct transfer mode, the four measurement cycles of the experiment are organized as follows:

Signal cycle: One FEL pulse train with 50 micro bunches is temporally overlapped with 50 ion bunches of $\sim 1 \mu\text{s}$ width in the interaction region. To ensure that the power supplies have reached stable conditions, typically 60 ion bunches are generated, from which the tenth to the last bunch are irradiated. The electrical signal, extracted

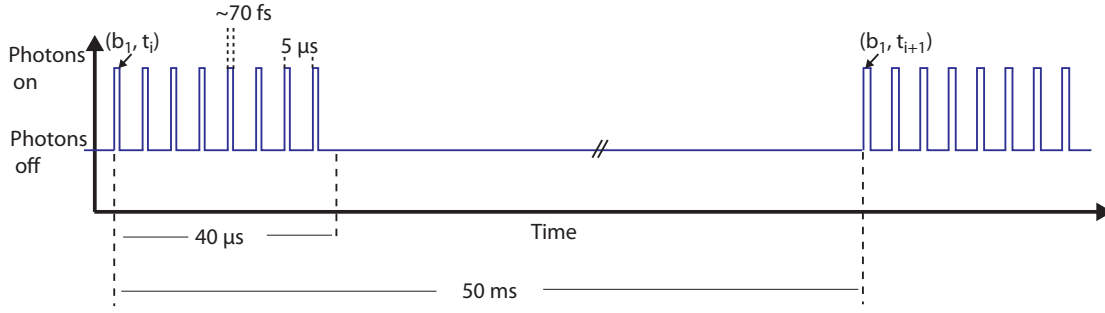


Figure 3.24: Time-structure of typical FEL bunch train. Macro cycle with 20 Hz repetition rate constitutes of 50 micro bunches. Blue line illustrates micro bunch train with 200 kHz repetition rate.

from the photon beam dump marks the zero time of each micro bunch to which the signals of the different detectors are referenced.

Ion only cycle: In between the next FEL pulse train a cycle where only fifty ion bunches are present is interlaced to measure the ion induced background on the fragment detectors. For these signals the average arrival time of the FEL micro bunches is used as a time zero marker.

Dark measurement: During one cycle neither ion nor photon beam are present in the interaction region. This sequence is acquired to detect switching noise on the fragment detectors.

Photon only cycle: In the now following photon only cycle the fifty photon bunches are passing without ions through the interaction region. Such a trace is acquired to measure the photon induced background.

Typically 500 cycles (trains) with 50 FEL pulses are written in an ASCII format to the output files. For each cycle the TDC and ADC values of all elements are acquired.

3.5.2 Data analysis

The data analysis procedure can be subdivided into two fundamental steps. At first every TDC value is referenced to the copper dump time of the respective FLASH pulse. For cycles where no photons were present in the interaction region, an average copper dump time is used as a time reference. By this, each TDC value can be assigned to a certain FEL bunch and train (b_i, t_i) which defines the identity of the hit where the ADC values are used as a marker to separate signal and background

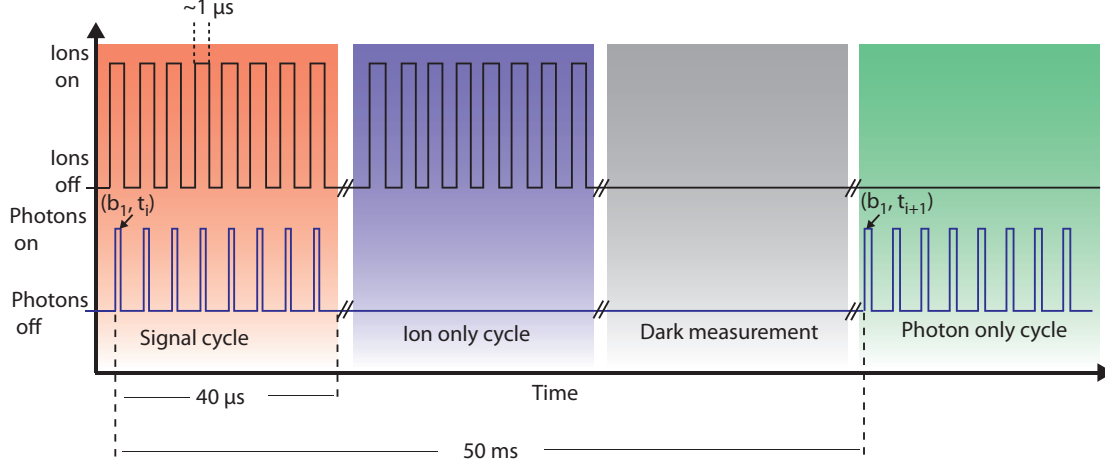


Figure 3.25: Illustration of timing scheme of the four measurement cycles.

traces from each other.

In the second more complex step, the corresponding hits on the delay lines and the multi-channel plates of the imaging detectors have to be assigned. For that purpose all hits which appeared within a certain FEL bunch and train are isolated and the time sum according eq. 3.9 for each permutation is computed. The combination of hits which yields the optimal time sum is then considered to stem from a real event. Once the real events are assigned, the impact position of the fragments is computed according the algorithm outlined in sec. 3.3.

Coincidence analysis

After the fundamental steps of the data-analysis procedure have been performed, every hit on the imaging detectors is categorized via $(T_i, x_i, y_i, b_i, t_i, m_{(b_i, t_i)})$, where T_i denotes the time-of-flight, (x_i, y_i) the impact position and $m_{(b_i, t_i)}$ the multiplicity of the respective bunch and train. For the normal multi-channel plate detectors the events are organized according $(T_i, b_i, t_i, m_{(b_i, t_i)})$. It is therefore possible to use either of the entries of the event list, the time-of-flight, the impact position or the multiplicity as a criteria to require hits on different detectors to appear with such coincidence restriction.

In the following, the coincidence analysis procedure using the time-of-flight as a criteria is illustrated. Here, a time window (region of interest ROI) is set around a certain time-of-flight region ($T_{\min} \leq T_i \leq T_{\max}$) of one detector, for instance DET 1. The events, which are enclosed in the time window, are either signal or background

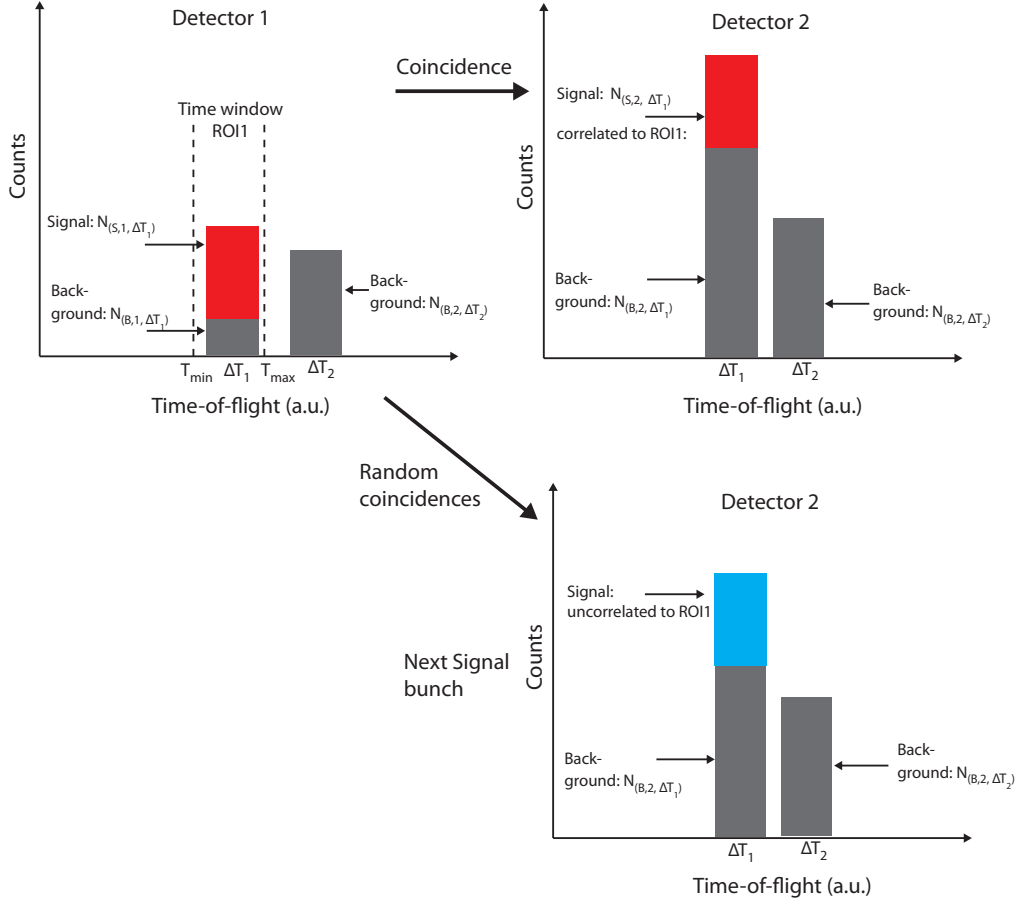


Figure 3.26: Assumed signal and background distribution of DET 1 and DET 2.

induced $N_{(T_{min} \leq T_i \leq T_{max}, D1)} = N_{(S,1, \Delta T_1)} + N_{(B,1, \Delta T_1)}$. For simplicity, the background is treated as such and is not distinguished to be photon or ion induced. The bunch and train number of each hit within the ROI is determined and the events on the other detector (like DET 2), which occurred within the same bunch and train are extracted.

The obtained coincident signal comprises, besides the real coincident hits all, various combinations of false coincidences, i.e. a real signal hit on DET 1 is for instance accompanied by a background hit on DET 2.

To estimate the false coincidences, the hits of DET 1 enclosed within the ROI are correlated with the hits on the second detector which are obtained for the next following signal bunch train $(b_i, t_i + 1)$. With such a correlation no real coincident signal hits on the second detector are prevailing. Under the assumption that the background remains constant the false coincident events can be estimated.

Chapter 4

Electron emission from fast O^- ions

In sec. 3.2 the magnetic bottle and the newly developed saddle-point electron spectrometer have been introduced. For both devices the idea is to do photoelectron spectroscopy on fast moving molecular ion beams under xuv radiation. In a first test both spectrometers have been employed to investigate the photodetachment process on a fast moving beam of O^- anions at a wavelength of 532 nm and 266 nm, respectively. Here the interest was on how the kinematical broadening, imposed on the energies of the emitted electrons by the movement of the ion beam (see sec. 2.3), can be applied to map information on the anisotropy of the electron emission into the observable time-of-flight (TOF) distribution of the photoelectrons. In case of the measurements performed with the saddle-point spectrometer a SIMION based Monte-Carlo Simulation (c.f. sec. A) was developed and applied to represent the observed photoelectron spectra.

Moreover, the photodetachment of the oxygen anion O^- , with the electron configuration $2s^2 2p^5$, is an important process for understanding the effects of correlated electron motion in an open shell system. Through photoabsorption, an electron-oxygen state in the scattering continuum is generated, which is characterized by various final states, composed of a free electron and a neutral oxygen atom,

$$O^-(^2P) + \hbar\omega \rightarrow O(^{2S+1}L) + e^- + E_{(k,e^-)}. \quad (4.1)$$

Within the LS-Coupling, the scattering continuum has components of 2P , 2D or 2S symmetry ($\Delta L = 0, \pm 1$) (c.f. fig. 4.1). Since the electron has been detached from a p-orbital the continuum electron can either have s or d wave character. The integral effects of the photoabsorption and the scattering reaction are observationally

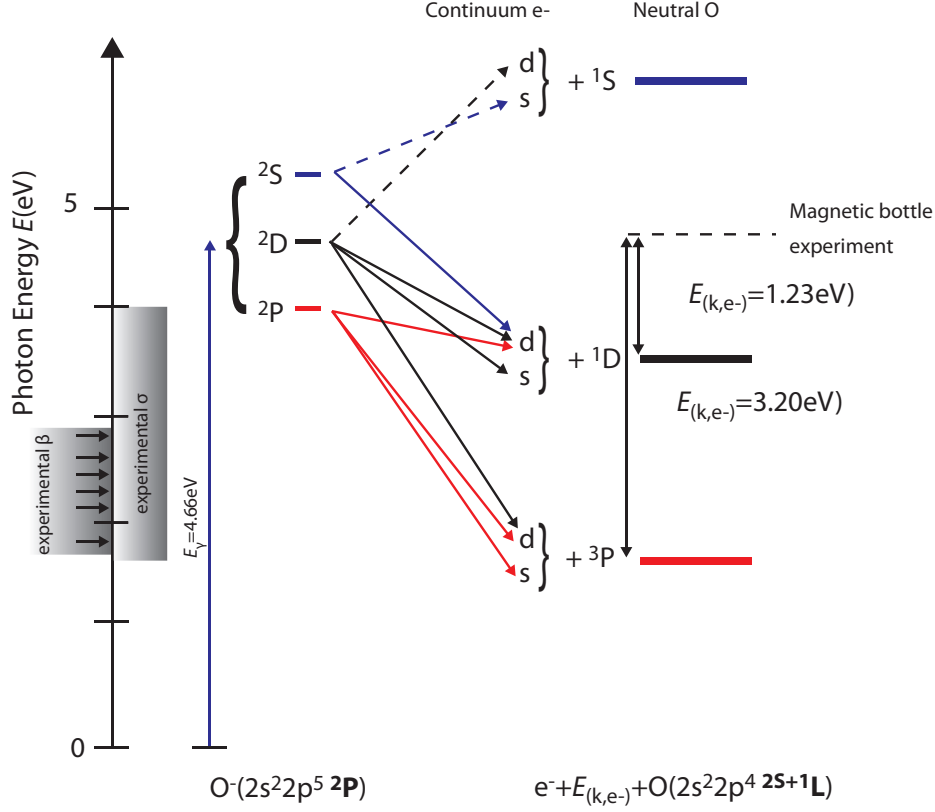


Figure 4.1: Illustration of the photodetachment of atomic oxygen at 266 nm. The shaded area along the energy axis indicates the region of experimentally known cross sections [Bra65, Neu85, Suz87]. The horizontal arrows mark photon energies where angular distributions and branching ratios into the 3P_J multiplet states have been observed [Hal68, Bre78, Han89, Cav07]. The blue, red and black arrows indicate the allowed coupling of the scattering continuum of $^2S, ^2D, ^2P$ symmetry into the different final states.

manifest both through the angular distribution of photoelectrons, described by the anisotropy parameter, and through the relative populations F_X ($X=^3P_J, ^1D_J, ^1S_J$) of final excited states of the neutral O-atom, as identified by the photoelectron energy [Dom10].

4.1 Magnetic bottle spectrometer

At first, the results which are obtained with magnetic bottle spectrometer are reviewed. A detailed account for all aspects is given in cite [Dom10]. The photon

energy of $E_\gamma = 4.66$ eV is sufficient to populate the first excited state of the residual neutral oxygen atom $O(^1D)$, indicated by black dashed lines in fig. 4.1. The major focus of the experiment was on how the parametric Monte-Carlo model intruded in sec. A.2 can be applied to represent the photoelectron spectrum and to explore the unknown asymmetry parameter and branching of the transitions into the different final states of the residual neutral oxygen atom $O(^1D)$ and $O(^3P)$, respectively.

4.1.1 Experimental parameters

A schematic drawing of the recently built TIFF jr. ion beam line and interaction zone equipped, with the magnetic bottle photoelectron spectrometer (c.f. sec. 4.2) is shown in fig. 4.2. Both, the ion and the photon beam, move in the horizontal plane. An ion beam of oxygen anions (~ 2 nA) with a kinetic energy of $E_0 = 4.45$ keV was extracted from a hollow cathode ion source operated in negative mode (see sec. 3.1.1). From TIFF, ion pulses with a width of $10 \mu\text{s}$ were transported through TIFF jr. to the interaction point. There, the ion pulses were crossed at 90 degrees by a horizontally polarized laser with 266 nm wavelength. A mean pulse width of ~ 5 ns and a pulse energy of $\sim 50 \mu\text{J}$ correspond to $\sim 7 \times 10^{13}$ photons per pulse. The laser was operated with a repetition rate of 40 Hz. The spatial profiles of the two beams were determined inside the electron spectrometer with a movable beam flag [For10]. The ion beam could be represented by Gaussian distributions in both, horizontal and vertical directions with widths (RMS) of 1.5 mm and 1.4 mm, respectively. The photon beam was nearly circular with a Gaussian width of 0.9 mm, thus, a total of ~ 40 ions were irradiated in each laser pulse. Each signal cycle (photon and ion beam on) was interlaced with a cycle where only the photon or only the ion beam was present in the interaction region. For each laser pulse the relative intensity and the precise arrival time at the interaction point were monitored by a fast photodiode while the absolute mean pulse intensity was recorded using a slower thermal power meter.

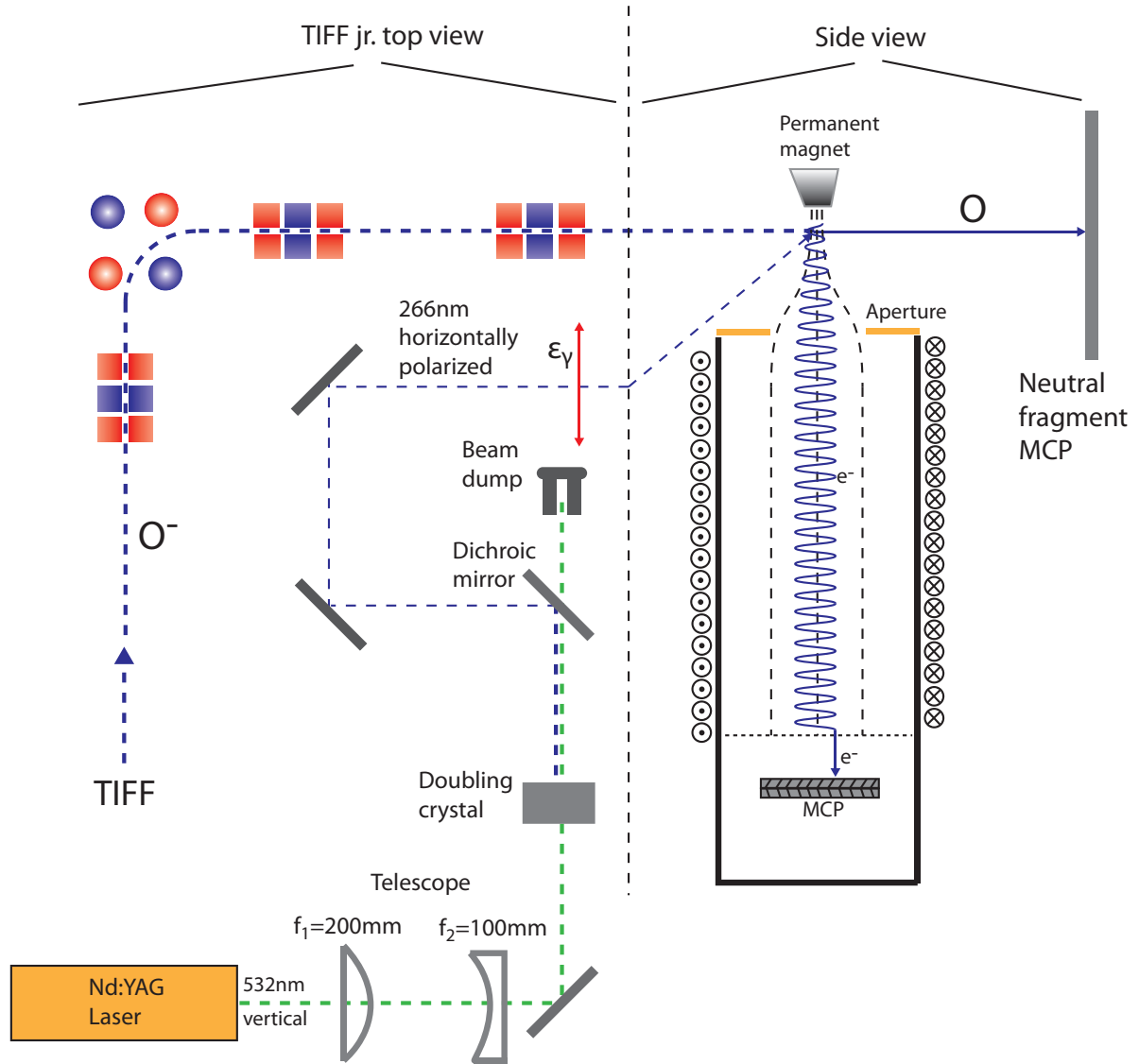


Figure 4.2: Schematic drawing of TIFF jr. ion beam line with quadrupole triplet unit to focus and to steer the beam into the interaction region equipped with magnetic bottle spectrometer [For10] and the arrangement of the optical elements to double the frequency of the 2nd harmonic of a Nd:YAG laser. The neutral fragments are detected with a non-position sensitive multi-channel plate.

4.1.2 Experimental results

Photoelectron time-of-flight distribution

Fig.4.3 displays the observed electron time-of-flight distribution for the photodetachment of O^- at 266 nm after background correction. The distribution exhibits a

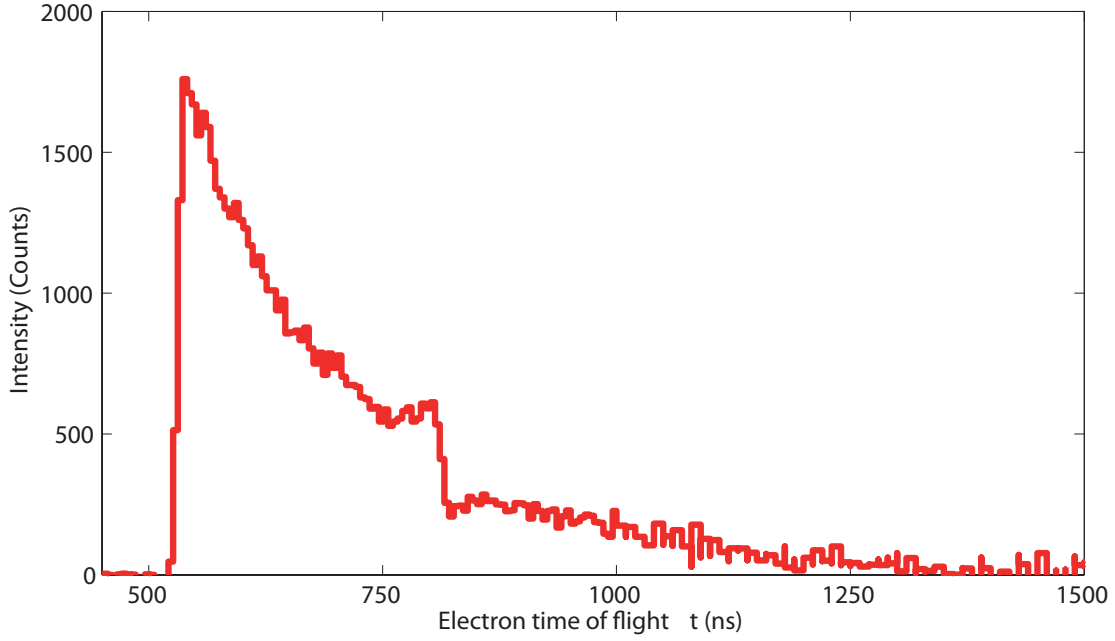


Figure 4.3: Measured electron time-of-flight distribution for photodetachment of O^- at 266 nm obtained with the magnetic bottle electron spectrometer.

rather sharp on and offset around 550 ns and 820 ns. In comparison to the computed distributions in sec. 2.3.2 the shape of the feature, enclosed between 550 – 820 ns, indicates these electrons to stem from a ($\beta = 0$) transition. The smooth characteristics of the second feature, ranging from 750 ns down to 1500 ns, mimics a ($\beta = -1$) transition. In the vicinity around 800 ns both electron families seem to contribute to the integrated distribution. The signal on the neutral fragment detector is not displayed since there only the time-of-flight of the neutral O-fragment appeared.

4.1.3 Monte Carlo model

The previous discussion illustrated the occurrence of two distinct components of the electron time-of-flight distribution. In the rest frame of the reactants a photoelectron appears with a kinetic energy [Dom10]

$$E_{(\text{cm}, e^-)} = (E_\gamma - E_{D,O} - E_{X,O}), \quad (4.2)$$

with $E_\gamma = 4.67$ eV and $E_{D,O} = 1.46$ eV the detachment threshold energy of oxygen. The excitation energy of the residual neutral oxygen is $E_{X,O(^3P)} = 0$ and $E_{X,O(^1D)} = 1.97$ eV, respectively. This yields $E_{k,e} = 3.20$ eV and $E_{k,e} = 1.23$ eV. Under the assumption of

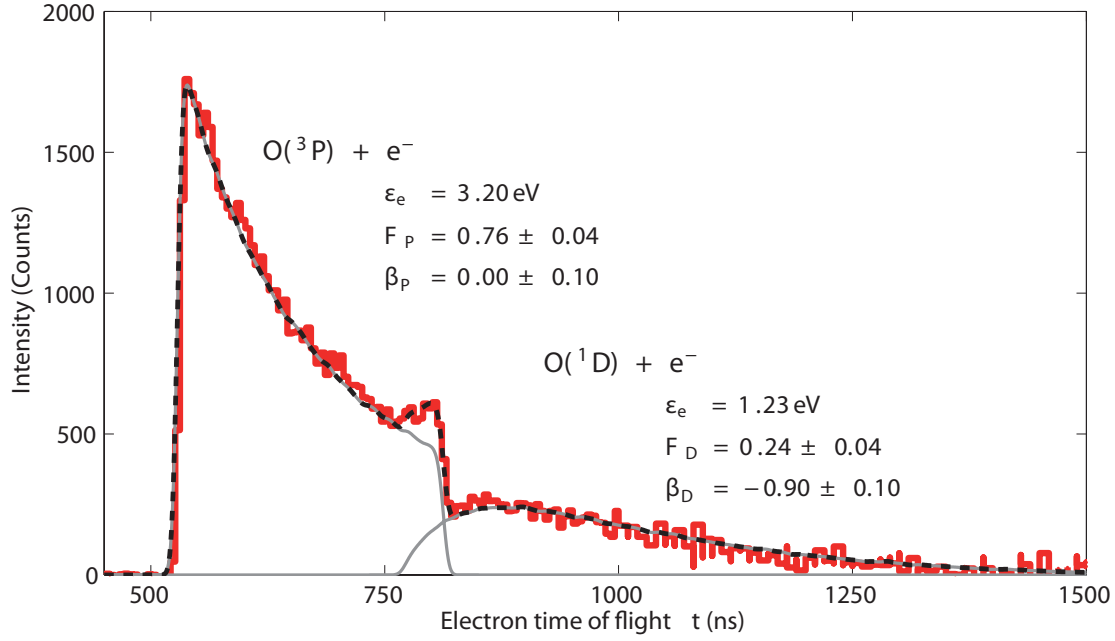


Figure 4.4: Measured electron time-of-flight distribution after photodetachment of O^- at 266 nm. The dashed black curve shows a fit to the distribution with a Monte Carlo model. The gray (thin) curves show the individual contributions from transitions to $O(^3P)$ and $O(^1D)$ to the total fit.

an idealized parallelization process in the inhomogeneous field, eq.(2.38) can be applied. By this, the overall distribution can be qualitatively represented and the components can be assigned to transitions into the 3P ($E_{k,e} = 3.20$ eV, $t = 550$ - 820 ns) and the 1D ($E_{k,e} = 1.23$ eV, $t = 750$ - 1500 ns) state of atomic oxygen.

Thus, for a quantitative modeling of the observed TOF distribution with the parametric Monte Carlo model (c.f. sec. A.2), two independent components have to be implemented and each of them is weighted by the respective amplitude (F_P , F_D)

$$P_{\text{exp}}(t) = F_P P_{\text{MC}}(t, 3.20 \text{ eV}, \beta_P, \mathbf{p}) + F_D P_{\text{MC}}(t, 1.23 \text{ eV}, \beta_D, \mathbf{p}). \quad (4.3)$$

The set of parameters which goes into the simulation can be separated in the ones which characterize the physics of the detachment process like the unknown channel fractions (F_P , F_D) and the unknown anisotropy parameters (β_P , β_D). The temporal width of the laser pulse δt , the drift Length L_d and (A_0, A_1) which account for the adiabatic parallelization go into the model as setup depended parameters $\mathbf{p} = (A_0, A_1, L_d, \delta t)$. The evaluation of the parametric Monte Carlo model is described in

sec. A.

In fig. 4.4, the dashed black line represents the resulting model distribution. The measured electron spectrum can thus be nicely represented by the parametric Monte-Carlo model and turns out for the transition to the O(³P) state

$$\begin{aligned} F_P &= 0.76 \pm 0.04, \\ \beta_P &= 0.00 \pm 0.10, \end{aligned} \tag{4.4}$$

and for the transition to the O(¹D) state

$$\begin{aligned} F_D &= 0.24 \pm 0.04, \\ \beta_D &= -0.90 \pm 0.10. \end{aligned} \tag{4.5}$$

4.1.4 Discussion

From the present experiment the branching ratio between excited and ground state oxygen production at 266 nm can be determined to be $F_D/F_P = 0.32 \pm 0.06$. A rough estimate has previously been given based on the total photodetachment cross section [Bra65]. On the theoretical side, several calculations around 266 nm have reported the total [Rob67, Zat06] and partial channel resolved cross sections allowing for a direct comparison to the present experiment. The ratio ¹D : ³P after detachment has so far been calculated to: ~ 0.8 [Coo62], ~ 0.6 [Gar67], ~ 0.5 [Cha72], and most recently ~ 0.25 [Wu03]. In comparison, the most recent calculation [Wu03] slightly underestimates the experimental result, while the earlier calculations all significantly overestimated the ¹D : ³P ratio.

The present experimental investigation is also the first to address the electron emission anisotropy in the region where both ¹D and ³P states of oxygen are accessible, while several experiments have been performed at lower energies [Hal68, Bre78, Han89, Cav07] (see also fig. 4.1). For the transition to ³P, the angular distribution mimics a pure s-wave with β close to zero as given in eq. (4.4), while the transition to the ¹D state is accompanied by a negative value of $\beta \sim -0.9$ far away from either pure s-wave ($\beta = 0$) or pure d-wave ($\beta = 1$) behavior, thus giving clear evidence for superposition of the outgoing waves. Only few calculations [Coo68, Ste79] for photon energies below 4 eV have given explicit values for the β parameter. Thus, a direct comparison to theory is not possible at this stage. For the transition to the ³P state, a simple linear extrapolation to higher energies seems to favor the Cooper-Zare

formula [Coo68] over the theory of Stehman and Woo [Ste79] giving a value for β_P close to the experimental value (0.00 ± 0.10).

Summarizing, these findings illustrate that the parametric Monte-Carlo model appears as a precise method to represent the photoelectron spectra, observed with a magnetic bottle spectrometer for the photodetachment on a fast moving O^- beam at $E_\gamma = 4.66$ eV. In the next paragraph, the results of the photodetachment measurement on O^- employing the saddle point electron spectrometer are presented.

4.2 Saddle point spectrometer

The main motivation for the investigation of the detachment process of a fast moving O^- beam using the newly build saddle-point spectrometer was to develop a SIMION based Monte-Carlo simulation to represent the observed electron spectra. The photon energy of $E_\gamma = 2.33$ eV, as employed during the experiment, is not sufficient to populate the first excited state of the residual neutral oxygen atom. Moreover, in these energy regime the detachment process has already been investigated in great detail [Cav07] which allows to employ these findings as calibration factors for the simulation.

4.2.1 Experimental parameter

The experiment was done at the X-Ring fast ion beam infrastructure which was recently built around the old ion injection beam line of the ASTRID storage ring in Aarhus, Denmark. A detailed description of the setup is given in [Ped12]. The oxygen anions were produced with a sputter ion source at a kinetic energy of 3 keV and a final dc current of 2 nA in the interaction region. Similarly to the setup described above, the photon and ion beams were perpendicularly crossed, but in contrary the 2nd harmonic of a Nd:YAG laser was used. The laser was vertically polarized, i.e. along the spectrometer axis ($\epsilon_\gamma = \mathbf{e}_z$).

Two different spectrometer configurations have been employed: A flat saddle point (a) $C_{1,2} = -72$ V with $U_0, D_0 = +56$ V which yields $U_S = -13$ V with a retardation potential of $U_D = -12.8$ V; and a steep saddle point (b) $C_{1/2} = -144$ V with $U_0, D_0 = +112$ V which yields $U_S = -26$ V with a retardation potential of $U_D = -25.6$ V (c.f. fig. 4.5).

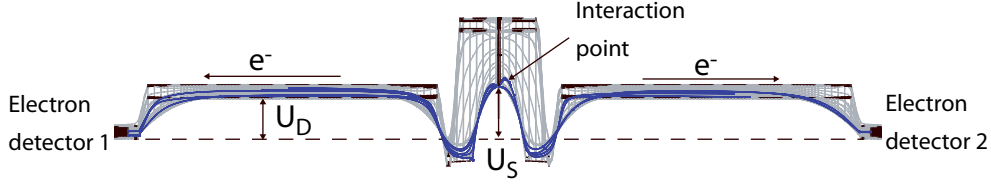


Figure 4.5: Potential landscape for an electron inside spectrometer (side view) when operated in saddle-point mode and a retardation potential U_D is applied to drift-unit.

4.2.2 Experimental results

Time-of-flight distribution

The observed time-of-flight distributions of the signal electrons, obtained for the two different operation modes of the spectrometer, are shown in fig. 4.6. Under the conditions of the flat saddle point, (c.f. fig. 4.6 (a)) the signal covers a time-of-flight range from $\sim 130 - 250$ ns whereas the signal obtained for the steep saddle point (c.f. fig. 4.6 (b)) appears in a more compressed fashion within a time window $\sim 120 - 180$ ns. In comparison to the computed spectra, shown in fig. 2.11, the overall shape of the observed distribution mimics a ($\beta = -1$) transition. In the spectrum as it was obtained with the magnetic bottle spectrometer shown in fig. 4.3 the corresponding signal ($O(^3P) + e^-$) occurred within 520-820 ns.

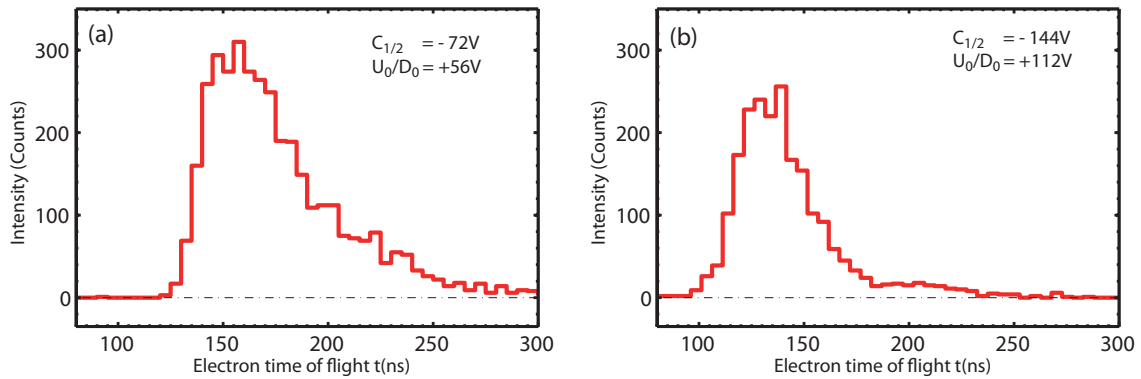


Figure 4.6: Electron time-of-flight spectra on upper electron detector for photodetachment of O^- at 532 nm obtained with the saddle point electron spectrometer.

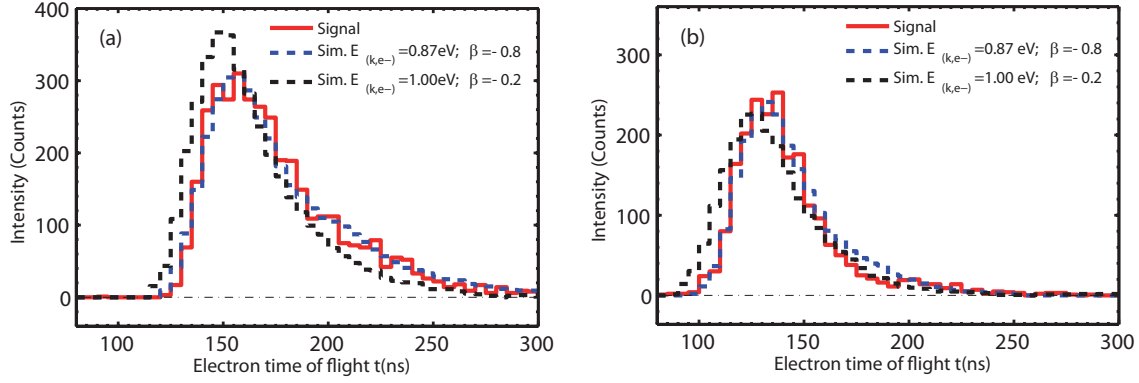


Figure 4.7: Measured electron time-of-flight spectra on upper electron detector (red curve) for configuration(1) fig. (a) and configuration (2) fig. (b). The dashed blue and black lines indicate the simulated spectra for $(E_{(k,e^-)}, \beta) = (0.87 \text{ eV}, -0.8)$ and $(E_{(k,e^-)}, \beta) = (1.00 \text{ eV}, -0.2)$, respectively.

4.2.3 Monte Carlo Simulation

The parallelization process of the photoelectrons inside the spectrometer cannot be represented by the parametric Monte Carlo model. Hence, to assign an asymmetry parameter to the observed distribution, the detachment process has to be modeled by a Monte Carlo simulation where the electron trajectory inside the spectrometer is computed with SIMION (c.f. sec. A).

Also here, two sets of parameters which go into the simulation have to be distinguished (compare table A.1). At first the setup depended parameters are illustrated. The potentials, applied to the different elements of the spectrometer are known within a precision of $\Delta U = \pm 0.2 \text{ V}$. The drift length from the interaction point to detector surface is $L_d = 150 \pm 1 \text{ mm}$. Since the measurements were performed with about equal event rates on the upper as well as lower electron detector, it can be assumed that the interaction point coincides with the saddle point. The kinetic energy of the ion beam can be determined to be $3 \pm 0.1 \text{ keV}$ and the one of a photoelectron emerging from a detachment process, leaving the neutral oxygen in its ground state is derived according eq. (4.2) to be $E_{(k,e)} = 0.87 \text{ eV}$. In [Cav07, Bre78] an asymmetry parameter of $\beta_P = 0.85 \pm 0.05$ for this photon energy has been reported, which was used in the simulation.

The dashed blue line in fig. 4.7 displays the simulated electron time-of-flight distribution as it is obtained for $(E_{(k,e^-)}, \beta) = (0.87 \text{ eV}, -0.8)$ and the two different operation modes of the spectrometer. To demonstrate the accuracy of the simulation, the input parameters of the simulation are varied to $(E_{(k,e^-)}, \beta) = (1.00 \text{ eV}, -0.2)$, yielding

the distributions as indicated by the black dashed lines. Here, it appears already obvious that for the flat saddle point (c.f. fig. 4.7(a)) the difference in the shape of both distributions is more pronounced as for the steep saddle-point configuration (c.f. fig. 4.7(b)). Especially for larger electron energies this will limit the ability to assign an appropriate asymmetry parameter to the observed electronic signal (see sec. 5.4).

The physically relevant input parameters of the simulation $E_{(k,e^-)}$ and β_P are well known quantities for the photodetachment of O^- at 532 nm. Since the computed distribution nicely reflect, within the boundaries of the setup dependent parameters, the measured electron time-of-flight spectra, the calibration i.e., the geometries of the different electrodes of the spectrometer are therefore correctly embedded in the simulation. Thus, this method can be extended to assign an energy as well as an asymmetry parameter to the electronic signal as it will be for instance observed for photoionization processes of molecular systems with photons in the vuv to soft x-ray spectral region (compare chapter 5 and 6).

4.3 Conclusion

The presented experiments represent a first example where the Doppler shift of electrons emitted from a fast moving ion beam has been used in combination with the magnetic bottle or saddle-point spectrometer to study angular distributions of photoelectrons [Dom10]. The possibility of angular resolved measurements using a magnetic bottle spectrometer was already discussed by Kruit *et al.* [Kru83] using retarding potentials, however, the Doppler effect has been mostly considered to be an artifact limiting the achievable energy resolution [Che87]. The method presented here appears as an alternative to approaches based on the rotation of the laser polarization, with a detector at a certain angle, but also to photoelectron imaging techniques [Peg89, Han99, Ped99]. Additionally, as indicated in fig. 4.2 and fig. 3.1, the spectrometers can be combined with fragment analyzing systems to detect the emerging break-up products from photon induced dissociation reactions in coincidence with the outgoing photoelectrons.

Chapter 5

Free electron laser experiments on H_3O^+

With the hydronium ion H_3O^+ as a first molecular target the dissociative photoionization at 56.7 eV photon energy was investigated with the upgraded detection system. In 2009, the hydronium ion has already been subject to fragmentation studies at $E_\gamma = 92$ eV [Ped09]. There it was found that outer valence ionized H_3O^{++} predominantly fragments into a binary $\text{H}_3\text{O}^{++} \rightarrow \text{H}_2\text{O}^+ + \text{H}^+$ and a three-body break-up pathway $\text{H}_3\text{O}^{++} \rightarrow \text{OH}^+ + 2\text{H}^+$. The detection system in use (c.f. sec. 3.1.2), gave only access to the light charged and neutral break-up products. The aim of the current experiment is to employ the newly built saddle-point spectrometer in combination with the heavy charged fragment analyzer to detect the incident photoelectron in coincidence with all outgoing reaction products emerging from the respective dissociation process.

5.1 Properties of H_3O^+

In the electronic ground state, the nuclei of the hydronium ion form a pyramidal structure of C_{3v} symmetry. The bond length is found to be $r_{\text{OH}} = 0.9758$ Å with an angle of $\alpha_{\text{HOH}} = 111.3^\circ$ between the different O-H bonds [Sea85]. The vibration of the H_3O^+ exhibits four fundamental modes: a symmetric stretch (breathing) mode ν_1 , a symmetric bend (umbrella) mode ν_2 and two asymmetric stretch modes ν_3, ν_4 with each of them twofold degenerated. The electronic configuration in the ground state of the ion is

$$(1a_1)^2(2a_1)^2(1e)^4(3a_1)^2 X^1A_1. \quad (5.1)$$

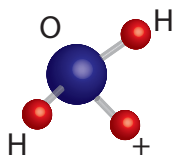
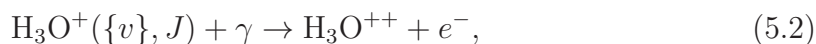


Figure 5.1: Theoretical minimum-energy structure of the hydronium ion H_3O^+ [Hea05].

The outer valence electrons are shared among the four fold populated $1e_1$ orbital, located along the O-H bonds and the doubly populated lone pair orbital $3a_1$ on the oxygen atom. The binding energies of the outer valence electrons were calculated to be 26.0 eV for the $3a_1$ and 31.2 eV for the $1e_1$ orbital [Raf77]. The inner valence orbitals $1a_1$ and $2a_1$ basically correspond to the 1s and 2s orbitals of the oxygen atom, with a binding energy of 49.3 eV for the $2a_1$ orbital.

5.2 Photoionization pathways

If the photon energy of the irradiating light exceeds the ionization threshold of the valence orbitals, further ionization of the monocation becomes possible (c.f. sec. 2.1.2). So far, only little is known about the potential energy surfaces arising from valence vacancies of H_3O^{++} . During the ionization process the nuclear configuration can be considered as being frozen, which leads to a vertical transition within the potential energy surface. The ionization process takes the form



where $(\{v\}, J)$ denote the vibrational and rotational quantum number of the monocation. According to Koopmans' theorem [Koo34], the orbital binding energies in H_3O^+ lead to an equivalent excitation of the dication. An energy level scheme for H_3O^+ and the valence ionized system H_3O^{++} is shown in the dark gray shaded column of fig. 5.2. As discussed in sec. 2.1.2, the potential energy surfaces corresponding to the excited H_3O^{++} levels are dissociative and can lead into a number of final break-up channels. Depending on the internal excitation of the reactant and the molecular products formed in the different fragmentation channels a certain amount of kinetic energy is released. Fig. 5.2 depicts the different fragmentation channels, which may open up for outer and inner valence ionization.

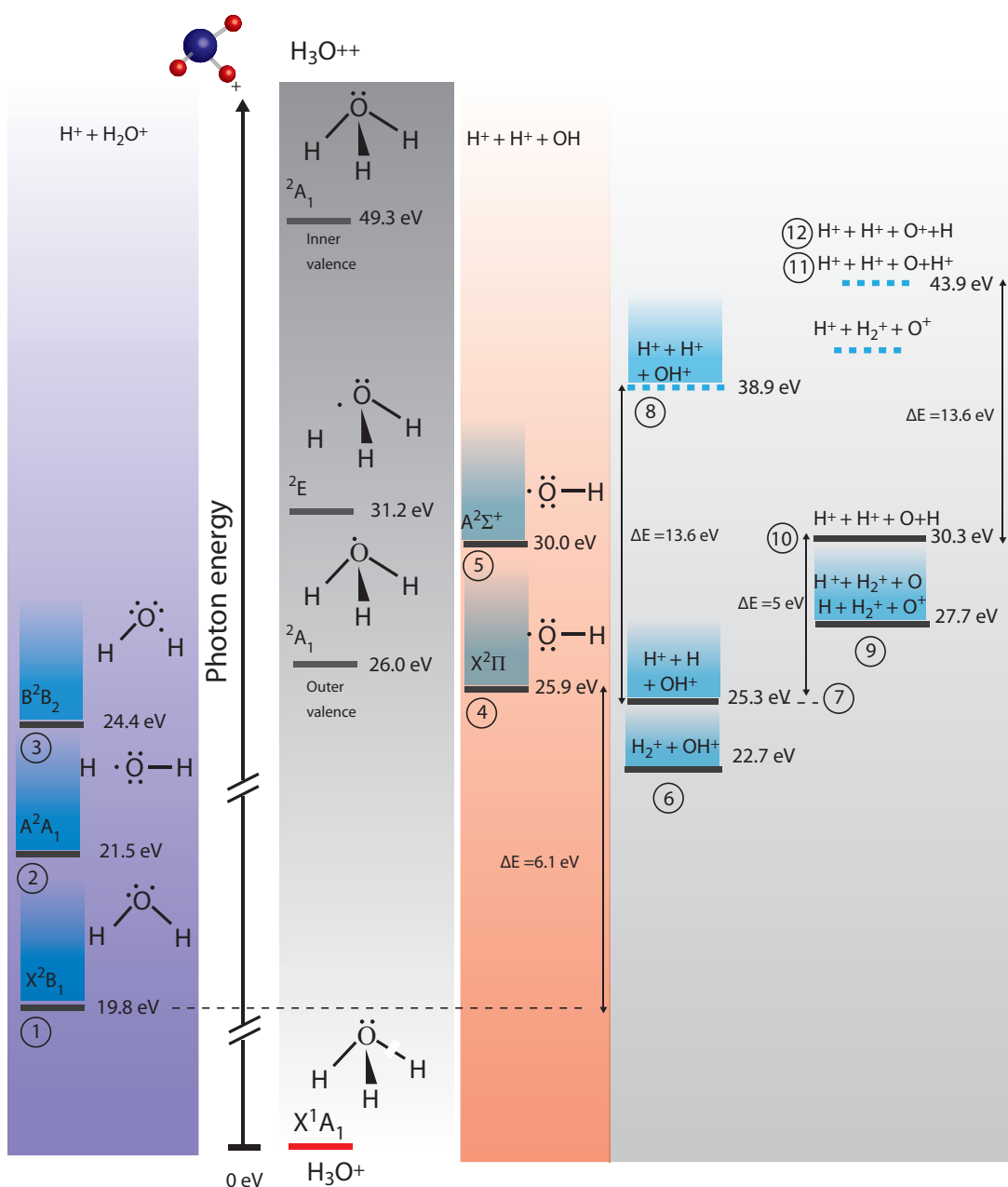


Figure 5.2: Inner and outer valence ionization energies of H_3O^+ , adapted from [Raf77], and level diagram for fragmentation into different break-up channels. Proton affinities and ionization energies are taken from [Nist, Hun98, Bal92]. The blue shaded areas indicate vibrational and rotational excitation of the respective molecular fragment.

Expected fragmentation pathways

In the following the energy levels associated with the different break-up pathways will be discussed. At first the channels triggered either by outer or inner valence

ionization are considered (indicated by black lines). The simplest fragmentation scenario arises in case of a two-body break-up, like $\text{H}^+ + \text{H}_2\text{O}^+$ ((1)-(3)) or $\text{H}_2^+ + \text{OH}^+$ (6). The number in parenthesis indicates the respective channel number used in the level scheme of fig. 5.2.

The level energy of ch. ((1)-(3)) is exemplarily calculated, for all other channels the same principle is used. In case H_2O the proton affinity is $E_{(\text{H}_3\text{O}^+ \rightarrow \text{H}_2\text{O} + \text{H}^+)} = 7.2 \text{ eV}$ [Hun98] and the ionization potential is $E_{(\text{I}, \text{H}_2\text{O})} = 12.6 \text{ eV}$ [Nist]. With the excited state energies of $E_{(\text{H}_2\text{O}^+ (\text{A}^2\text{A}_1))} = 1.7 \text{ eV}$ and $E_{(\text{H}_2\text{O}^+ (\text{X}^2\text{B}_1))} = 4.6 \text{ eV}$ the energy of the two-body break-up pathways, leaving the molecular fragment in its vibrational and rotational ground state, can be determined via

$$E_0(\text{H}^+ + \text{H}_2\text{O}^+(\text{X})) = E_{(\text{I}, \text{H}_2\text{O})} + E_{\text{H}_2\text{O}^+(\text{X})} + E_{(\text{H}_3\text{O}^+ \rightarrow \text{H}_2\text{O} + \text{H}^+)}, \quad (5.3)$$

where $E_{\text{H}_2\text{O}^+(\text{X})}$ reflects the respective electronic excitation of the charged water molecule, which yields $E_0(\text{H}^+ + \text{H}_2\text{O}^+(\text{X}^2\text{B}_1)) = 19.8 \text{ eV}$ ch.(1), $E_0(\text{H}^+ + \text{H}_2\text{O}^+(\text{A}^2\text{A}_1)) = 21.5 \text{ eV}$ ch.(2) and $E_0(\text{H}^+ + \text{H}_2\text{O}^+(\text{B}^2\text{B}_2)) = 24.4 \text{ eV}$ ch.(3).

The dissociation energy of H_2^+ is $E_{\text{D}, \text{H}_2^+} = 2.6 \text{ eV}$ [Bal92] and the proton affinity of OH is $E_{\text{H}_2\text{O}^+ \rightarrow \text{OH} + \text{H}^+} = 6.1 \text{ eV}$ [Hun98]. In combination with the ionization potential of H with $E_{\text{I}, \text{H}} = 13.6 \text{ eV}$ and the one of OH with $E_{\text{I}, \text{OH}} = 13.0 \text{ eV}$ the level energy of the two body channel $\text{H}_2^+ + \text{OH}^+$ is determined to be $E(\text{H}_2^+ + \text{OH}^+) = 22.7 \text{ eV}$.

As indicated in fig. 5.2 various three-body break-up channels can arise. If the charged water fragment dissociates further, either a neutral OH is accompanied by two H^+ fragments (c.f. fig. 5.2 ch. (4) and (5)), or OH^+ is formed together with a H^+ and a neutral H (c.f. fig. 5.2 ch. (7)).

The ground ($\text{OH}(\text{A}^2\Sigma^+)$) and first excited state ($\text{OH}(\text{X}^2\Pi)$) of neutral OH are separated by 4.1 eV, which yields $E_0(\text{H}^+ + \text{H}^+ + \text{OH}(\text{X}^2\Pi)) = 25.9 \text{ eV}$ ch.(4) and $E_0(\text{H}^+ + \text{H}^+ + \text{OH}(\text{A}^2\Sigma^+)) = 30.0 \text{ eV}$ ch.(5).

To derive the energy level of the break-up pathway $\text{OH}^+ + \text{H}^+ + \text{H}$, one has to take the ionization potentials of OH (13 eV) and of H (13.6 eV) into account. Since in comparison to neutral H, less energy is required to ionize the OH molecule, the energy level is reduced by 0.6 eV.

With respect to ch. (6) and (7) the energy of ch. (9) and (10) is elevated by the proton affinity of neutral oxygen of $E_{(\text{OH}^+ \rightarrow \text{O} + \text{H}^+)} = 5 \text{ eV}$.

The chs.(8,11,12) indicate the pathways which may open for inner valence shell ionization. Due to an Auger decay, prior to the dissociation, the dication may release another electron (c.f. sec. 2.1.2). Thus three excess charges are shared among the

different fragments. Relative to ch. (7) and (10) the ionization energy of neutral H and O is required to populate pathway (8),(11) and (12), when the neutral oxygen and hydrogen are assumed to be in their electronic ground state.

5.3 Fragmentation

The experiment has been split into two parts. In the first phase the fragmentation was investigated, the thereby obtained findings are discussed in the present section. The second part of the experiment was devoted to the electron spectroscopy measurements, the corresponding results are given in sec. 5.4.

5.3.1 Experimental parameters

The experiment was carried out at the fast ion beam infrastructure TIFF (c.f. sec. 3.1). The dc current of 10 nA of the H_3O^+ ion beam corresponds for a kinetic energy of 4.2 keV to a linear particle density of $n_l = 3 \cdot 10^2 \text{mm}^{-1}$. An average FLASH energy of 30 μJ per pulse was measured with the GMD-tool¹. The transmission of the PG 2 beam line, of about $T_{\text{PG}2} \approx 0.5$ for photons in the energy range of 38-90 eV [Mar06] yields an energy of 15 μJ per FEL pulse, corresponding to $N_\gamma = 1.6 \cdot 10^{12}$ photons in the interaction region. The height of the ion and photon beam was determined with the beams' overlap scanner to be 1.8 mm and 1.5 mm (RMS). The horizontal width of the laser beam of about 0.9 mm (RMS) yields a total number of approximately 270 ions which were irradiated with one FEL pulse.

The electrostatic mirror-unit (c.f. sec. 3.1.3) was set such that singly charged ionic break-up products with a kinetic energy of 3.5–4.0 keV, corresponding to $\text{H}_n\text{O}^+ (n = 0..2)$, could reach DET 3. In [Ped09] it has been found that the binary break-up $\text{H}_2\text{O}^+ + \text{H}^+$ channel is associated with a total kinetic energy release of up to 10 eV with a major contribution around 4.5 eV and an asymmetry parameter of $\beta = 2$. As illustrated in fig. 3.10 such a dynamic range and β parameter manifests an expected transmission (see sec. 3.1.3) of the electrostatic mirror-unit of $T_M = 0.6 - 0.8$.

¹Gas monitor detector, installed in the photon beam line to monitor the FEL intensity and position [Tre05].

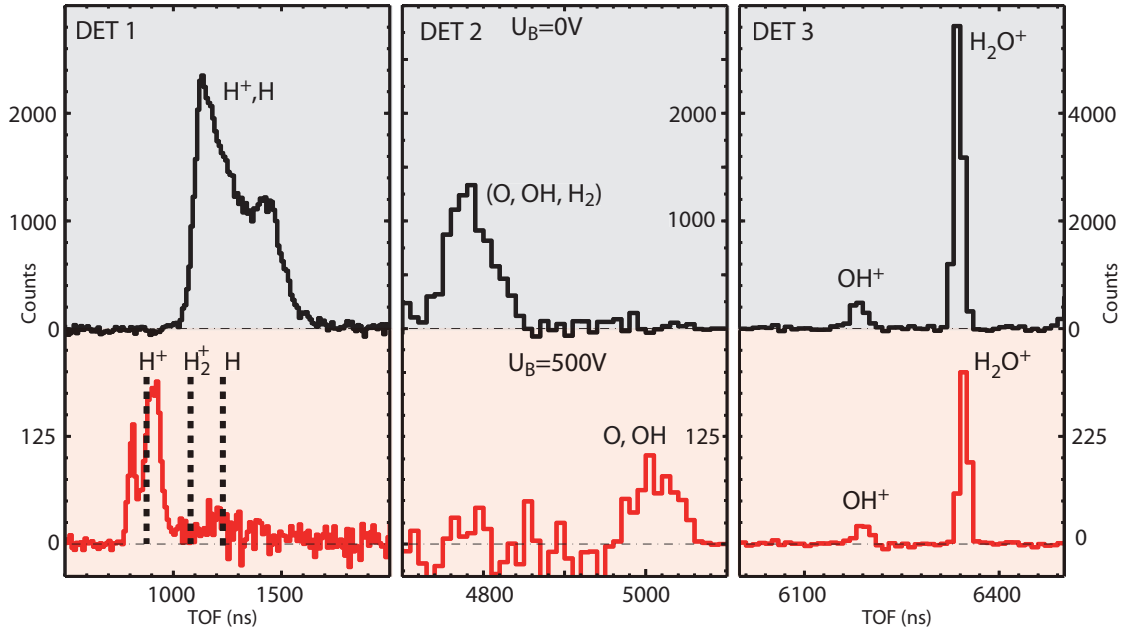


Figure 5.3: Time-of-flight distribution of signal events on DET 1-3 after background correction for $U_B = 0$ V (gray shaded) and $U_B = 200$ V (red shaded). The major contribution on DET 1 stems from H^+ , on DET 2 from OH , and on DET 3 from OH^+ and H_2O^+ , respectively.

5.3.2 Fragment assignment

In fig. 5.3 the time-of-flight distributions of the signal events on the three fragment detectors DET (1–3) are shown. The gray shaded spectra were taken with no potential barrier $U_B = 0$ applied to the interaction region. For fragment assignment the central electrodes of the spectrometer were lifted to a potential of $U_B = +500$ V, depicted in the lower row of fig. 5.3. By this, a certain shift on the fragment arrival time depending on its charge-to-mass ratio can be imposed (c.f. sec. 3.2.1). In more detail, a neutral fragment on DET 2 appears at a later arrival time since the parent ion beam is decelerated when entering the interaction region (c.f. eq. (3.2)). In contrary, charged reaction products on DET 1 gain energy (c.f. eq. (3.3)) while leaving the biased interaction region and arrive at earlier times (c.f. fig. 5.3). The fragments observed with DET 3 impinge at about the same time-of-flight, since in case of the biased interaction zone the energy gain of the ionic products is compensated by a longer path through the mirror.

The signal on the first detector can be determined to stem mostly from H^+ with some contribution of neutral H ($\leq 7\%$). Whereas no H_2^+ induced signal is observable on

DET 1. The dashed black lines indicate the expected arrival time of the respective fragment species. The signal on the second detector originates from heavy neutral fragments. Which can be either O, OH or H₂. The third detector clearly exhibits to separated contributions, which can be unambiguously attributed to OH⁺ and H₂O⁺, respectively and no significant contribution of O⁺. The mirror was also operated in a mode, transmitting higher fragment masses towards DET 3. By this, no additional ionic reaction product could be identified.

5.3.3 Fragmentation pathways

At first, the absence of particular fragment species allows for the exclusion of some of the pathways indicated in the level scheme in fig. 5.2. Since no O⁺ induced signal is observable, ch. (9) and (12) can be ruled out. For a H₂⁺ fragment to reach DET 1 at least a kinetic energy of $E_{\text{KIN,H}_2^+} = 0.8 \text{ eV}$ ($U_B = 500$) is required. As illustrated in fig. 5.2 ch. (6) and (9) are associated with a kinetic energy release of about 3.5 eV sufficient for a H₂⁺ fragment to reach DET 1. Thus these pathways can also be excluded.

To further identify the dissociation pathways, coincidence cuts are applied to the signals of the different detectors (see fig. 5.4). For that purpose a time window is set around a certain fragment species and within that window the events observed for the same FEL pulse on the respective other detectors are determined (c.f. sec. 3.5).

H₂O⁺producing pathway: The clear correlation between charged water and H⁺ can be interpreted as a signature of a dominant binary break-up pathway H₂O⁺ + H⁺ feature (1) in fig. 5.4.

Heavy neutral fragment: The correlation between hits on DET 1 and the neutral signal of DET 2 (feature (2)), can be interpreted to originate from a three-body break-up channel, where a neutral OH formed. A further separation of OH into O and H (ch.10 and 11) would lead to a significantly increased neutral H induced signal on DET 1, which is not observable.

OH⁺producing pathway: Since no H₂⁺ induced signal has been found, the OH⁺-fragments have to be produced in a three-body break-up channel. Unfortunately the statistics acquired in the measurement with biased interaction region is not sufficient to decide whether OH⁺ + H + H⁺ or OH⁺ + H⁺ + H⁺ is prevailing (ch. (7) or (8) fig. 5.2) since the major part of H⁺ is produced in H₂O⁺ + H⁺. However, the electronic signal

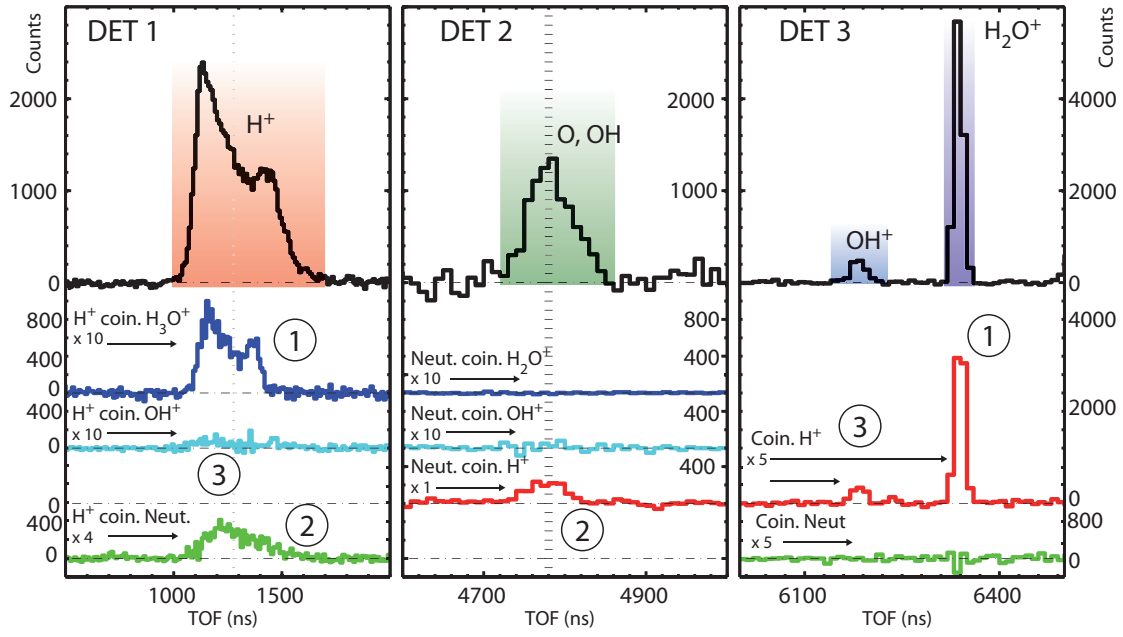
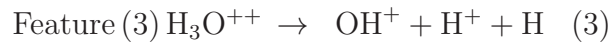
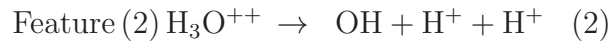
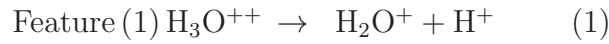


Figure 5.4: Coincident time-of-flight distribution of signal events on DET 1-3. The green lines represent events on DET 1 and 3 which occur in coincidence with neutral OH on DET 2. The cyan and blue colored lines represent events on DET 1 and 2, which appear in coincidence with OH^+ or H_2O^+ , respectively.

as it will be presented in sec. 5.4 does not reveal any contribution of an electron ionized from an inner valence orbital. Since for ch. (8) the opening requires such a vacancy, this pathway can also be excluded.

With these findings the following break-up channels can be identified:



The existence of the first and second break-up channel, has already been stated in [Ped09] for dissociative photoionization of H_3O^+ at a wavelength of 13.5 nm. The discussion given in [Ped09] mentions the possibility of a OH^+ containing channel, which due to the limitations of the detector arrangement, was experimentally not accessible.

Branching of fragmentation pathways

As it was pointed out in the previous section, each of molecular fragment species is produced in one individual break-up pathway. The total number of break-up events is therefore given by the sum over all molecular hits observed with DET 1 and DET 3. To determine the real number of signal hits of each species $F \in \{\text{OH}, \text{OH}^+, \text{H}_2\text{O}^+\}$, the number of observed signal hits $\mathbf{N}_{(F)}$ has to be weighted by the efficiency of the respective detection unit, i.e. for fragments observed on DET 3, the transmission of the mirror-unit T_M has additionally to be included. The total number of break-up events can thus be computed via $N_{\text{total}} = N_{\text{H}_2\text{O}^+}/(T_M\epsilon_3) + N_{\text{OH}^+}/(T_M\epsilon_3) + N_{\text{OH}}/(\epsilon_2)$. To derive the transmission of the mirror-unit, as prevailing during the experiment the observed coincidence between the charged water induced signal of DET 3 and DET 1 can be used. The probability to detect two hits in coincidence on different detectors is proportional to the product of their detection efficiencies. For events on the DET 1 the geometrical detection efficiency G_β [Ped09] and for impacts on DET 3 the transmission of the mirror has to be taken into account. Since the efficiencies of the detectors are known parameters, it is possible to derive the T_M . In total $\mathbf{N}_{\text{H}_2\text{O}^+} = 12 \cdot 10^3$ H_2O^+ fragments have been detected on DET 3. These events were accompanied by $N_{(\text{H}^+, \text{coin.}, \text{D3}, \text{D1})} = 1500$ coincident H^+ fragments on DET 1. The transmission of the mirror can be computed according

$$T_M = N_{(\text{H}^+, \text{coin.}, \text{D3}, \text{D1})} / (\mathbf{N}_{\text{H}_2\text{O}^+} G_\beta \epsilon_1 \epsilon_3). \quad (5.4)$$

With the detection efficiencies of $\epsilon_1 = 0.5 \pm 0.1$, $\epsilon_3 = 0.5 \pm 0.1$ and the geometrical factor $G_{\beta=2} = 0.7$ the transmission of the mirror can be calculated to be $T_M = 0.8 \pm 0.2$. For events on DET 3, $f_{(F)} = \mathbf{N}_F / (T_M \epsilon_3 N_{\text{total}})$ ($F = (\text{OH}^+, \text{H}_2\text{O}^+)$) and on DET 2 $f_{(F)} = \mathbf{N}_F / (\epsilon_3 N_{\text{total}})$ ($F = (\text{OH})$) the relative branching can be stated to be $f_{\text{H}_2\text{O}^+} = 0.65 \pm 0.35$, $f_{\text{OH}} = 0.28 \pm 0.15$ and $f_{\text{OH}^+} = 0.08 \pm 0.08$. The total number of observed molecular fragments yields an integrated count rate of about 9.6 ± 0.7 events per 100 laser shots.

5.3.4 Photofragment momentum imaging

The analysis of the kinetic energy release offers the possibility to obtain the initial state from which the fragmentation process started, and to assign the final state of

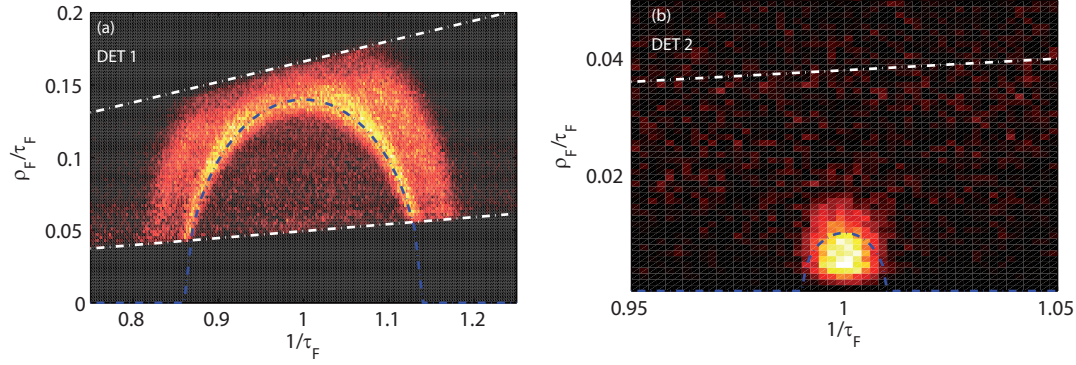


Figure 5.5: Background corrected, normalized momentum spheres of all events on DET 1 (a) and DET 2 (b).

the molecular break-up products. For that purpose the momentum change of the products in the center-of-mass frame has to be known. In the current experimental setup, the first and second detector provide position resolution for a kinematical analysis of the break-up events.

In fig. 5.5(a), the momentum sphere of all H^+ events (with only a 7% contribution of neutral H) on DET 1 is shown. The momentum vectors are normalized to the ion-beam velocity according to $\rho_F = R_F/L_1$ and $\tau_F = T_F/L_1 v_0$ (c.f. sec. 2.2.1), with L_1 being the distance between the interaction point and surface of DET 1. The normalized longitudinal and transversal center-of-mass velocities are $1/\tau_F$ and ρ_F/τ_F (c.f. sec. 2.2.1). As discussed in sec. 3.1.2, the shape of the first detector limits the detection of the photofragments to those, which are emitted in an explosion cone with an opening angle of ($38 \text{ mrad} \leq \theta_F \leq 150 \text{ mrad}$). The inner, dashed white line marks the detection limit which is imposed by the central hole, whereas the upper line indicates the outer edge of the detector. Besides the clear limits due to the inner hole, also part of the events which are preferably emitted in transverse direction (longitudinal momenta ranging from ($1/\tau_F \approx 0.85..1.15$)) escape from detection.

The kinetic energy release of a two-body break-up is only shared among two fragments. If only one of the two break-up products is observed, like H^+ formed in channel (1) (see previous section) momentum conservation forces them to appear on a ring-shaped momentum distribution, with a radius given in eq. (2.20). The well pronounced sphere with $\sqrt{(1/\tau - 1)^2 + (\rho/\tau)^2} \approx 0.14$ indicates that these events originate from the binary break-up channel.

If the energy is distributed among more than two products, no clear kinematical correlation determines the amount of energy which is taken away by one fragment. Thus, the events which are distributed within $\sqrt{(1 - 1/\tau)^2 + (\rho/\tau)^2} \leq 0.12$ can be

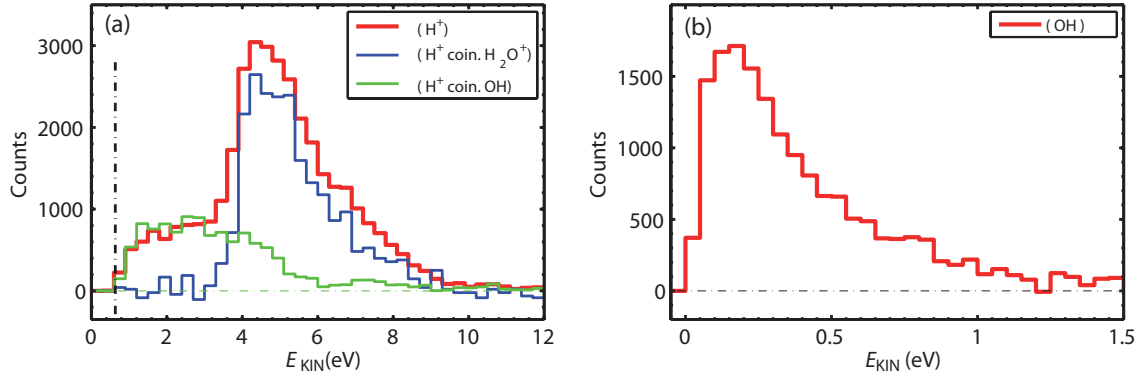


Figure 5.6: (a): Kinetic energy of all events on DET 1 after background correction (red line). The blue curve represents the kinetic energy release of the events which can be attributed to the two-body break-up. The green curve represents the events, which are detected in coincidence with neutral OH. (b): Kinetic energy release of all events on DET 2.

assigned to stem from a three-body break-up process.

The normalized momentum sphere of neutral fragments on DET 2 is shown in fig. 5.5 (b). These fragments are identified as OH (see sec. 5.3.3) which yields $\rho_{\text{OH}} = R_{\text{OH}}/L_2$ and $\tau_{\text{OH}} = T_{\text{OH}}/L_2 v_I$, where the drift length to the second detector is expressed by L_2 . The white dashed line indicates the outer limit of the effective detection area, which is defined by the central hole of the first detector, (c.f. fig. 3.7). It is obvious that the second detector is fully sensitive to all events, which are, as indicated by the dashed blue line, confined within a circle. The absence of any ring-shaped structure underlines the assumption that the neutral fragments emerge in a break-up process with more than two products.

The center-of-mass kinetic energy of the fragments, impinging on the imaging detectors DET 1 and DET 2, can be obtained via $E = p_F^2/2m_F$ with $(F \in \{\text{H}^+, \text{OH}\})$. The energy spectrum of all events of the first detector is shown in fig. 5.6 (a). Due to the central hole, the distribution has a cut-off for fragment energies smaller than 0.7 eV, indicated by black dashed line. The spectrum exhibits a dominant feature around 4.3 eV and extends up to 10 eV. To disentangle the contribution of the different channels, the kinetic energy of the H^+ -fragments, detected in coincidence with either H_2O^+ or OH, is determined. The resulting distributions (green and blue curve), shown in fig. 5.6 are normalized such that the sum of both reflects the kinetic energy distribution of all fragments of DET 1. These findings illustrate that the kinetic energy of the H^+ fragments stemming from the three-body break-up channel, $\text{OH} + \text{H}^+ + \text{H}^+$ dominates the energy distribution from $(0.7 \text{ eV} \leq E \leq 4.0 \text{ eV})$. Within the energy range $(4.0 \text{ eV} \leq E \leq 5 \text{ eV})$ the binary as well as the three-body

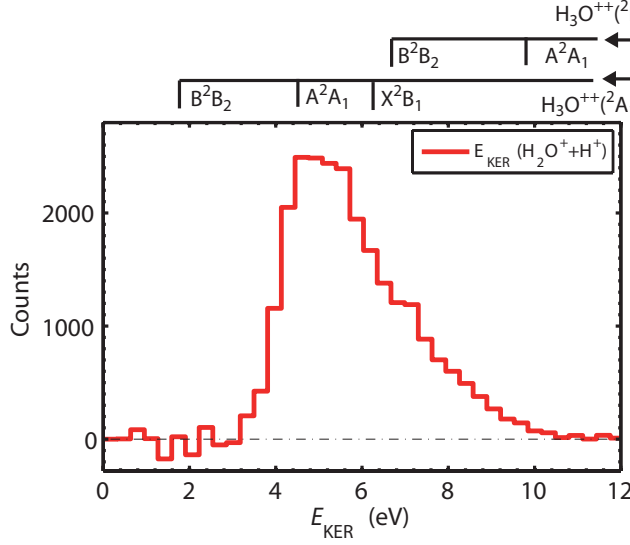


Figure 5.7: Kinetic energy release of two-body break-up. The tick marks on the upper abscissae indicate the expected KER of the binary break-up channel $\text{H}_3\text{O}^{++} \rightarrow \text{H}_2\text{O}^+ + \text{H}^+$ (c.f. fig. 5.2).

channel contribute.

The kinetic energy of all neutral fragments on DET2 is depicted on the right of fig. 5.6. The distribution features a maximum around 0.15 eV and is extended to 1 eV. In the following sections a detailed discussion of the channel resolved kinetic energy release is given.

Two-body break-up

In the previous section, the kinetic energy spectra of the signal events on the imaging detectors have been shown. Since the 3D-coordinates of the H^+ -events, which can be assigned to be produced in the binary break-up channel are available, the correlation $\vec{p}_{\text{H}_2\text{O}^+} = -\vec{p}_{\text{H}^+}$ yields the center of mass momentum of the charged water fragment. By this, the kinetic energy release (KER) of the two-body break-up $\text{H}_3\text{O}^{++} \rightarrow \text{H}_2\text{O}^+ + \text{H}^+$ can be calculated as $E_{\text{KER}(\text{H}_2\text{O}^+ + \text{H}^+)} = p_{\text{H}^+}^2 (1/2m_{\text{H}^+} + 1/2m_{\text{H}_2\text{O}^+})$ (see. eq. (2.19)). Fig. 5.7 displays the resulting KER spectrum of the binary fragmentation pathway. The distribution features a sharp onset at 4 eV and a maximum at around 4.6 eV. The extension of the distribution down to about 10 eV is associated with a small shoulder at 6.6 eV kinetic energy. The tick marks on the upper abscissae indicate the kinetic energy release for either of the reactions, $(\text{H}_3\text{O}^{2+}(^2\text{A}_1) \rightarrow \text{H}^+ + \text{H}_2\text{O}^+(\text{B}^2\text{B}_2, \text{A}^2\text{A}_1, \text{X}^2\text{B}_1,))$ with $E_{\text{KER}} = (2, 4.5, 6.2)$ eV and $(\text{H}_3\text{O}^{2+}(^2\text{E}) \rightarrow \text{H}^+ + \text{H}_2\text{O}^+(\text{B}^2\text{B}_2, \text{A}^2\text{A}_1))$ with $E_{\text{KER}} = (6.2, 9.7)$ eV, where the products as well as the reactants are assumed to be in their vibrational and rotational ground states.

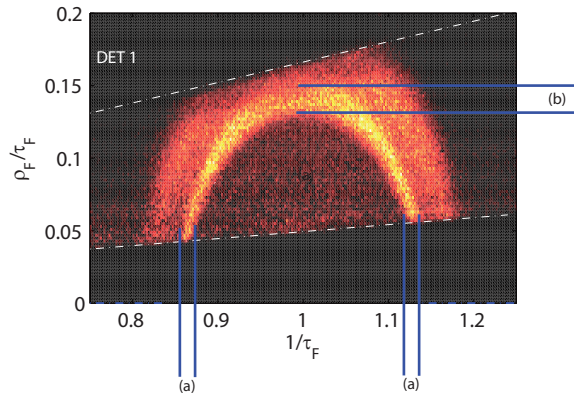


Figure 5.8: Illustration of nonlinearity of DET 1, which becomes important for particles preferably emitted in transverse direction (b).

In sec. 5.5 the photofragment spectrum is further discussed, with respect to different prospects regarding the internal excitation of H_2O^+ .

In the following, the dominating mechanisms which may lead to a broadening of the kinetic energy release distribution for specific reactant and product states are pointed out. First of all the interaction between photon and ion beam can take place at any point within the interaction volume rather than in a well-defined interaction point. The volume is spanned by the finite width of the ion and photon beam of about 1.5 mm and 1.8 mm, respectively. In case of H_3O^+ , with a kinetic energy of ≈ 4.2 keV, and under the assumption of Gaussian shaped ion and photon beam profiles a broadening of $\pm\Delta E = \pm 0.3$ eV can be estimated. Moreover, the non-linearity of the first detector should also be mentioned. This effect becomes only important for those fragments which are emitted in transverse direction and depends on the radial impact position. Fig. 5.8 displays the effect of the nonlinear behavior of the detector for transversally emitted fragments (b) in comparison to forward and backward emitted particles (a). Since no detailed investigation of that effect is available, an upper limit can be estimated to be $\Delta(\rho_F/\tau_F)/(\rho_F/\tau_F) \leq 0.05$. This yields for transversally emitted particles with a kinetic energy of ~ 4.5 eV an energy increase less than 0.4 eV.

Three-body break-up

In the upcoming paragraph the kinematics of the three body break-up, $\text{OH} + \text{H}^+ + \text{H}^+$, are discussed. In fig. 5.6 the momentum distribution of the OH fragments on DET 2 clearly reveals that geometrically these events are fully detected on the second detector. In addition the light charged fragments are covered with high geometrical efficiency on DET 1. A kinematical analysis of the three-body break-up process re-

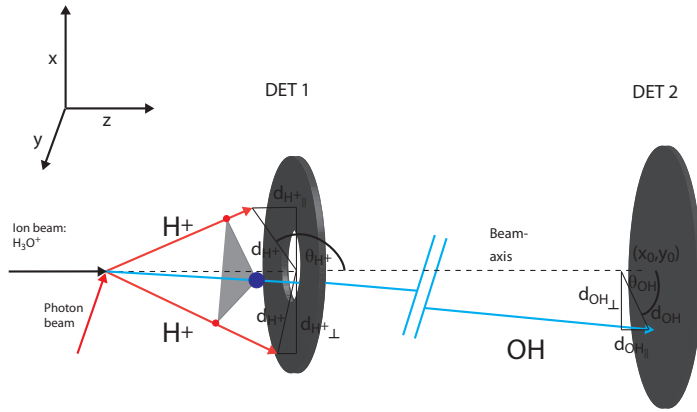


Figure 5.9: Schematic of the three body break-up in case of photodissociation of H_3O^{++} in $\text{OH} + \text{H}^+ + \text{H}^+$ and serial detector arrangement.

quires a unique assignment of corresponding events on both detectors (see fig. 5.9). For this purpose, events with at least two hits per FEL pulse on DET 1 (H^+) and one further coincident hit on DET 2 (OH) are extracted and the center-of-mass velocity is determined. By applying a center of mass velocity cut the true events, stemming from a single three-body break-up process can, be unambiguously assigned.

Once the appropriate hits on both detectors are found, the total center of mass kinetic energy release (KER) is calculated according to $E_{\text{KER}} = E_{\text{KIN, OH}} + E_{\text{KIN, H}^+} + E_{\text{KIN, H}^+}$. In fig. 5.10 the KER-spectrum of the three-body break-up is shown. The distribution features a maximum at about 5.5 eV. The tick marks on the upper abscissae indicate the expected KER if the three-body break-up is initiated by a valence vacancy in the $3a_1$ orbital and the hydroxyl radical OH is produced in its electronic ground $\text{OH}(\text{X}^2\Pi)$ and first excited $\text{OH}(\text{A}^2\Sigma^+)$ state, $(\text{H}_3\text{O}^{++}({}^2\text{E}) \rightarrow \text{H}^+ + \text{H}^+ + \text{OH}(\text{A}^2\Sigma^+, \text{X}^2\Pi))$ with $E_{\text{KER}} = (1.2, 5.3)$ eV. A detailed discussion of the photofragment spectrum is given in sec. 5.5.

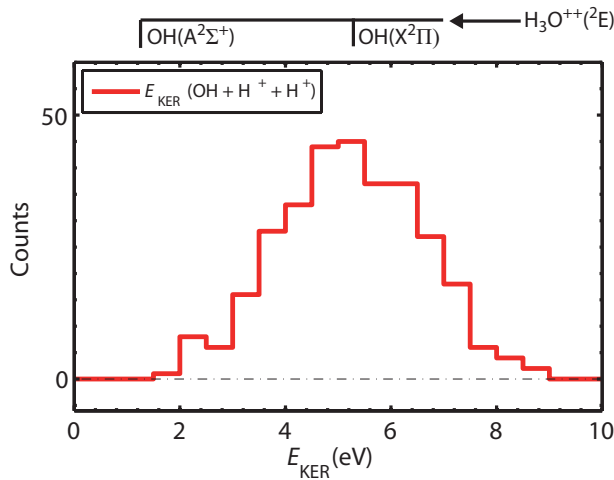


Figure 5.10: Kinetic energy release of three body break-up channel: $\text{H}_2\text{O}^+ + \text{H}^+ + \text{H}^+$. The tick marks on the upper abscissae indicate the expected KER of the three-body break-up channel, $\text{H}_3\text{O}^{++} \rightarrow \text{OH} + \text{H}^+ + \text{H}^+$ (c.f. fig. 5.2).

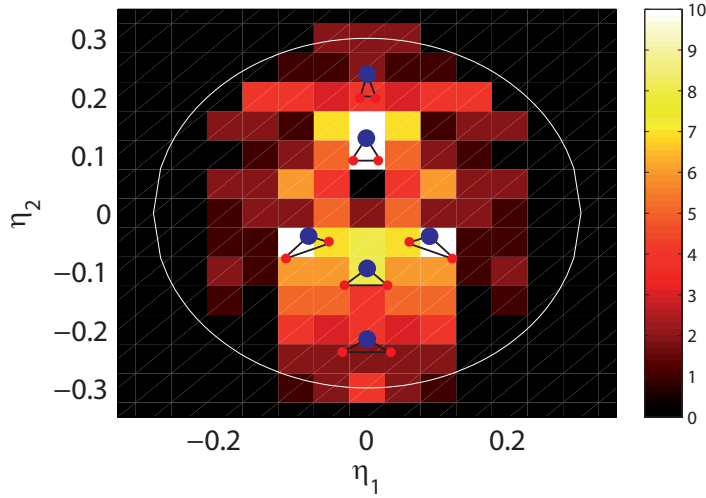


Figure 5.11: Dalitz plot of the three body break-up of H_3O^+ into $\text{OH} + \text{H}^+ + \text{H}^+$. The break-up geometry of the system is indicated by small triangles, where the blue point represents the OH complex, and the red points express the H^+ fragments.

The Dalitz coordinates, which have been introduced in sec.2.2.1, can be used to represent the geometry of the three-body break-up. Fig.5.11 displays the event distribution within the Dalitz plane as it is obtained for the dissociative photoionization of H_3O^+ . The energy sharing between the H^+ fragments defines the position of an event along the η_1 axis. Events, where both H^+ products carry the same amount of energy, are located along the $\eta_1 = 0$ line. Since the H^+ fragments, are un-distinguishable, the Dalitz plot exhibits a mirror symmetry with $\eta_1 = 0$ as the reflection axis. The η_2 axis represents the amount of kinetic energy carried by the OH fragment. For $(\eta_1, \eta_2) = (0, 1/3)$ the OH fragment carries the largest amount of energy, in contrast to $(\eta_1, \eta_2) = (0, -1/3)$, where the OH fragment stays at rest. Thus, the center of the Dalitz plane represents the events where the energy is equally shared among the products.

Unfortunately the statistic, as it was acquired during 3h of data taking time is strongly limited, which makes a rather rough binning necessary. In spite of the limited statistics, some tentative conclusions on the break-up geometry can be drawn. The distribution shows that for a large number of events the energy is equally shared among the H^+ fragments. Moreover, only a few processes occur where the OH fragment stays either at rest ($\eta_2 = -1/3$) or takes the maximum amount of kinetic energy ($\eta_2 = 1/3$). In addition, the observed pattern exhibits that basically none of the fragmentation process proceeds with $(\eta_1, \eta_2) = (0, 0)$. Two areas within the Dalitz plane carry the major part of the intensity. The one centered around $(\eta_1, \eta_2) = (0, 0.15)$ expresses processes with an angle of $50^\circ \leq (\angle_{\text{OH}}^{\text{H}^+}) \leq 70^\circ$ between the light charged fragments. The majority of events appear with $-0.25 \leq \eta_2 \leq -0.05$, which indicates that break-up processes with an angle of $100^\circ \leq (\angle_{\text{OH}}^{\text{H}^+}) \leq 130^\circ$ are preferred.

The position of an event along the η_2 axis depends on the relative fraction of the total kinetic energy release, which is carried by the molecular fragment. Hence, for break-up processes which appear with $-0.25 \leq \eta_2 \leq -0.05$ less than half of the maximal relative kinetic energy of $2m_{\text{H}}/M \approx 12\%$ of the total KER is transformed into translational motion of the OH fragment.

Absolute cross section

The second detector is fully sensitive to all neutral OH fragments (c.f. fig. 5.10(b)) allowing to estimate the absolute cross section of the neutral OH containing break-up channel. The observed number of OH fragments N_{OH} has to be weighted by the multi-channel plate efficiency of DET 2 given by $\epsilon_2 = 0.5 \pm 0.1$. Additionally the transmission of the PG 2 photon beam line $T_{\text{PG}2} = 0.4 \pm 0.1$ has to be considered to determine the average number of photons per pulse N_γ . The convolution factor can be determined to be $F = (5.5 \pm 1.0) \text{ cm}^{-1}$. In combination with the linear density n_{I} , the cross section is calculated according to eq. (2.30) to be $\sigma_{\text{OH}+2\text{H}^+} = (0.32 \pm 0.16) \cdot 10^{-18} \text{ cm}^2$, whereas in [Ped09] a $\sigma_{\text{OH}+2\text{H}^+} = (0.37 \pm 0.18) \cdot 10^{-18} \text{ cm}^2$ has been reported (see sec. 5.5). A detailed discussion of the error bar on the cross section, mainly dominated by the photon flux delivered to the experiment, is provided in [Ped09]. The relative strength of the OH fragment containing channel was found to be $f_{\text{OH}+2\text{H}^+} = 0.28 \pm 0.15$ (see sec. 5.3.3) resulting in an absolute cross section for all break-up events of $\sigma = (1.2 \pm 0.8) \cdot 10^{-18} \text{ cm}^2$.

5.4 Photoelectron spectroscopy

In the previous section the three dominating break-up channels of H_3O^+ have been identified. It has been shown that the break-up proceeds from H_3O^{++} into a dominant binary and two three-body break-up channels. In the upcoming paragraph the electronic signal is correlated to certain ionic break-up products and the thereby obtained distributions are modeled by a Monte-Carlo simulation.

5.4.1 Experimental parameters

The expected kinetic energy of an electron photoionized from the ($1e$) orbital ($E_\gamma = 56.7 \text{ eV}$) is $E_{(\text{k}, 1e)} = 25.5 \text{ eV}$ and for the ($3a_1$) orbital with $E_{(\text{k}, 3a_1)} = 30.7 \text{ eV}$. An

electron ionized from the $2a_1$ inner valence orbital appears with a kinetic energy $E_{(k, 2a_1)} = 7.4 \text{ eV}$. The major constituent of the residual gas H_2 has an ionization threshold of 15.4 eV [Nist] which leads to a kinetic energy of an electrons photoionized from H_2 of $E_{(\text{H}_2)} = 42 \text{ eV}$. Since $T \propto 1/\sqrt{E}$ the time-of-flight of the signal photoelectrons is expected to lie in a region where the background electrons, mainly stemming from the ionization of H_2 are expected to dominate. Under operational conditions a pressure of $p_{\text{int}} = 5 \cdot 10^{-10} \text{ mbar}$ was prevailing in the interaction region. In analogy to eq. (2.28) the residual-gas induced count rate per FEL pulse, can be derived from

$$R_B \approx \sigma_B N_\gamma \left(\frac{p_{\text{int}}}{k_B T} \right) L_{\text{acc.}}, \quad (5.5)$$

where the photoionization cross section σ_B , is dominated by the main constituent of the residual gas, H_2 , with $\sigma_{\text{H}_2} = 1 \cdot 10^{-18} \text{ cm}^2$ for a photon energy of 60 eV . $L_{\text{acc.}}$ expresses the effective length of the acceptance volume of the spectrometer (sec. 3.2). An energy per FEL pulse of $30 \mu\text{J}$, as it was used for the fragmentation measurement, would result in a residual-gas induced count rate of $R_B = 15 \text{ events/pulse}$, which does not allow for electron spectroscopy measurements, based on a pulse counting technique. Therefore the electron spectroscopy was realized in a different phase of the experiment, where the laser was reduced to an energy of $2 \mu\text{J}$ per FEL pulse. Therefore a background induced count rate of about $R_B = 0.8 \text{ events/pulse}$ can be expected. The dc ion beam current was again 10 nA .

The newly installed stray light protection unit S_0 before the refocusing mirror unit (RMU), see sec. 3.2.1, was used to collimate the photon beam to an appropriate diameter and in addition to block the halo around the main beam. The guard system S_1 and S_2 before and after the interaction region was then iteratively closed to minimize the stray light induced noise on the electron detectors. The spectrometer was operated with $C_{1,2} = -144 \text{ V}$ and $U, D_0 = +112 \text{ V}$. As a free parameter, the potential of the drift unit, U_D , was varied between $-25, -30, -45 \text{ V}$. In case of $U_D = -25 \text{ V}$ the dynamic range of the spectrometer covers $E_{k,e-} \in 0..40 \text{ eV}$ and for $U_D = -45 \text{ V}$ only electrons with a kinetic energy in the range of $E_{k,e-} \in 20..40 \text{ eV}$ can reach the detection unit. Since the lower detector could not properly be operated only the signal on the upper detector could be used in the analysis described below.

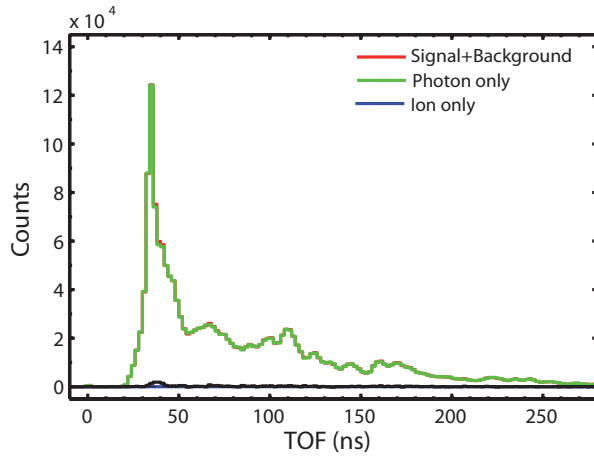


Figure 5.12: Noncoincident electron time-of-flight spectrum on the upper electron detector. The photon-induced background (green line), almost dominates the signal (red curve).

5.4.2 Experimental results

Even though the FEL intensity had been reduced, the signal-to-noise ratio on the electron detector was very low. In fig. 5.12 the electron time-of-flight distribution is shown. Except for a small region around 50 ns, the photon induced background (green curve) almost dominates the complete signal trace (red line). Besides the residual-gas induced background on the electron detectors another reason for the limited signal-to-noise ratio can be seen in the fact that the reduction of the laser intensity resulted in a less stable pointing of the photon beam. This might have negatively influenced the geometrical overlap of the two beams. In contrast to the electron detectors, the signal on the light fragment (DET 1) and heavy charged fragment detector (DET 3) is practically background free. By requiring the electronic signal to appear in coincidence with the signal on one of the low-noise fragment detectors the background could be suppressed and those FEL pulses which had a proper overlap of ion and photon beam could be separated.

5.4.3 Coincidence with light charged fragment

Fig. 5.13 displays the time-of-flight spectra of the electrons towards the upper electron detector, which are detected in coincidence with H^+ . The error bar reflects the statistical uncertainty of the coincident signal. The energy scale as it is depicted on the upper axis of the respective plot in fig. 5.13 is calibrated according to eq. (3.4). The time-of-flight to energy conversion is made under the assumption that the interaction point lies exactly in the saddle point. The electron energies corresponding

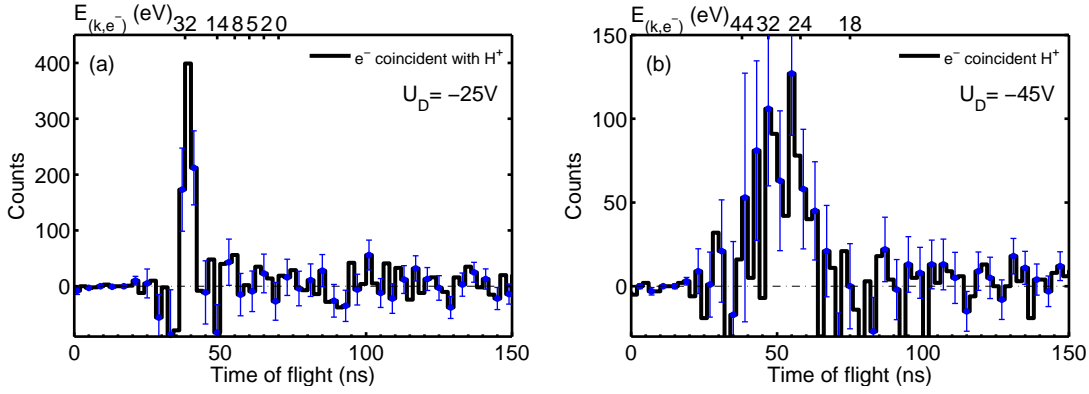


Figure 5.13: Electron time-of-flight spectra for different retarding potentials applied to the drift unit of spectrometer. A potential of $U_D = -45$ V (fig. (b)) yields a separation of the signal into two components in comparison to $U_D = -25$ V (fig. (a)) where no splitting of the signal is obvious.

to the different TOF values for the respective retardation U_D are indicated on the upper abscissa. Consequently, hits which appear in the time-of-flight distribution with a fictive kinetic energy smaller than 0 eV stem from electrons which are created somewhere in the spectrometer.

The spectrum obtained for $U_D = -25$ V (fig. 5.13(a)) features a significant peak around 40 ns. Under such retardation conditions electrons with a kinetic energy of 25 eV up to 34 eV appear in a rather compressed fashion. In contrast in the range where an inner valence electron would be expected around 55 ns (corresponding to 8 eV) no contribution is observable. To further differentiate the electronic signal the potential barrier was increased. As it has been shown in sec. 3.2.1, the energy resolution of the spectrometer for a given saddle point depends on the retarding potential of the drift unit, i.e. the higher $|U_D|$ the better the spectrometer resolution. A deceleration with $U_D = -45$ V indeed leads to a broadening of the electronic signal and an indication of a separation into a fast and a slow component, centered at ~ 48 ns ($E_{(k,e^-)} = 32$ eV) and ~ 58 ns ($E_{(k,e^-)} = 26$ eV), respectively.

In sec. 2.3.2 the physics governing the photoionization process under such conditions have been discussed. There, it has been shown that the motion of the beam imposes a certain width on the electronic signal, which explicitly depends on the ion velocity v_0 . Specifically, an electron which is emitted in beam direction gains energy from the ion beam propagation, whereas the ones which are emitted antiparallel loose energy. Thus, parallel or antiparallel emitted electrons with a kinetic energy of 26 eV in the center-of-mass frame, appear in the laboratory frame with kinetic energies of 24.5 eV and 27.5 eV. In sec. 2.3.2, it has been shown that this effect is not limiting

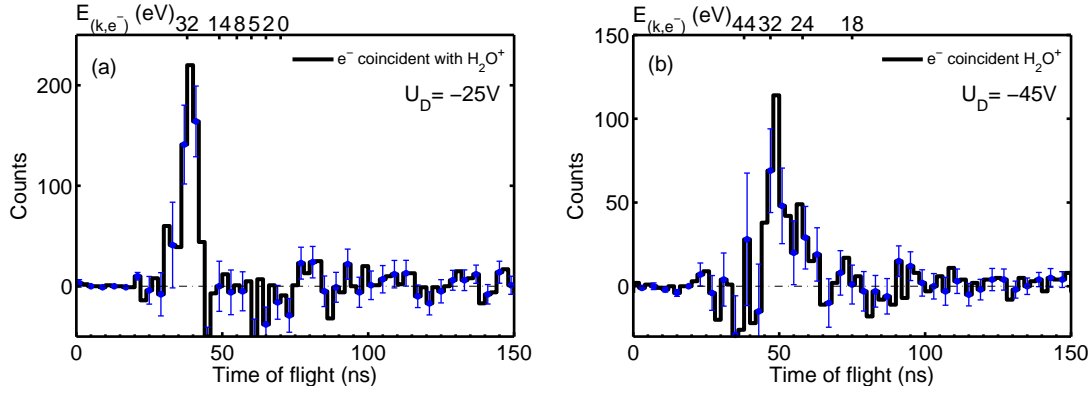


Figure 5.14: Time-of-flight spectra of electrons which are detected in coincidence with H_2O^+ . A retardation with $U_D = -25$ V (fig. (a)), yields a separation of the signal into two components, in comparison to $U_D = -45$ V (fig. (b)) where no splitting of the signal is obvious.

the possible energy resolution. Moreover, the kinematical energy spread of ± 1.5 eV is smaller than the observed width of the peaks, see sec. 5.4.6.

In the following the other processes, which limit the resolution of the spectrometer are illustrated. The widths of ion and photon beam of 1.8 mm and 1.5 mm (RMS) and the gradient of 1 V/mm in the vicinity of the saddle-point can be assumed to impose an additional energy of $\pm \Delta E_S = \pm 0.25$ eV.

The precise spectral distribution of the photon beam was determined with a FLASH beam diagnostics tool, to be $E_\gamma \pm \Delta E_\gamma = 56.7 \pm 0.5$ eV.

Finally the resolution of the data acquisition system on the order of $\Delta T \pm 1$ ns has also be mentioned. For the observed electron energies, $E_e \in [25 \text{ eV}..30 \text{ eV}]$ and a retardation with $U_D = -45$ V, an uncertainty in the time-of-flight of ± 1 ns translates into an $\Delta E_{\text{DAQ}} \approx 1$ eV. Under this retardation conditions and beam parameters the observed electronic line appears broadened by $\Delta E \approx \sqrt{\Delta E_S^2 + \Delta E_\gamma^2 + \Delta E_{\text{DAQ}}^2} \approx \pm 1.15$ eV.

5.4.4 Coincidence with charged water

The dissociative photoionization of H_3O^+ proceeds into three channels with each of them containing at least one H^+ fragment. The coincident electron spectra shown in fig. 5.13 of the previous section therefore represent the integrated electronic signal of all three channels. A further differentiation, i.e., a more channel-specific discussion of the electronic signal can be obtained if the electrons are required to be accompanied by one of the heavier molecular fragments like OH, OH^+ or H_2O^+ on the neutral (DET 2) or heavy charged fragment detector (DET 3). The signal-to-noise ratios of

the neutral fragment detector (DET 2) and the limited statistics of the OH^+ signal (DET 3) do not allow for a direct correlation between the OH or OH^+ break-up products and the electronic signal.

However, in fig. 5.14 the black curve shows the electronic signal which is detected in coincidence with H_2O^+ for two different retarding modes of the spectrometer. In case of $U_D = -45 \text{ V}$ (b) the coincident electron time-of-flight spectrum reveals the heavy charged water to be mainly accompanied by fast electrons with clearly smaller contribution of slow electrons.

Similar to the derivation of equation 5.4 the transmission of the spectrometer T_S can be determined. In total $N_{(e^-, \text{coin.}, D3, E_{\text{up}})} = 440$ signal counts on the upper electron detector are found in coincidence with $N_{\text{H}_2\text{O}^+} = 5900$ H_2O^+ hits on DET 3. Since only the upper detector was operated the electrons which are emitted into the lower hemisphere are lost for detection. Hence the transmission of the spectrometer can be estimated according to

$$T_S = N_{(e^-, \text{coin.}, D3, E_{\text{up}})} / (N_{\text{H}_2\text{O}^+} (0.5 \cdot \epsilon_E \epsilon_3 T_M)). \quad (5.6)$$

With $\epsilon_E = 0.5 \pm 0.1$, $\epsilon_3 = 0.5 \pm 0.1$ and T_M determined in sec. 5.3 the transmission of the spectrometer is $T_S = 0.8 \pm 0.3$, which matches the expected simulated transmission for electron energies in the range of $E_{(k, e^-)} = (26..32 \text{ eV})$ and a retardation of $U_D = -45 \text{ V}$ (see fig. 3.17). Further differentiation of the signal is not possible since a retardation potential beyond $U_D = -45 \text{ V}$ would strongly affect the transmission of the spectrometer.

5.4.5 Double coincidence with light fragments

In case of the two three-body break-up channels $\text{OH} + \text{H}^+ + \text{H}^+$ and $\text{OH}^+ + \text{H}^+ + \text{H}$ the molecular fragment is accompanied by two hits on DET 1. Hence the coincidence requirement that an electron has to be accompanied by two events on the first detector, gives indirect access to the electronic signal of the two three-body break-up channels.

The coincident signal suggests that these channels are mainly accompanied by the less energetic electrons. Based on the intensity ratio of OH and OH^+ fragments a relative branching $R(\text{OH}/\text{OH}^+) \approx 3.5$ has been found. Consequently, the coincident electronic signal as it is observed for the two-fold coincidence with a light fragment

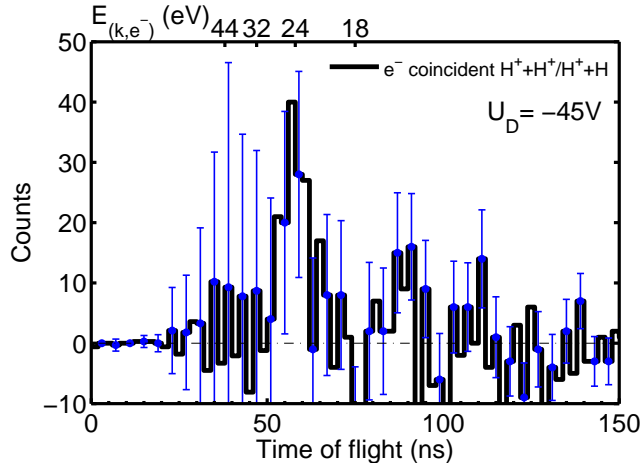


Figure 5.15: Electron time of flight spectra for $U_D = -45 \text{ V}$. The black curve displays the coincident electronic signal, when a coincidence with exactly two hits on DET 1 is required.

on DET 1 is dominated by the neutral OH containing channel.

5.4.6 Monte Carlo Simulation

In the previous section it has been shown that the separation of the electronic signal on the upper electron detector, once an appropriate retardation is applied, supports the assumption that two electrons with different energies are photoionized from the hydronium ion. In order to determine the electron energy, the photoionization process for randomly oriented molecules is modeled with a Monte Carlo Simulation. For a certain asymmetry parameter, the ejection probability into an angle $[\cos \tilde{\theta}, \cos \tilde{\theta} + d \cos \tilde{\theta}]$ is computed according to equation 2.31. The trajectories of photoelectron propagating inside the spectrometer from the interaction region towards the electron detector are computed with SIMION. The photoelectron spectroscopy measurement on H_3O^+ was done with three different retardation modes, $U_D = (-25 \text{ V}, -30 \text{ V}, -45 \text{ V})$. One major problem which might hamper the ability to assign an energy to the observed electronic signal stems from the fact that the crossing point of the ion and photon beams does not exactly lie at the saddle point. To account for this scenario, the electron spectra taken with different retardation potentials have to be included in the simulation. Once an appropriate offset $\Delta \mathbf{x}_s = (\Delta x_s, \Delta y_s, \Delta z_s)$ is found, the only free parameters left in the simulation are the electron energy and asymmetry parameter of the two electrons (E_i, β_i) ($i = 1, 2$). Thus, if a parameter set can be found such that the time-of-flight spectra can be uniquely described with that set, an energy can be assigned to the observed electronic signal. This approach is justified since a variation of the retarding potential on the drift unit of the spectrometer does not affect the position of the saddle point

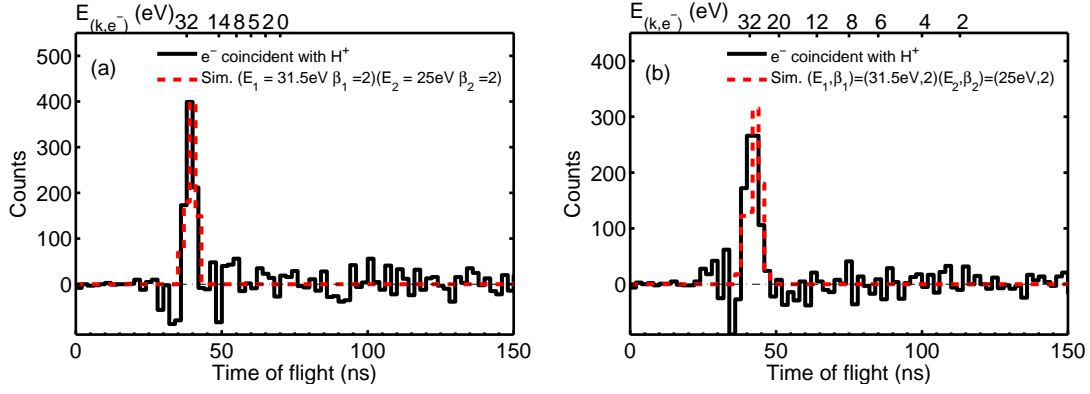


Figure 5.16: The black curves display the measured electron time-of-flight spectra for a retarding potential of $U_D = -25$ V (fig. (a)) and $U_D = -30$ V (fig. (b)). The dashed red line represents the simulated electron time-of-flight distribution, for two electron energies and beta parameters of $(E_1, \beta_1) = (25 \text{ eV}, 2)$ and $(E_2, \beta_2) = (31.5 \text{ eV}, 2)$.

and since the crossing point of ion and photon beam can be assumed to remain stable over time. Thus an absolute calibration of the simulation, under the present experimental conditions can be obtained.

The simulated spectra in fig. 5.16, (red curve) are obtained for a retardation with $U_D = (-25 \text{ V}, -30 \text{ V})$ and for two electron energies of $(E_1, \beta_1) = (25 \text{ eV}, 2)$ and $(E_2, \beta_2) = (31.5 \text{ eV}, 2)$. As it turned from the simulation, the interaction point was in the saddle point, i.e., $\Delta \mathbf{x}_s = (0, 0, 0)$ could be used for these kind of electron energies.

The dashed red line in fig. 5.17 (a) displays the simulated time-of-flight spectrum as is obtained $(E_{(k,e^-)}, \beta_1) = (31.5 \text{ eV}, 2)$. In the right part of fig. 5.17 the red curve expresses the simulation for $(E_{(k,e^-)}, \beta_2) = (25 \text{ eV}, 2)$.

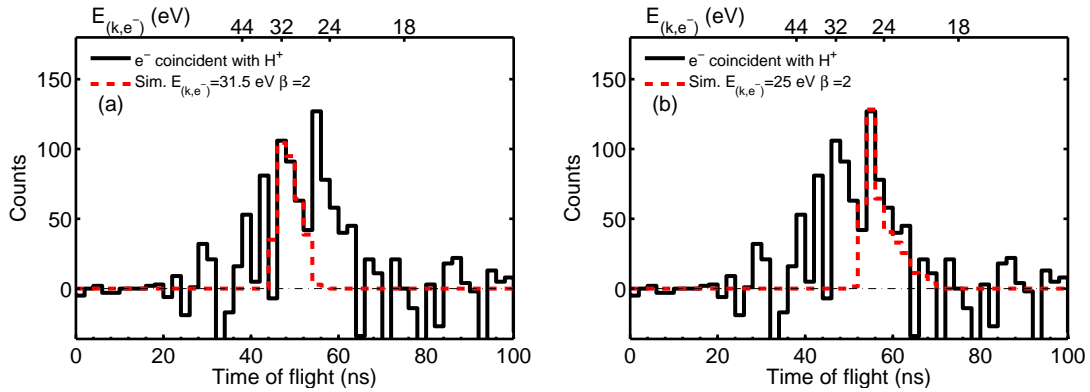


Figure 5.17: Electron time-of-flight spectra for a retarding potential of $U_D = -45$ V applied to drift unit of spectrometer. Dashed red lines represent the simulated electron time-of-flight for $(E_{(k,e^-)}, \beta_2) = (31.5 \text{ eV}, 2)$ (fig. (a)) and $(E_{(k,e^-)}, \beta_1) = (25 \text{ eV}, 2)$ (fig. (b)).

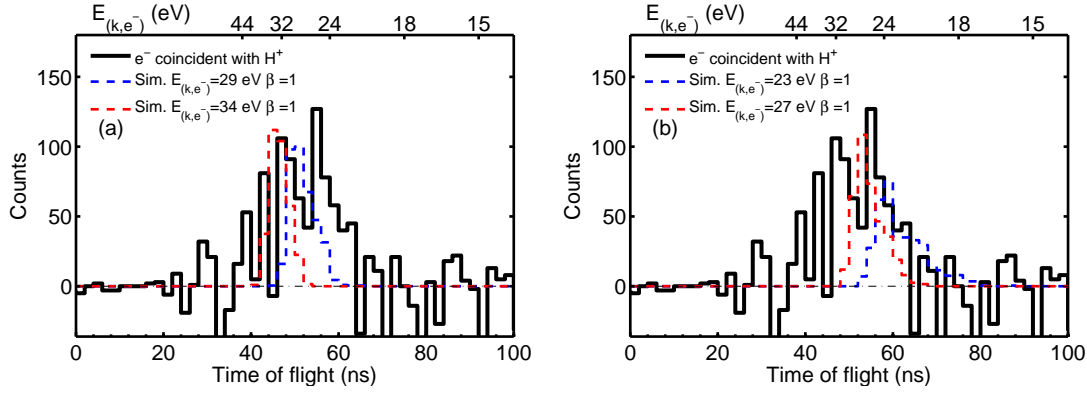


Figure 5.18: Electron time-of-flight spectra for a retarding potential of $U_D = -45$ V. In fig. (a) the red and blue line represent the simulated electron time-of-flight distribution for $(E_{(k,e^-)}, \beta_1) = (34 \text{ eV}, 1)$ and $(E_{(k,e^-)}, \beta_1) = (29 \text{ eV}, 1)$. In fig. (b) the red and blue line represent the simulated electron time-of-flight distribution for $(E_{(k,e^-)}, \beta) = (27 \text{ eV}, 1)$ and $(E_{(k,e^-)}, \beta) = (23 \text{ eV}, 1)$.

A similar representation of the observed time-of-flight spectra could also be obtained if $\beta = 1$ was used in the simulation. The large uncertainty of the asymmetry parameter arises from the very short time-of-flight for these electron energies. In sec. 2.3.2 the effective velocity of the photoelectron has been expressed in terms of the emission angle relative to the laser polarization. Under the present conditions, the kinematics of the photoionization process on a moved target imposes an additional energy of $\approx \pm 1.5 \text{ eV}$ on the kinetic energy of the ejected photoelectron (see sec. 5.4.3). This yields for the drift length of $L_{\text{Drift}} = 0.15 \text{ m}$ a broadening of the expected time-of-flight distribution of $\Delta T \approx 3 \text{ ns}$. Hence under the prevailing conditions the asymmetry parameter β can only be stated in rough boundaries.

Within the above discussed broadening mechanisms the assignment of the electron energy to the respective signal can be considered as rather precise. The uncertainty on the expressed electron energies is hence dominated by the intrinsic energy resolution of the setup of about $\sim 1.2 \text{ eV}$ for these kind of electron energies. The slow electron can be expressed to appear with a center-of-mass kinetic energy of $E_{(k,e^-)} = (25 \pm 1.2) \text{ eV}$ and a spread of $\Delta E_{(k,e^-)} = \pm 1.5 \text{ eV}$, whereas the fast electron is found with $E_{(k,e^-)} = (31.5 \pm 1.2) \text{ eV}$ and a similar spread of $\Delta E_{(k,e^-)} = \pm 1.5 \text{ eV}$. In fig. 5.18 the computed spectra display the distributions when an energy beyond the respective energy interval is used in the simulation.

5.5 Discussion

In the previous sections the feasibility of photoelectron spectroscopy measurements under xuv radiation on a fast moving H_3O^+ ion beam has been demonstrated. In combination with the heavy charged fragment detection system a break-up channel resolved investigation of the observed photoelectron and photofragment spectra is possible. By this, the fragmentation was found to proceed from outer valence shell ionized H_3O^{++} into three pathways: A dominant two-body and two three-body break-up channels. In the upcoming paragraph, the observations made for the fragmentation as well as for the electron spectroscopy measurements are combined and discussed regarding their significance for the physics of the photofragmentation process.

5.5.1 Two-body break-up: $\text{H}_2\text{O}^+ + \text{H}^+$

The fragmentation and photoelectron spectroscopy measurements were done in different phases of the experiment. Regarding the electron spectroscopy, the path of the ion beam through the spectrometer was not straight. This affected the orbit of the outgoing H^+ fragments, i.e., it does not allow to deduce the total kinetic energy release from the H^+ break-up products. Hence, the electronic signal and the photofragment spectra cannot be directly correlated on an event-by-event basis. To qualitatively combine the observed kinetic energy spectra of the photoelectrons and photofragments, some pre-considerations have to be made.

As expressed in the energy balance of eq. (2.7), the experimentally accessible spectrum of the photoelectrons is linked to the kinetic energy release spectrum of the photofragments

$$\hbar\omega + E_{(\text{i},\text{H}_3\text{O}^+)} = E_{(\text{k},\text{e}^-)} + E_{\text{KER}} + E_0(\text{H}_2\text{O}^+ + \text{H}^+) + E_{\text{Int.}}(\text{H}_2\text{O}^+) \quad (5.7)$$

where $E_{(\text{i},\text{H}_3\text{O}^+)}$ reflects the initial vibrational energy of the target (indicated by a cyan shaded area in fig. 5.19), see sec. 2.1.3. Eq. 5.7 can be rephrased into

$$E_{\text{KER}} = \underbrace{\hbar\omega - E_{(\text{k},\text{e}^-)} - E_0(\text{H}_2\text{O}^+ + \text{H}^+)}_{E_{\text{KER}}^0} + E_{(\text{i},\text{H}_3\text{O}^+)} - E_{\text{Int.}}(\text{H}_2\text{O}^+.) \quad (5.8)$$

In such a representation, E_{KER}^0 denotes the expected kinetic energy release if neither the target nor the charged water fragment carries vibrational excitation. From eq. (5.8) it is obvious that an excitation of the target or the charged water fragment leads to an increase or decrease of the total kinetic energy release E_{KER} . From the present experimental data neither the internal excitation of the reactant nor that of the products is directly accessible. These quantities are therefore the unknown parameters in the following discussion.

The kinetic energy release (KER) of the photofragments, the photoelectron spectrum as well as the level scheme of the fragmentation of H_3O^{++} into the binary break-up channel $\text{H}_2\text{O}^+ + \text{H}^+$ are shown in fig. 5.19. Moreover, the resulting di-cationic state energy distributions $\hbar\omega - E_{(\text{k},\text{e}^-)}$ are arranged in the energy scheme. For a certain electronic excitation of the charged water molecule, the cyan shaded areas indicate vibrational and rotational excitations.

First the left part of the illustration, referring to the fast electronic signal (indicated by gray shaded area), is discussed. In the previous section it has been shown that the fast electrons appear in the center-of-mass frame with a certain energy spread of about ± 1.5 eV around the mean of $E_{(\text{k},\text{e}^-)} = 31.5$ eV. For a photon energy of 56.7 eV the di-cationic state energy distribution $\hbar\omega - E_{(\text{k},\text{e}^-)}$ thus peaks around 25.2 eV (see. fig. 5.19). The latter energy is used as a reference for the photofragment spectrum. With respect to this energy and the three electronic state energies of the charged water molecule, different values of E_{KER}^0 are calculated according to eq. (5.8) which are listed in the upper row of table 5.1 and indicated by black dashed lines (to the left) in fig. 5.19. In comparison to $\Delta V = V_2(\{R_0\}) - V_1(\{R_0\}) = 26$ eV (c.f. eq. (2.9)) as predicted by [Raf77] for $3a_1$ valence ionization, also listed in table 5.1, the di-cationic state energy of 25.2 eV suggests the fast electrons to stem from the ionization of this orbital.

The photoelectron spectrum, as reconstructed from the measurement, can be reflected onto the E_{KER} spectrum, indicated for the ground state water product on the left side of fig 5.19. It is seen that neglecting $E_{\text{Int.}}(\text{H}_2\text{O}^+)$ and $E_{(i,\text{H}_3\text{O}^+)}$ the observed KER distribution is represented rather well by the reflected photoelectron spectrum, i.e., a small amount (~ 0.3 eV) of $E_{\text{Int.}}(\text{H}_2\text{O}^+)$ would yield perfect agreement. To populate the A^2A_1 state of the water product, significant internal excitation of the parent H_3O^+ is required (~ 1.5 eV). Although this cannot be strictly excluded, such a high target excitation seems to be rather unlikely. Hence, it is concluded that the X^2B_1 electronic level is populated after the dissociation induced by a vacancy in the

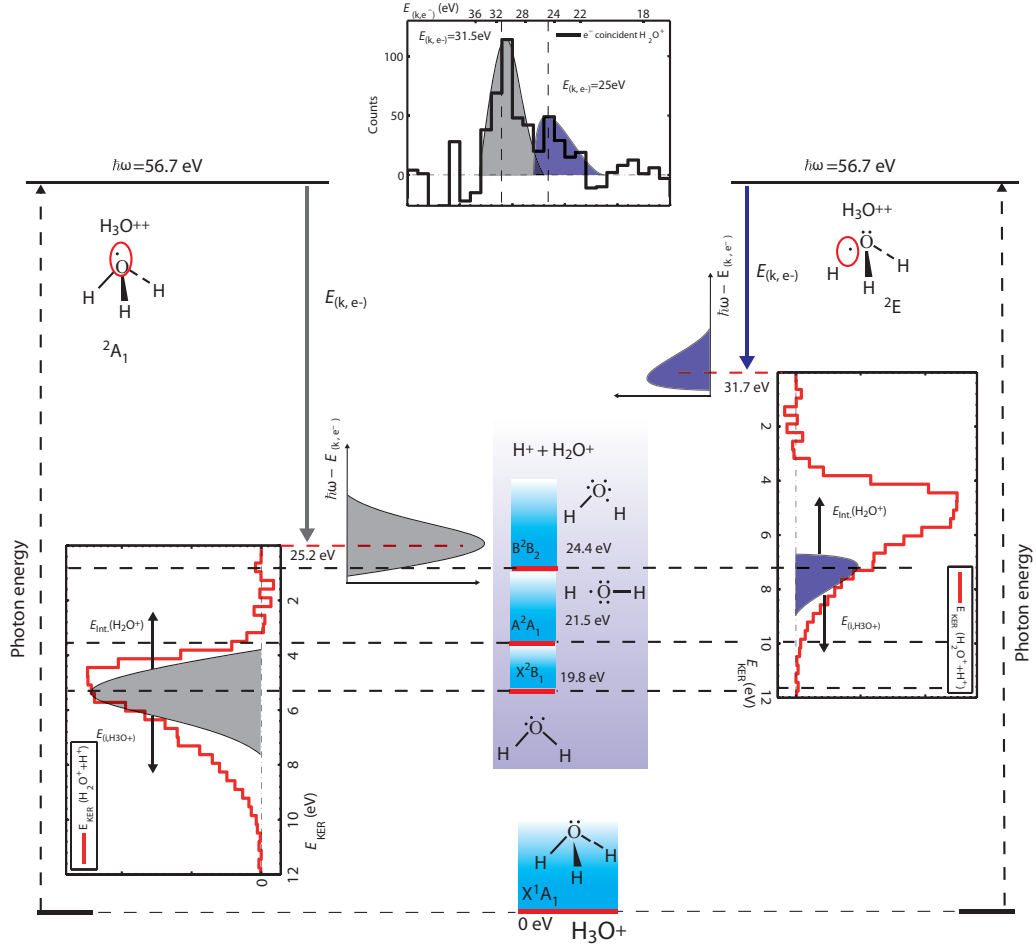


Figure 5.19: Closing illustration of the findings obtained for the two body break-up channel of the dissociative photoionization of H_3O^+ with a photon energy of 56.7 eV, set in contrast to the theoretically expected level scheme of the break-up. The figure on the top expresses the electron time-of-flight distribution, whereas the kinetic energy release distribution is illustrated with two figures to the side.

$3a_1$ orbital.

For the smaller, slow component of the electron line (blue shaded) the comparison is shown on the right hand side of fig. 5.19. The major part of the slow electrons have been identified to appear with a kinetic energy in the center-of-mass frame of $E_{\text{kin},e^-} = 25.0 \text{ eV}$. This yields, for a photon energy of 56.7 eV, a maximum of the di-cationic state energy distribution $\hbar\omega - E_{\text{kin},e^-}$ around 31.7 eV. For this energy of the di-cationic state and the electronic excitation energy of the charged water molecule the different values of E_{KER}^0 are calculated according to eq. (5.8) (listed in the second

$E_{(k,e^-)}$	$\Delta E_{(k,e^-)}$	$\hbar\omega - E_{(k,e^-)}$	ΔV	$E_{\text{KER}}^0(\text{X}^2\text{B}_1)$	$E_{\text{KER}}^0(\text{A}^2\text{A}_1)$	$E_{\text{KER}}^0(\text{B}^2\text{B}_2)$
31.5 ± 1.2	± 1.5	25.2	26.0	5.4	3.7	0.8
25.0 ± 1.2	± 1.5	31.7	31.2	11.9	10.2	7.3

Table 5.1: $E_{(k,e^-)}$: measured kinetic energy at the maximum of the photoelectron spectrum. $\Delta E_{(k,e^-)}$: spread of the photoelectron kinetic energy. E_{KER}^0 : fragment kinetic energy release for different electronic states of the charged water fragment, see fig. 5.19. ΔV denotes the expected orbital binding energy of [Raf77]. All energies are in eV.

row of table 5.1) and expressed by black dashed lines (to the right). Moreover, the di-cationic state energy of 31.7 eV lies close to $\Delta V = 31.2$ as calculated from [Raf77] for $1e$ photoionization. If the origin of the KER scale is again shifted to this value (31.7 eV) (see right part of fig. 5.19), one obtains that the reflected photoelectron spectra in the B^2B_2 state of H_2O^+ gives one of the contributions to the KER spectra not yet explained through the fast electron line. Thus, this part of the spectrum could be expressed by a contribution from the B^2B_2 state with little vibrational fragment energy. The still unexplained KER at around ~ 9 eV could indicate that the target carries internal excitation prior to irradiation.

It may also happen that the lower electronic states (A^2A_1 , X^2B_1) with corresponding very large fragment excitation $E_{\text{Int.}}(\text{H}_2\text{O}^+) \sim 1.5$ eV are populated. Also here, this cannot be decided on the basis of the present data.

Angular distribution of photofragments

The emission angle of the photofragments relative to the laser polarization, which is collinear to the laboratory z -axis, can be computed according to equation 2.23. Under the assumption that the fragmentation into the two-body channel proceeds from $\text{H}_3\text{O}^{++}({}^2\text{A}_1, {}^2\text{E})$ into $\text{H}_2\text{O}^+(\text{X}^2\text{B}_1, \text{B}^2\text{B}_2)$, the angular distribution of the H^+ fragments is determined. The investigation of the emission angle of the H^+ products which are detected in coincidence with charged water on DET 3 is strongly limited by statistics. Thus, to reveal the angular distribution of the events of the two branches of the binary break-up channel, an indirect approach has to be applied. For kinetic energies $E \geq 4$ eV it has been shown in sec. 5.3.4 that, besides some intermixing of the three- and two-body channels for ($4 \leq E \leq 4.9$ eV), mainly the binary channel contributes to the integrated distribution of events on DET 1. One can thus assume that the H^+ events on DET 1, which contribute to the kinetic energy release adjacent to $E_{\text{KER}}^0(\text{X}^2\text{B}_1)$ and $E_{\text{KER}}^0(\text{B}^2\text{B}_2)$ originate from the respective transition of the binary

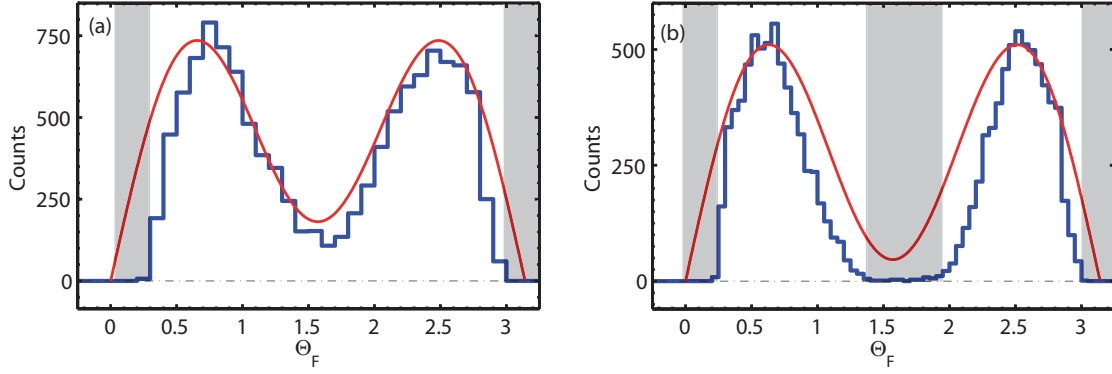


Figure 5.20: Angular distribution of H⁺ fragments on DET 1, $4.0 \leq E \leq 6$ eV (fig. (a)) and to $6 \leq E \leq 8$ eV (fig. (b)). Calculated angular distribution (red line) for $\beta = 1.5$ (fig. (a)) and $\beta = 1.8$ (fig. (b)).

break-up channel. The energy spectrum of events on DET 1 is thus split in intervals around 5 eV (mainly $3a_1$ ionization leading to $\text{H}_2\text{O}^+(\text{X}^2\text{B}_1)$) and 7 eV (mainly $1e$ ionization leading to $\text{H}_2\text{O}^+(\text{B}^2\text{B}_2)$) and the angular distribution of the respective events is computed.

In the left of fig. 5.20, the angular distribution of H⁺ events which contribute to the kinetic energy release of $4 \leq E_{\text{KER}} \leq 6$ eV is shown. The probability to detect a fragment within the emission angle $(\theta_F, \theta_F + d \cos \theta_F)$ relative to the laser polarization is given by equation 2.31. The solid red line represents the computed distribution for an asymmetry parameter $\beta = 1.5$. Since the laser polarization is collinear to the flight direction of the ion beam, the obtained distribution yields a preferred fragment emission parallel and antiparallel to the ion propagation. Due to the central hole in DET 1 fragments which are emitted with an angle $(0 \leq \theta_F \leq 0.3)$ and $(2.9 \leq \theta_F \leq \pi)$ are not detected. This leads to the cut-off of the angular distribution as indicated by the gray shaded areas. As illustrated in sec. 5.3.4, about 20% of the signal events, within the considered energy interval, originate from the three body break-up. Hence the β parameter for that energy interval, can only be stated within boundaries which are governed by the mixing of the three and two body break-up channel. The asymmetry parameter of the transition identified as $\text{H}_3\text{O}^{2+}({}^2\text{A}_1) \rightarrow \text{H}_2\text{O}^+(\text{X}^2\text{B}_1)$ can be derived to be $\beta_1 = 1.5 \pm 0.3$. This value is in good agreement with the asymmetry parameter of $\beta = 2$ for $4.0 \leq E \leq 6.0$ eV found for the dissociative photoionization of H_3O^+ at 90 eV photon energy, as reported in [Ped09].

Fig. 5.20 (b) displays the angular distribution of those H⁺ events which contribute

to the kinetic energy release of $6 \leq E_{\text{KER}} \leq 8 \text{ eV}$. The gray shaded area around ($1.4 \leq \theta_{\text{F}} \leq 2$), indicates a preferred emission perpendicularly to the ion flight direction. Since for these events the major part of the kinetic energy release is stored in the transverse motion, the diameter of the detector is too small and the fragments escape from detection.

The obvious asymmetry around $\pi/2$ can be explained by the fact that emission angles in the center-of-mass frame of ($\theta_{\text{F}} \leq \pi/2$) represent dissociation processes in forward ion flight direction. The longitudinal momentum of these fragments is larger than for the backward emitted particles $\theta_{\text{F}} \geq \pi/2$. Thus, the ratio of transversal to longitudinal velocity, which defines the radial coordinate on the detector, is smaller. Hence a forward-emitted particle with the same transversal velocity as a backwards-emitted one can still reach the detector, while the others miss the detector.

Due to the geometrical limitations of the first detector, the asymmetry parameter can be stated only roughly. The onset as well as the offset of the distribution allow to exclude an isotropic ($\beta = 0$), as well as a perpendicular emission ($\beta = -1$). The computed angular distribution, as it is depicted by the red line in fig. 5.20 (b), is determined for $\beta = 1.8$. The asymmetry parameter of the transition identified as $\text{H}_3\text{O}^{++}({}^2\text{E}) \rightarrow \text{H}_2\text{O}^+(\text{B}^2\text{B}_1)$ can thus be formulated to be $\beta_2 \in [1...2]$.

5.5.2 Three-body break-up: $\text{OH} + \text{H}^+ + \text{H}^+$

Besides the binary break-up channel, a significant three-body break-up pathway $\text{OH} + \text{H}^+ + \text{H}^+$ has been identified. The observed electronic signal (see fig. 5.15) indicates this pathway to be only accompanied by the slower electrons. As shown in the previous section, this suggests the three-body break-up pathway to be initiated by a vacancy in the $1e$ orbital. In fig. 5.21, the level scheme, the photoelectron and the KER spectrum of the photofragments are depicted. Additionally, the energy distribution of the di-cationic state $\hbar\omega - E_{(\text{k},\text{e}^-)}$, with a maximum around 31.7 eV and an energy spread of about $\pm 1.5 \text{ eV}$ as deduced from the simulation (see sec. 5.4.6) is embedded in the level scheme. The photofragment spectrum is again arranged with respect to that maximum and the expected E_{KER}^0 for the ground and first excited state of the hydroxyl radical OH (listed in table 5.2) are indicated by black dashed lines.

A projection of the photoelectron distribution into the electronic ground state

$E_{(k,e^-)}$	$\Delta E_{(k,e^-)}$	$\hbar\omega - E_{(k,e^-)}$	ΔV	$E_{\text{KER}}^0(X^2\Pi)$	$E_{\text{KER}}^0(A^2\Sigma^+)$
25.0 ± 1.2	± 1.5	31.7	31.2	5.8	1.7

Table 5.2: $E_{(k,e^-)}$: measured kinetic energy at the maximum of the photoelectron spectrum. $\Delta E_{(k,e^-)}$: spread of the photoelectron kinetic energy. E_{KER}^0 : kinetic energy release for different electronic states of the hydroxyl radical OH, see fig. 5.19 and ΔV denotes the expected orbital binding energy of [Raf77]. All energies are in eV.

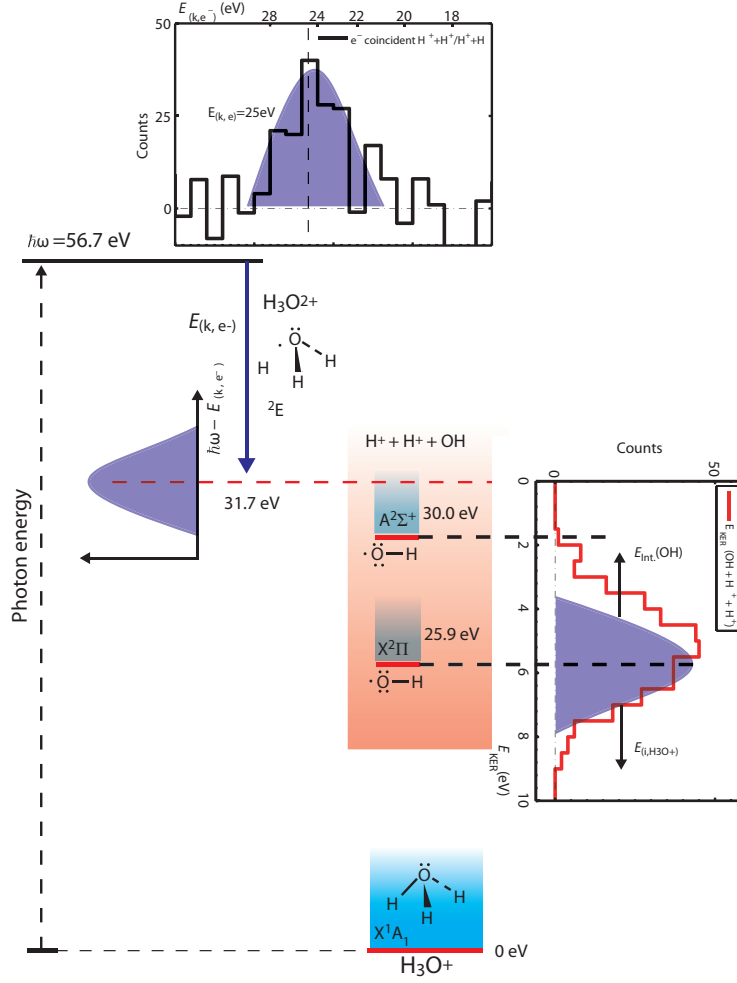


Figure 5.21: Closing illustration of the findings obtained for the three break-up channel of the dissociative photoionization of H_3O^+ at 56.7 eV photon energy, set in contrast to the theoretically expected level scheme of the break-up. The figure on the top expresses the electron time of flight distribution, whereas the kinetic energy release distribution is illustrated with the left figure.

$X^2\Pi$ of the hydroxyl radical OH, neglecting $E_{\text{Int.}}(\text{OH})$ and $E_{(i,\text{H}_3\text{O}^+)}$, represents the KER distribution towards the upper end. The deviation at the lower kinetic energy release indicates that some part of the dissociation energy is transformed into

internal excitation of hydroxyl radical, i.e., $E_{\text{Int.}}(\text{OH}) \sim 0.8 \text{ eV}$ would yield a good representation of the observed KER spectrum.

Energetically, it is also possible that the three-body break-up populates the first excited state of the hydroxyl radical ($\text{OH}(\text{A}^2\Sigma^+)$). For this to happen, the overall available kinetic energy is reduced by the excitation energy of 4 eV from the ground to first excited state. The neutral detector is still fully sensitive for these events but the light charged fragments might escape from detection.

The pathway producing OH^+ fragments is strongly suppressed in contrast to the other channels, which allows only for a tentative characterization of the break-up. The obtained electron spectra as well as the kinematical analysis of the break-up products provide no indication that inner valence ionization might trigger that dissociation pathway.

Cross section

Finally, the cross section of the neutral OH containing three-body break-up channel is presented. Within three beam times, the dissociative photoionization of H_3O^+ was investigated at $E_\gamma = 35.5 \text{ eV}$, 56.7 eV and $E_\gamma = 90 \text{ eV}$ photon energy. The minimal photon energy to open the channel is given by the ionization threshold of the 1e-orbital of $E_{1e} = 31.2 \text{ eV}$. The obtained cross section, shown in fig. 5.22, exhibits its maximum value for a photon energy of 35.5 eV. The biggest uncertainty on the

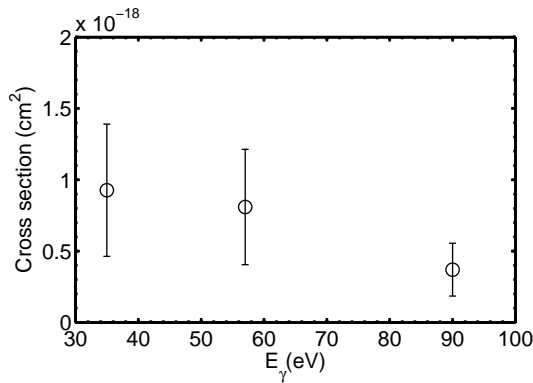


Figure 5.22: Absolute cross section, obtained for the dissociative photofragmentation of H_3O^+ proceeding into $\text{OH} + \text{H}^+ + \text{H}^+$ at $E_\gamma = 35.5 \text{ eV}$, 56.7 eV and 90 eV photon energy.

cross section stems from the variation in the number of photons, delivered to the interaction region.

Chapter 6

Free electron laser experiments on $\text{H}^+(\text{H}_2\text{O})_2$

The first dissociative photoionization studies on the Zundel ion H_5O_2^+ at 90 eV photon energy, performed at TIFP, revealed a dominant binary break-up pathway $\text{H}_5\text{O}_2^{++} \rightarrow \text{H}_3\text{O}^+ + \text{H}_2\text{O}^+$ [Lam10, Wol10]. Due to limitations in the detection systems (c.f. sec.3.1.2) the heavy ionic break-up products H_nO^+ $n = (1...3)$ were only partially accessible during that investigation. Therefore, the heavy charged fragment analyzer in combination with the saddle-point spectrometer was employed to observe all outgoing reaction products including the photoelectrons to fully observe the fragmentation pattern.

The remarkable research interest in small water clusters is motivated by the fact that these systems are considered as the intermediate stage between isolated molecules in the gas phase and molecules in solution or bulk media [Mue04]. Protonated water H_3O^+ , the Eigen ion, and the protonated water cluster $(\text{H}_2\text{O})_2\text{H}^+$, the Zundel ion, are of key importance for the water cluster formation since they have been identified as the fundamental units in bulk water and isolated water clusters [Mar99, Nie08]. In the Earth's atmosphere, charged water clusters are for instance found to participate in droplet and cloud formation [Ste01]. Besides their relevance in atmospheric and biochemical processes they can also be considered as model systems for understanding the mobility of a free charge in the aqueous surrounding. Hence, numerous experimental and theoretical works have been devoted to advance the understanding of these systems [Asm03, Mue04, Mue05, Ven08].

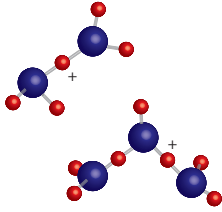


Figure 6.1: Theoretical minimum-energy structures when two and three water molecules cluster around a proton according to [Hea05].

6.1 Properties of $\text{H}^+(\text{H}_2\text{O})_2$

The geometry of a water cluster is governed by the ambition of the neutral water molecule to attach via hydrogen bonds to the proton and in addition that during the cluster formation the water angle \angle_{HOH} is kept nearly preserved. Consequently, the Zundel ion is composed of two water molecules loosely bound by a central proton which is equidistantly spaced between the opposing oxygen atoms [Hea05], see fig.6.1. The bond angle between $\text{O} - \text{H}^+ - \text{O}$ is found to be about $\angle_{\text{OH}^+\text{O}} = 176^\circ$ [Xie94], i.e., it deviates only a little from linearity. In its ground state the system is of ${}^1\text{XA}_1(\text{C}_{2v})$ symmetry and the equilibrium distance between one OH-bond of $\text{O} - \text{H}^+ - \text{O}$ is 1.117 \AA [Yeh89].

In comparison to the hydronium ion the number of valence orbitals of the dimer is increased. The outer valence orbitals can be subdivided in the ones which participate in the binding and the ones which are basically unaffected by the bond. Starting out with the latter, the lone pair electrons of each of the oxygen atoms which do not interact with the bonding constitute the outer valence orbital with the lowest binding energy of $\sim 20\text{eV}$ [Ven12]. Since the water molecules to each side are equivalent this level is twofold degenerate at the equilibrium configuration.

The outer valence electrons shared among the non-interacting OH-bonds exhibit a binding energy of $\sim 26.6\text{eV}$. These levels are also twofold degenerate.

The lone pair electrons of the oxygen facing towards the central proton can interact with each other, giving rise to two levels with distinct ionization energies of $\sim 21.9\text{eV}$ and $\sim 27.4\text{eV}$, respectively.

The inner valence orbitals are occupied by the oxygen 2s electrons, and are predicted by different calculations at either $\sim 40\text{eV}$ [Mue04] or $\sim 49\text{eV}$ [Ven12]. Inner and outer valence ionization levels are indicated in fig.6.2.

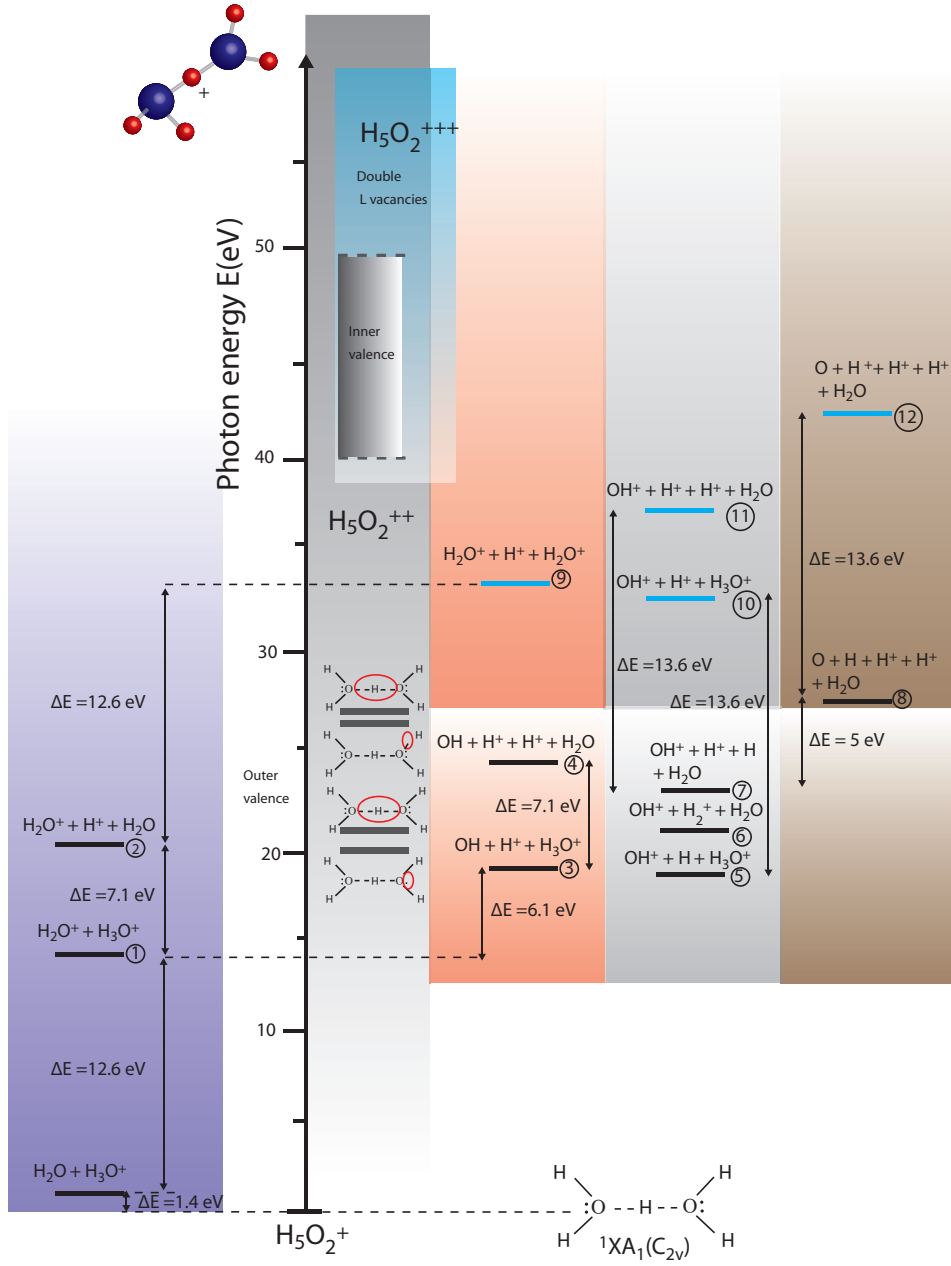


Figure 6.2: Inner and outer valence ionization energies of H_5O_2^+ , adapted from [Mue04, Ven12], and level diagram for fragmentation into possible break-up channels. Proton affinities and ionization energies are taken from [Nist].

6.2 Photoionization pathways

Similar to relation 5.2 the ionization process of H_5O_2^+ can be written in the form

$$\text{H}_5\text{O}_2^+(\{v\}, J) + \gamma \rightarrow \text{H}_5\text{O}_2^{++} + e^-. \quad (6.1)$$

Here, the energy levels that are reached correspond to the orbital energies discussed in the previous section. Theoretical studies regarding the shape of the potential surfaces of $\text{H}_5\text{O}_2^{++}$ around the approximate energies marked in gray shaded column of fig. 6.2 have been performed recently [Ven12]. Via the potential energy surface of the dicationic system fragmentation into a number of energetically allowed, lower final channels may occur as indicated in fig. 6.2.

6.2.1 Expected fragmentation pathways

As reported in [Sto06], the gas phase dissociation energy of H_5O_2^+ into H_3O^+ and H_2O is $\sim 1.4\text{ eV}$, see lower corner of left column in fig. 6.2. At first the break-up pathways which can be initiated by either outer or inner valence vacancies are discussed (final levels indicated by black lines). A break-up process into the binary channel $\text{H}_2\text{O}^+ + \text{H}_3\text{O}^+$ yields the maximum possible kinetic energy release of $\sim 7\text{ eV}$ from the lowest $\text{H}_5\text{O}_2^{++}$ orbital. This process is illustrated in the leftmost column. Starting out from that pathway, the sequential separation of the H^+ reduces the overall available kinetic energy by the proton affinity of the respective fragment (c.f. sec. 5.2). Thus, the KER for further fragmentation of H_3O^+ leading to the three body channel $\text{H}_2\text{O}^+ + \text{H}^+ + \text{H}_2\text{O}$ ch.(3), is reduced by 7.1 eV . In case of a continuing break-up of H_2O^+ , resulting in $\text{OH} + \text{H}^+ + \text{H}_2\text{O}$ ch.(4) the KER is further reduced by $\sim 6.1\text{ eV}$.

If the charge remains with the OH^+ fragment the available kinetic energy release of chs.(5,7) is elevated by the difference of the ionization energy of OH and H of 0.6 eV (see section 5.2).

Inner valence ionization requires a photon energy $E_\gamma \geq 40\text{ eV}$ [Ven12, Mue04] which may open an autoionization pathway, most likely ICD [Mue05], as indicated with the cyan shaded area in the level scheme of fig. 6.2. In terms of fragmentation pattern the experimental signature of such a process is a sharing of the three excess charges among the different break-up products. The levels which arise from autoionization are indicated cyan colored lines. In comparison to pathway (2), the available kinetic energy release of ch.(9) is reduced by the ionization energy of H_2O ($\sim 12.6\text{ eV}$) and in contrast to pathway (5),(7) and (8) ch.(10),(11) and (12) is elevated by the ionization energy of H ($\sim 13\text{ eV}$).

6.3 Fragmentation

At a FLASH photon energy of 56.7 eV the first phase of the experiment was devoted to fragmentation studies with an average FEL energy of 30 μJ per pulse, whereas the second part was dedicated to electron spectroscopy measurements at a reduced FEL energy of 2 μJ per pulse. The thereby obtained results are presented in section 6.4.

6.3.1 Experimental parameters

TIFF was operated with similar conditions as given in sec. 5.3. The final dc current of 10 nA in the interaction region corresponds to a linear particle density of $n_l = I/(v_l q_l) = 4.20 \cdot 10^3 \text{ mm}^{-1}$. The electrostatic mirror-unit (c.f. sec. 3.1.3) was set such that singly charged ionic fragments with a kinetic energy of 1.9–2.2 keV (H_nO^+ ($n=0\dots3$)) could reach DET 3.

6.3.2 Fragment assignment

In fig. 6.3 the observed signal time-of-flight distributions on the three fragment detectors for the dissociative photoionization of $\text{H}^+(\text{H}_2\text{O})_2$ at $E_\gamma = 56.7 \text{ eV}$ photon energy are shown. Two different measurements were taken: One with a unbiased interaction region $U_B = +0 \text{ V}$ (black curve) and one with $U_B = +200 \text{ V}$ (red curve).

The dashed black lines indicate the expected arrival times of the respective fragment species for the measurement with biased interaction region. The smooth distribution around 1000–1400 ns (red curve) is found to be H^+ induced, whereas the sharp feature around 1800 ns originates mainly from heavy charged fragments H_nO^+ ($n = 0\dots2$) which reach DET 1 (black dashed line in lower left of fig. 6.3 indicates expected arrival time of H_2O^+). Here the number of hydrogen atoms n , cannot directly be resolved. The shoulder around 1900 ns can be assigned to stem from neutral fragments, most notably neutral H, whereas no H_2^+ induced signal is observable. The signal on the second detector stems from neutral fragments, which can be H_nO ($n=0\dots2$). In comparison to the dissociative photoionization of the hydronium ion a third fragment species H_3O^+ is additionally observable on DET 3. The mirror was also operated in a mode where singly charged ionic fragments with a kinetic energy of 3.8 – 4.1 keV H_nO_2^+ ($n = 0\dots4$) are transmitted to DET 3. Since that measurement did not reveal the existence of another heavy charged reaction product

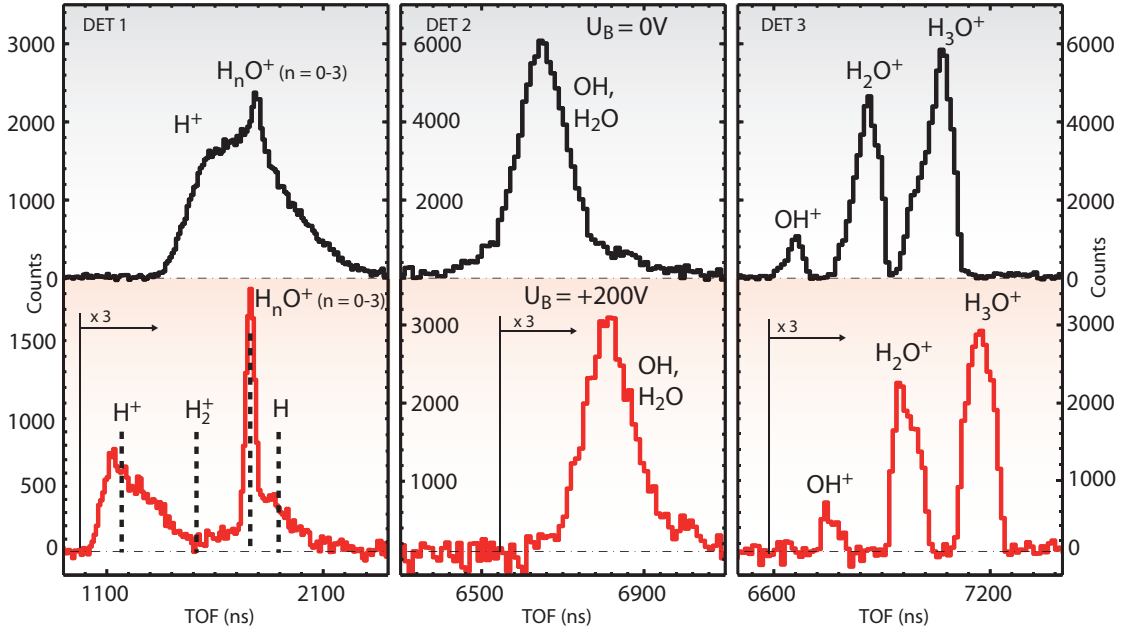


Figure 6.3: Time of flight distribution on DET 1-3 after background correction. The upper gray shaded spectra display the $U_B = 0$ V the lower red shaded ones show signal distribution of the $U_B = +200$ V measurement. The major contribution to the signal on DET 1 stems from H^+ and H_2O^+ . The signal on the neutral detector is mainly composed of OH. On the third detector OH^+ , H_2O^+ and H_3O^+ are detected.

the above identified break-up products comprise the hole set of observed fragment species for the dissociative photoionization of H_5O_2^+ at $E_\gamma = 56.7$ eV.

6.3.3 Assignment of fragmentation pathways

In the following paragraph the fragmentation pathways are identified. For this, four means are employed: (1) The coincident occurrence between certain fragment species, (2) charge and (3) mass conservation (c.f. section 2.1.2) and (4) the kinematical completeness of the break-up, i.e. the conservation of the longitudinal momenta. In fig. 6.4, the histograms to the side and on top represent the time-of-flight distribution of the different fragment detectors as they were acquired in the zero bias measurement. The upper two-dimensional scatter plots (a, b) display the coincidence maps for hits on DET 1 or DET 2 correlated with hits on DET 3. The lower two dimensional scatter plot (c) displays the self-correlated signal of the heavy charged fragment detector DET 3. At first, the correlations of each fragment species observed with DET 3 are pointed out and discussed in more detail in the following subsections.

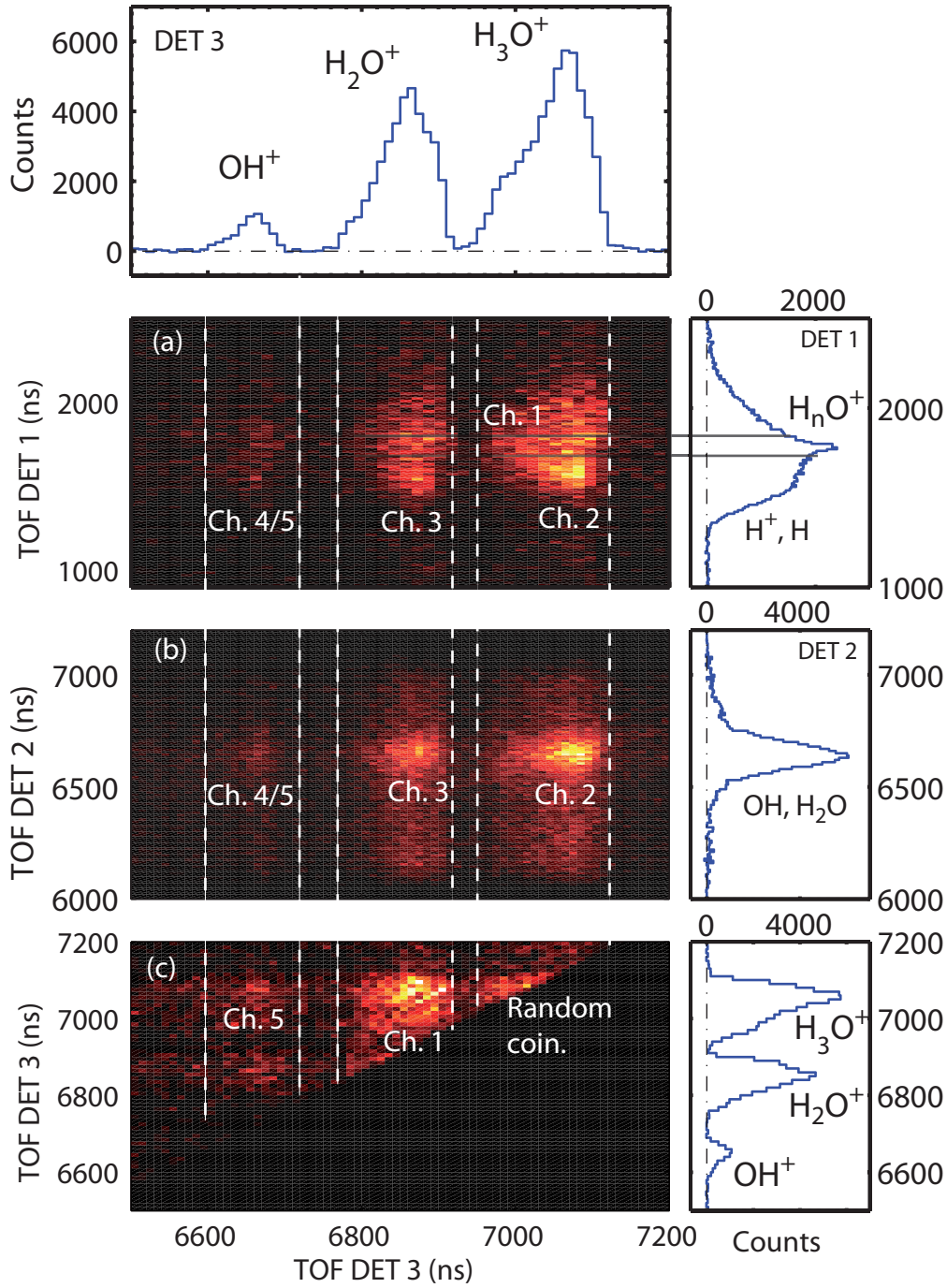


Figure 6.4: The upper two-dimensional scatter plots, (a, b) display the coincidence maps for the correlation of hits on DET 1 or DET 2 referenced to DET 3. The lower two dimensional scatter plot expresses the self-correlated signal of DET 3. The histograms on the top and to the side, show the time of flight distribution of the signal events on the respective detector. Channels contributing to specific ranges in the coincidence maps are indicated by Ch.1-Ch.5.

Regarding the two stronger peaks on DET 3, both the H_2O^+ and H_3O^+ break-up products are found correlated with H^+ and H_nO^+ on DET 1 as well as with neutral hits on DET 2. In addition, the self-correlated signal of DET 3 (panel c) shows that H_2O^+ is strongly coincident with H_3O^+ .

The smaller peak of OH^+ fragments occurs in coincidence with H^+ and neutral H on DET 1 (obtained for the measurement with biased interaction zone) as well with neutral fragments on DET 2 (c.f. fig. 6.4 (b)). The self-correlated signal of DET 3 yields that OH^+ is also accompanied by H_3O^+ and very weakly by H_2O^+ (c.f. fig. 6.4 (c)). In the following, the fragmentation channels are discussed in detail.

H_3O^+ producing pathways

Identification of $\text{H}_3\text{O}^+ + \text{H}_2\text{O}^+$ (ch.(1)): The self-correlated signal of DET 3 reveals a strong coincidence between H_3O^+ and H_2O^+ , which marks the contribution of the binary break-up pathway $\text{H}_3\text{O}^+ + \text{H}_2\text{O}^+$ (ch. 1) on DET 3.

As discussed in sec. 6.2.1, the largest amount of kinetic energy is expected to be released in the two-body break-up process. For the observed heavy ionic fragments H_nO^+ to reach DET 1 at least 5 eV of kinetic energy is necessary. Indeed the heavy charged break-up products H_nO^+ on DET 1 are accompanied by H_3O^+ and also but less strongly by H_2O^+ on DET 3 (Interval indicated in the upper two dimensional histogram (a) by the gray horizontal lines). The number of hydrogen atoms of the parent molecule is $n_{\text{H}} = 5$ and of oxygen atoms $n_{\text{O}} = 2$. Thus, the correlation of H_nO^+ (DET 1) with H_3O^+ and mass conservation of the break-up process yields the number of hydrogen atoms which is associated with the heavy fragments on DET 1 to be $n = 2$, i.e., mainly charged water fragments H_2O^+ emerging from the binary break-up channel impinge on DET 1.

Identification of $\text{H}_3\text{O}^+ + \text{H}^+ + \text{OH}$ (ch.(2)): By applying a coincidence cut between the hits on DET 1 obtained in the measurement with biased interaction zone and H_3O^+ it has been found that H_3O^+ is also strongly correlated with H^+ fragments on the first detector. The atomic content of the parent beam and the observed coincidence restricts the remaining fragment to $n'_{\text{H}} = 1$ and $n'_{\text{O}} = 1$. Since the two excess charges are already shared among the observed coincident ionic fragments the missing product has to be neutral OH. Further fragmentation of neutral OH would lead to a significant neutral H induced signal on DET 1, which is not observed. The corresponding fragments, H^+ , OH and H_3O^+ are kinematically corre-

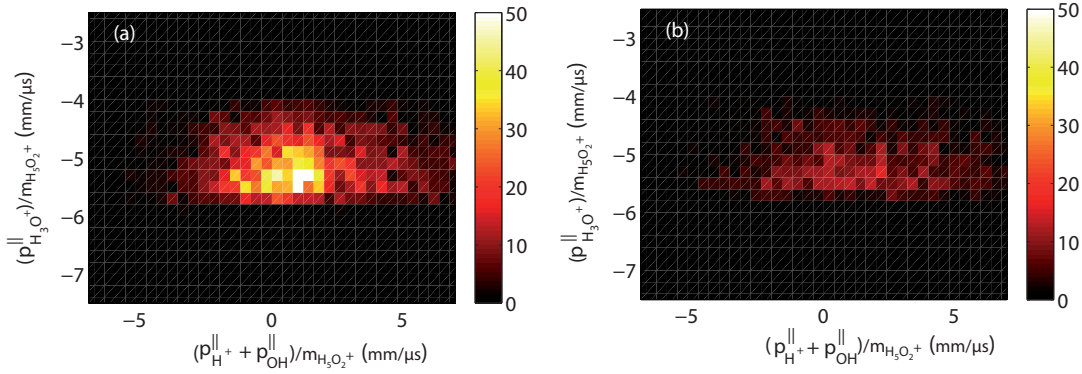


Figure 6.5: (a): Kinematical correlation between H^+ hits DET 1 and neutral hits on DET 2 under the restriction these hits have to be accompanied by one H_3O^+ fragment on DET 3. (b): Kinematics of randomly correlated hits.

lated. In fig. 6.5 (a) the sum of the center-of-mass longitudinal momenta of H^+ and OH ($p_{\text{H}^+}^{\parallel} + p_{\text{OH}}^{\parallel}$)/ $m_{\text{H}_5\text{O}_2^+}$, normalized to the mass of the parent molecule, is plotted against the longitudinal momentum ($p_{\text{H}_3\text{O}^+}^{\parallel}$)/ $m_{\text{H}_5\text{O}_2^+}$. To model the dispersion of the mirror an effective drift length is used to determine the longitudinal momentum of H_3O^+ , which makes these events to appear around $p_{\parallel, \text{H}_3\text{O}^+} = -5 \text{ mm}/\mu\text{s}$. In such a representation and under ideal conditions, transversal and longitudinal momentum are as such conserved and the kinematics of the break-up would force the correlated events to lie on a straight line with negative slope (c.f. section 3.1.3), since $p_{\text{H}^+}^{\parallel} + p_{\text{OH}}^{\parallel} = -p_{\text{H}_3\text{O}^+}^{\parallel}$. Indeed the events show a correlation with each other, which deviates from the expected ideal case. When a charged particle propagates through the mirror longitudinal momentum is translated into transversal momentum and vice-versa (c.f. section 3.1.3). Thus, the kinematical correlation between real events appears blurred. Fig. 6.5(b) displays the momentum distribution of randomly correlated events. Since no correlation is obvious a dominant three-body channel $\text{H}_3\text{O}^+ + \text{H}^+ + \text{OH}$ ch. (2) can be identified.

H_2O^+ producing pathways

The charged water molecule has already been identified to be partially produced in the binary break up channel.

Identification of $\text{H}_2\text{O}^+ + \text{H}^+ + \text{H}_2\text{O}$ (ch.(3)): In analogy the correlation between the H_2O^+ induced signal of DET 3 and the one of DET 1 can be analyzed. By means of coincidence analysis the coincident fragments on DET 1 can be identified to be H^+ . Thus the number of hydrogen and oxygen atoms of the remaining fragment can

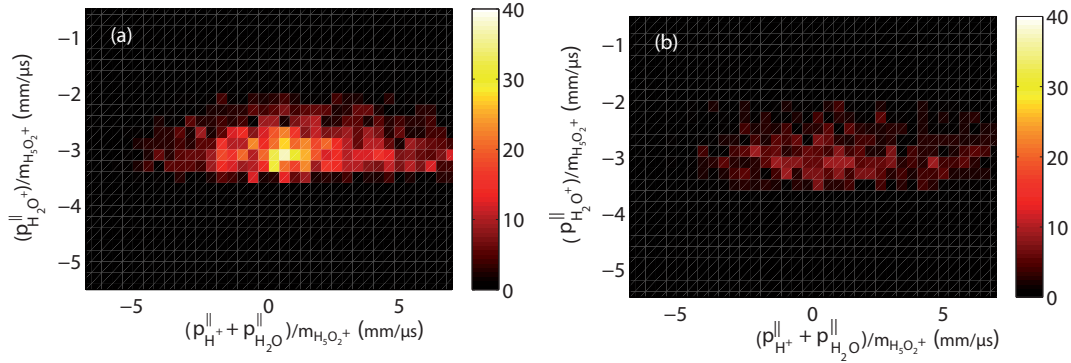


Figure 6.6: (a) Kinematical correlation between H^+ hits on DET 1 and neutral hits on DET 2 under the restriction that these hits have to be accompanied by one H_2O^+ fragment on DET 3. (b) Kinematics of randomly correlated hits.

be determined to be $n'_\text{H} = 2$ and $n'_\text{O} = 1$ and the neutral break-up product can be identified to be H_2O . In fig. 6.6 (a) the sum of the longitudinal momentum of H^+ and H_2O $(p_{\text{H}^+}^{\parallel} + p_{\text{H}_2\text{O}}^{\parallel})/m_{\text{H}_5\text{O}_2^+}$ is plotted against $p_{\text{H}_2\text{O}^+}^{\parallel}/m_{\text{H}_5\text{O}_2^+}$. Given that in contrast to the randomly correlated events at the right of fig. 6.6, a clearly enhanced intensity around $(p_{\parallel, \text{H}^+} + p_{\parallel, \text{H}_2\text{O}}, p_{\parallel, \text{H}_2\text{O}^+}) = (0 \text{ mm}/\mu\text{s}, 3 \text{ mm}/\mu\text{s})$ for real coincidences is observed the three body break channel $\text{H}_2\text{O}^+ + \text{H}^+ + \text{H}_2\text{O}^+$ (3) can be identified.

OH^+ producing pathways

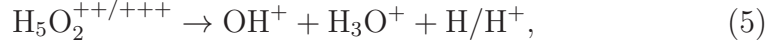
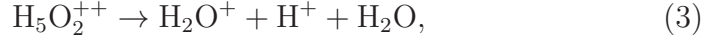
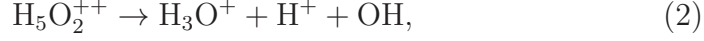
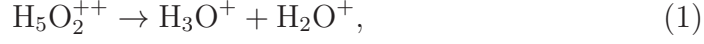
As stated above, for this fragment species two significant coincidences are observable.

Identification of $\text{OH}^+ + \text{H}^+ + \text{H} + \text{H}_2\text{O}$ (ch.(4)): First the correlation with neutral H and H^+ on DET 1 is considered (obtained with the biased measurement), which restricts atomic content of the residual neutral fragment on DET 2 to $n'_\text{H} = 2$ and $n'_\text{O} = 1$. Since no correlation with charged water is observed, the remaining neutral fragment can be assigned to H_2O , which is formed in a four-body break-up process $\text{OH}^+ + \text{H}^+ + \text{H} + \text{H}_2\text{O}$, channel (4).

Identification of $\text{OH}^+ + \text{H}_3\text{O}^+ + \text{H}/\text{H}^+$ (ch.(5)): The second, rather weak, OH^+ producing pathway is indicated by the correlation between OH^+ and H_3O^+ (lower two-dimensional histogram). Due to the limited statistics of the OH^+ -induced signal a triple coincidence between a OH^+ , H_3O^+ hit on DET 3 and the signal on DET 1 (for a biased interaction zone) cannot be performed. Thus it cannot be finally decided if the missing fragment is H^+ or neutral H. By this, another three-body break-up channel $\text{OH}^+ + \text{H}_3\text{O}^+ + \text{H}/\text{H}^+$ where OH^+ is produced can be identified.

From the present experimental results the following dominant break-up channels

can be formulated:



Branching of fragmentation pathways

Since the heavy charged fragments OH^+ , H_2O^+ and H_3O^+ contribute to more than one reaction-channel, the branching of the pathways can only be determined by considering the respective coincident signal.

The observed fragmentation channels express that each of the prominent break-up pathways (2-4) is accompanied by one heavy neutral fragment, which is exclusively detected by DET 2. This circumstance can be used to disentangle the contribution of the respective three-body channel to the OH^+ , H_2O^+ and H_3O^+ induced signal of DET 3. Additionally, the transmission of the mirror T_M at the setting used during the fragmentation measurement can be obtained. The integrated signal of DET 2, $N_{(\text{neut.}, \text{D2})}$ is the sum over all neutral fragments stemming from the respective break-up channel:

$$N_{(\text{neut.}, \text{D2})} = N_{(\text{OH}, \text{ch}(2), \text{D2})} + N_{(\text{H}_2\text{O}, \text{ch}(3), \text{D2})} + N_{(\text{H}_2\text{O}, \text{ch}(4), \text{D2})}. \quad (6.2)$$

The notation is chosen such that $N_{(\text{OH}, \text{ch}(2), \text{D2})}$, $N_{(\text{H}_2\text{O}, \text{ch}(3), \text{D2})}$ and $N_{(\text{H}_2\text{O}, \text{ch}(4), \text{D2})}$ reflect the unknown number of *neutral* fragments OH and H_2O on the second detector, which are produced in ch. (2), (3), (4).

A coincidence requirement between the signal on DET 2 and the one of DET 3 yields the number of coincident events of each ionic fragment species observed with DET 3: $N_{(F, \text{coin.}, \text{D2}, \text{D3})}$, $F \in \text{OH}^+, \text{H}_2\text{O}^+, \text{H}_3\text{O}^+$. The events of a certain fragment species, for instance H_3O^+ on DET 3, which is expected to be detected in coincidence with the signal DET 2 is given by $N_{\text{H}_3\text{O}^+, \text{coin.}, \text{D2}, \text{D3}} = \epsilon_2 \epsilon_3 T_M N_{\text{OH}, \text{ch}(2), \text{D2}}$, (c.f. eq. (5.6)), where $N_{\text{OH}, \text{ch}(2), \text{D2}}$ represents the unknown number of OH signal-hits on DET 2 of ch. (2) (see sec. 3.5.1). Thus, the number of neutral events which are produced in the

respective break-up channel can be derived from

$$\begin{aligned} N_{(\text{OH}, \text{ch}(2), \text{D2})} &= \mathbf{N}_{(\text{H}_3\text{O}^+, \text{coin.}, \text{D2}, \text{D3})} / (\epsilon_2 \epsilon_3 T_M), \\ N_{(\text{H}_2\text{O}, \text{ch}(3), \text{D2})} &= \mathbf{N}_{(\text{H}_2\text{O}^+, \text{coin.}, \text{D2}, \text{D3})} / \epsilon_2 \epsilon_3 T_M, \\ N_{(\text{H}_2\text{O}, \text{ch}(4), \text{D2})} &= \mathbf{N}_{(\text{OH}^+, \text{coin.}, \text{D2}, \text{D3})} / (\epsilon_2 \epsilon_3 T_M), \end{aligned} \quad (6.3)$$

where the detection efficiencies of DET 2 and DET 3 are again given by $\epsilon_{(2,3)}$.

The total number of each heavy charged species on DET 3 can be expressed as the sum of the contributions of the different channels:

$$\begin{aligned} \mathbf{N}_{(\text{H}_3\text{O}^+, \text{D3})} &= N_{(\text{H}_3\text{O}^+, \text{ch}(1), \text{D3})} + N_{(\text{H}_3\text{O}^+, \text{ch}(2), \text{D3})} + N_{(\text{H}_3\text{O}^+, \text{ch}(5), \text{D3})}, \\ \mathbf{N}_{(\text{H}_2\text{O}^+, \text{D3})} &= N_{(\text{H}_2\text{O}^+, \text{ch}(1), \text{D3})} + N_{(\text{H}_2\text{O}^+, \text{ch}(3), \text{D3})}, \\ \mathbf{N}_{(\text{OH}^+, \text{D3})} &= N_{(\text{OH}^+, \text{ch}(4), \text{D3})} + N_{(\text{OH}^+, \text{ch}(5), \text{D3})}. \end{aligned} \quad (6.4)$$

To investigate the self-correlated signal on DET 3 a certain fragment species like H_3O^+ is taken as a reference and the coincident OH^+ and H_2O^+ hits are extracted. According to that, the investigation of the self-correlated signal on DET 3 yields the number of coincident events $\mathbf{N}_{(\text{F}, \text{coin.}, \text{D3}, \text{D3})}$ ($F \in \text{OH}^+, \text{H}_2\text{O}^+, \text{H}_3\text{O}^+$).

Thus from the self-correlated signal the contribution of ch. (1) to the H_3O^+ as well as to the H_2O^+ signal and additionally the contribution of ch. (5) to the OH^+ signal can be derived

$$\begin{aligned} N_{(\text{H}_3\text{O}^+, \text{ch}(1), \text{D3})} &= \mathbf{N}_{(\text{H}_2\text{O}^+, \text{coin.}, \text{D3}, \text{D3})} / (\epsilon_3^2 T_M^2), \\ N_{(\text{H}_2\text{O}^+, \text{ch}(1), \text{D3})} &= \mathbf{N}_{(\text{H}_3\text{O}^+, \text{coin.}, \text{D3}, \text{D3})} / (\epsilon_3^2 T_M^2), \\ N_{(\text{OH}^+, \text{ch}(5), \text{D3})} &= \mathbf{N}_{(\text{H}_3\text{O}^+, \text{coin.}, \text{D3}, \text{D3})} / (\epsilon_3^2 T_M^2). \end{aligned} \quad (6.5)$$

The experimentally accessible quantities are the total number of neutral hits $\mathbf{N}_{(\text{neut.}, \text{D2})}$ on DET 2 as well as the heavy charged fragment induced hits $\mathbf{N}_{(\text{F}, \text{D3})}$ on DET 3 with ($F \in \text{OH}^+, \text{H}_2\text{O}^+, \text{H}_3\text{O}^+$). The correlation between DET 2 and DET 3 yields $\mathbf{N}_{(\text{F}, \text{coin.}, \text{D2}, \text{D3})}$ and the self-correlation of DET 3 provides $\mathbf{N}_{(\text{F}, \text{coin.}, \text{D3}, \text{D3})}$ with ($F \in \text{OH}^+, \text{H}_2\text{O}^+, \text{H}_3\text{O}^+$). Thus by combining the relations (6.3, 6.2, 6.4, and 6.5) the transmission of the mirror and the relative branching of the channels can be determined. The transmission of the mirror is found to be $T_M = 0.6 \pm 0.1$.

The relative contribution of each channel to the integrated signal can be determined as follows: About $N_{\text{OH}, \text{ch}(2), \text{D2}} / \mathbf{N}_{(\text{neut.}, \text{D2})} = 0.60 \pm 0.1$ of the neutral fragments orig-

inate from ch. (2), another $N_{\text{H}_2\text{O}, \text{ch}(2), \text{D2}}/\mathbf{N}_{(\text{neut.}, \text{D2})} = 0.30 \pm 0.1$ of the neutral events are produced in ch. (3), and the remaining $N_{\text{H}_2\text{O}, \text{ch}(2), \text{D2}}/\mathbf{N}_{(\text{neut.}, \text{D2})} = 0.10 \pm 0.1$ can be attributed to ch. (4). With these findings the contribution of ch. (2) to the observed H_3O^+ signal and the one of ch. (3) to the H_2O^+ signal can be computed. This yields that $N_{(\text{H}_3\text{O}^+, \text{ch}(1), \text{D3})}/\mathbf{N}_{(\text{H}_2\text{O}^+, \text{D3})} = 0.40 \pm 0.1$ of the H_3O^+ and $N_{(\text{H}_2\text{O}^+, \text{ch}(1), \text{D3})}/\mathbf{N}_{(\text{H}_2\text{O}^+, \text{D3})} = 0.60 \pm 0.1$ of the H_2O^+ events are produced in the binary break-up channel. By this, the relative branching of the channels can be derived to be

$$\begin{aligned} f_{(\text{ch.}(1))} &= 0.30 \pm 0.17, \\ f_{(\text{ch.}(2))} &= 0.45 \pm 0.25, \\ f_{(\text{ch.}(3))} &= 0.20 \pm 0.12, \\ f_{(\text{ch.}(4))} &= 0.03 \pm 0.03, \\ f_{(\text{ch.}(5))} &= 0.02 \pm 0.02, \end{aligned}$$

which identifies the binary (1) and the H_3O^+ containing three-body break-up channel. (2) as the prominent pathways. The error bars on the stated relative branching are mainly due to the uncertainty of the detection efficiency of the respective detector. A further discussion of these findings is given in sec. 6.5.

Absolute cross section

Fig. 6.7 shows that the second detector is fully sensitive to all neutral fragments. Therefore, the absolute cross section of the neutral fragment producing fragmentation pathways can be derived. According to eq. (2.30), the absolute cross section can be derived, where the sum extends over all signal cycles. The multi-channel plate efficiency of DET 2 is given by $\epsilon_2 = 0.5 \pm 0.1$. The transmission of the PG 2 photon beam line is $T_{\text{PG 2}} = 0.4 \pm 0.1$. The overlap factor can be determined to be $F = (5.5 \pm 1.0) \text{ cm}^{-1}$. With the average number of photons per pulse N_γ and the linear density n_{I} , the cross section can be calculated to be $\sigma_{\text{neut.}} = (3.6 \pm 1.2) 10^{-18} \text{ cm}^2$ (c.f. section 5.3.4), which yields in combination with the relative strength of ch. (2) a total cross section for this pathway of $\sigma_{\text{ch.}(2)} = (2.4 \pm 1.3) \cdot 10^{-18} \text{ cm}^2$ and for all events of $\sigma = (5.3 \pm 2.8) \cdot 10^{-18} \text{ cm}^2$.

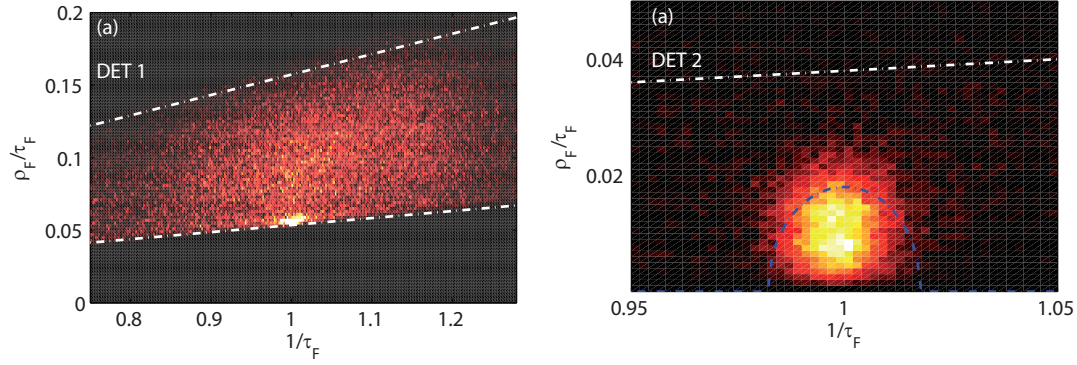


Figure 6.7: (a) Normalized momentum sphere of all events on DET 1, after background correction. (b) Normalized momentum sphere of all events on DET 2, after background correction.

6.3.4 Photofragment momentum imaging

The normalized center of mass momenta (see sec. 2.2.1) of all hits on DET 1 is shown in fig. 6.7(a). The elevated intensity confined in the sphere $\sqrt{(1/\tau - 1)^2 + (\rho/\tau)^2} \leq 0.06$ can be attributed to stem from heavy charged fragments, which impinge on the inner edge of the central hole of the first detector. The diffuse radial distribution of the light charged fragments, most notably H^+ and neutral H indicates that these events originate from break-up processes, where more than two break-up products are released. The momentum sphere of all events on the second detector is depicted in fig. 6.7(b), which identifies them to be well-confined within a sphere of $\sqrt{(1/\tau - 1)^2 + (\rho/\tau)^2} \leq 0.02$ diameter. The dashed white line marks again the detection limit which is imposed by the first detector (c.f. fig. 3.7).

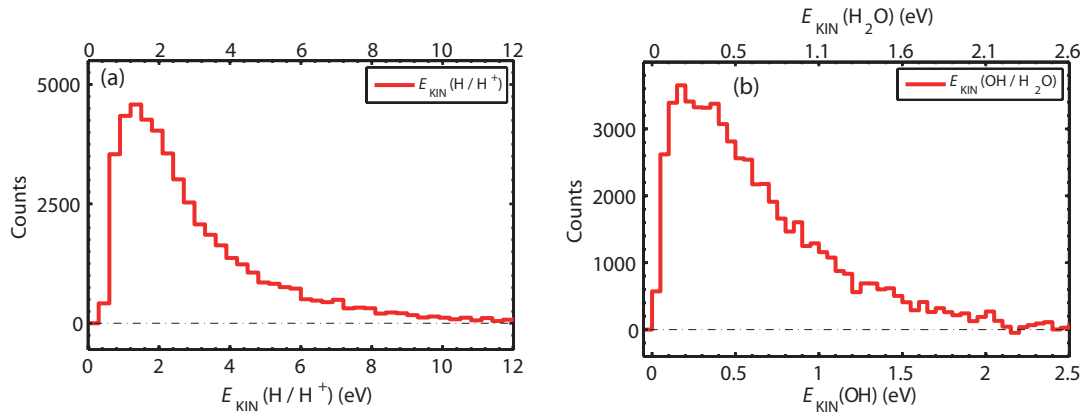


Figure 6.8: Kinetic energy spectrum of H^+ and H fragments on DET 1 (a) and neutral $\text{OH}/\text{H}_2\text{O}$ fragments on DET 2 (b).

The kinetic energy spectra of the events on the two imaging detectors are shown in fig. 6.8. The events are separated for heavy fragments ($\sqrt{(1/\tau - 1)^2 + (\rho/\tau)^2} \leq 0.06$) and light break-up products, H^+ and neutral H , ($\sqrt{(1/\tau - 1)^2 + (\rho/\tau)^2} \geq 0.06$). For the latter, the kinetic energy is computed according $E = p^2/2m_{H^+}$ and displayed in fig. 6.8. The energy distribution exhibits a clear maximum around 1.8 eV and extends up to 10 eV.

The investigation of the relative strength of the different break-up pathways revealed ch. (2, 3) as the major neutral fragment producing ones. Since the signal on DET 2 cannot be distinguished for OH or H_2O the neutral break-up products' kinetic energy is computed according to $E = p^2/2m_F$ with $F \in OH, H_2O$. The lower abscissae of fig. 6.8(b) displays the kinetic energy of the OH fragments, whereas the upper x-axis states the kinetic of neutral water. On both scales the distribution exhibits a maximum around 0.25 eV and extends up to 2 eV.

Two-body break-up

The coincidence analysis revealed the heavy charged fragments on DET 1 to be mainly H_2O^+ with a minor contribution of H_3O^+ . Their center of mass kinetic energy is determined via $E = p_F^2/2m_F$ with $F \in H_2O^+, H_3O^+$. Similarly as for the neutral signal on DET 2 the lower abscissae of fig. 6.9 displays the kinetic energy of H_2O^+ fragments, whereas the upper abscissae states the one of H_3O^+ break-up products. As it was discussed in sec. 6.3.3 the heavy ionic fragments impinging on the first detector can be attributed to stem from the binary break-up ch. (1). Under the assumption that mainly charged water is observed on DET 1 the kinetic energy release for the binary break-up channel can be computed according

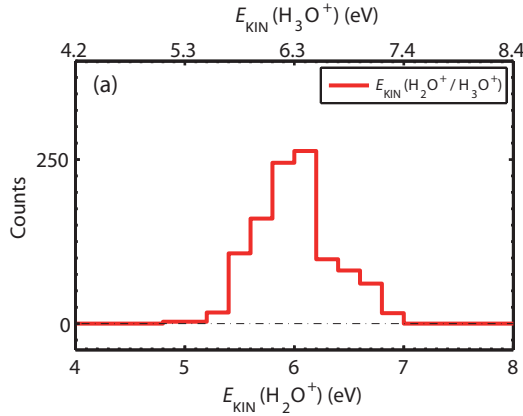


Figure 6.9: Kinetic energy spectrum of heavy ionic fragments on DET 1, which can be attributed to the binary break-up channel: $H_3O^+ + H_2O^+$.

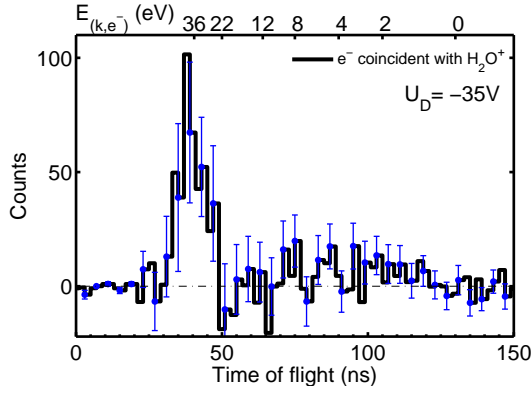


Figure 6.10: Electronic signal coincident with H_2O^+ , obtained for a retarding potential of $U_D = -35 \text{ V}$.

$E_{\text{KER}(\text{H}_2\text{O}^+ + \text{H}_3\text{O}^+)} = p_{\text{H}_2\text{O}^+}^2 (1/2m_{\text{H}_2\text{O}^+} + 1/2m_{\text{H}_3\text{O}^+})$, which allows for the conclusion that up to 12 eV of kinetic energy is released in the two-body break-up channel.

6.4 Photoelectron spectroscopy

In the previous section, the prominent fragmentation pathways have been identified. In analogy to the investigation of the hydronium ion the photoelectron spectroscopy measurements were done in a different phase of the experiment, with conditions, comparable to the ones of the electron spectroscopy measurement of H_3O^+ . The dc-current was again 10 nA. The limited signal-to-noise ratio of the electronic signal again restricts the investigation to the coincident signal. Unfortunately the path of the ion beam through the spectrometer was not straight, which influenced the orbit of the H^+ fragments. Therefore it is not possible to apply a coincident cut on the H^+ induced signal on DET 1. Thus only the electronic signal coincident with the heavy charged fragment species H_3O^+ and H_2O^+ can be explored.

6.4.1 Coincidence with H_2O^+

The electronic signal as it was acquired in coincidence with H_2O^+ is shown in fig. 6.10. The error bars reflect again the statistical uncertainty of the respective signal. In contrast to the rather narrow line, as observed for the ionization of the hydronium ion (see sec. 5.4.4), the distribution, shown in fig. 6.10, exhibits a width of about 20 ns. As the assignment of the break-up pathways in section 6.3.3 revealed, the charged water fragment is produced in the two-body (ch. (1)), as well as in the three-body break-up pathway (ch. (3)). Thus the observed coincident electronic signal comprises contributions of both channels.

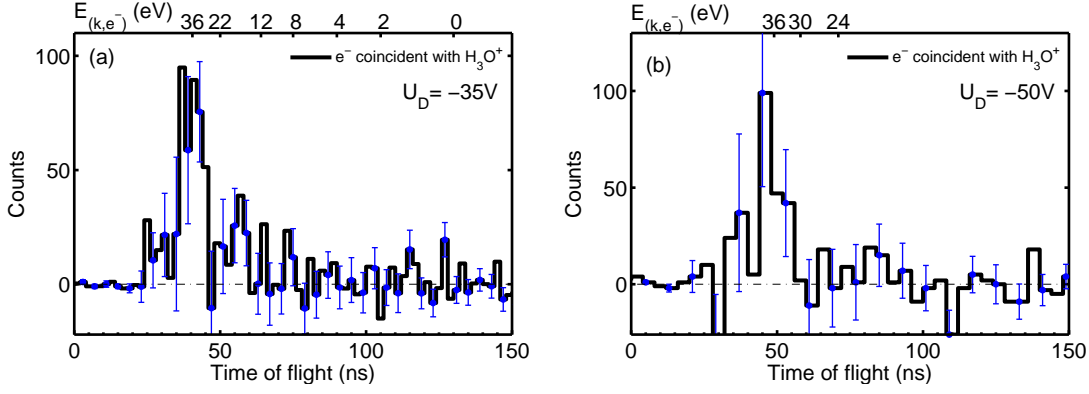


Figure 6.11: Electronic signal coincident with H_3O^+ , obtained for a retarding potential of $U_D = -35$ V (a) and $U_D = -50$ V (b).

The characteristic broadening effects, as they are imposed by the finite width of the interaction region and the time resolution of the data acquisition system can be assumed to be independent of the considered molecular system. The only effect depending on the target is the kinematical broadening. Since the velocity of the dimer scales with $\sqrt{m_{\text{H}_3\text{O}^+}/m_{\text{H}_5\text{O}_2^+}}$ relative to the one of the monomer, the kinematics of the ionization process on the moved target can be addressed to impose a width of $\Delta E = \pm 1$ eV on the electronic signal (c.f. sec. 2.3).

6.4.2 Coincidence with H_3O^+

The coincidence cut on the second heavy ionic fragment species H_3O yields the electron time-of-flight spectra as shown in fig. 6.11. The distribution as it is obtained for $U_D = -35$ V (fig. 6.11 (a)), has a stronger maximum around 35 ns and in addition possibly a small feature occurs in the vicinity of 55 ns. The hydronium ion has been assigned to be produced in the binary (ch. (1)) as well as in the three body break-up pathways (chs. (2, 5)). Hence the coincident electronic signal represents the integrated contribution of two strong channels. A further retardation with $U_D = -50$ V shifts the dominant peak to 50 ns but does not yield a further separation of the feature. The less energetic electrons which contributed to the side peak around 55 ns ($U_D = -35$ V) cannot appear for $U_D = -50$ V since such a retardation rejects all electrons with a kinetic energy smaller than $E_{(k,e-)} \leq 24$ eV.

In the previous paragraph the electronic signal found in coincidence with H_2O^+ exhibits only one dominant component, which has been assigned to stem from ch. (1) and (3), respectively. This suggests that the possible signature of less energetic

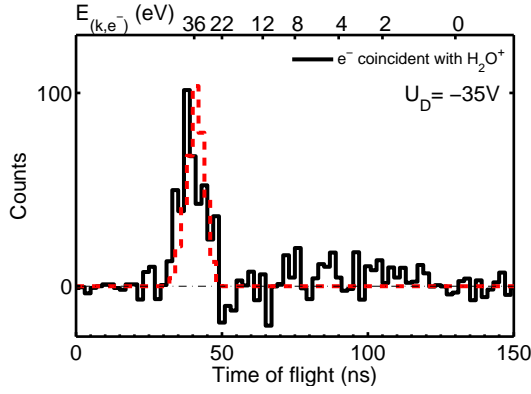


Figure 6.12: Red dashed line, computed time-of-flight distribution for $(E_{(k,e^-)}, \beta) = ((30...38 \text{ eV}), 1)$ and a retardation with $U_D = -35 \text{ V}$.

electrons is either associated with ch. (2) or ch. (5). Additionally, the rather broad time range covered by the dominant component of the electronic signal gives rise to the assumption that different molecular orbitals may have been ionized.

6.4.3 Monte Carlo Simulation

In analogy to the approach used to represent the photoelectron spectra obtained for the photoionization of the hydronium ion, the photoionization process for a fixed number of randomly oriented $\text{H}^+(\text{H}_2\text{O})_2$ molecules is computed according eq. (2.31). The photoelectron spectroscopy measurements were done with two different retardation modes ($U_D = -35 \text{ V}, -50 \text{ V}$). In the upcoming paragraphs the electronic signal as observed either in coincidence with H_2O^+ or H_3O^+ are compared to the simulated spectra.

Coincidence with H_2O^+

The computed and measured electron time-of-flight distributions are depicted in fig. 6.12. The simulation was done with a set of electrons with a kinetic energy randomly taken from the interval $E_{(k,e^-)} = (30...38 \text{ eV})$ with an asymmetry parameter $\beta = 1$. The chosen energy range reflects the electron signal as it is obtained for the H_2O^+ -containing fragmentation pathways. As mentioned in section 5.4 the time-of-flight to the electron detectors is rather short for these kinds of electron energies. Thus, the asymmetry parameter can only be stated within boundaries. From the results of the Monte Carlo simulation it can be concluded, that the integrated electronic signal of the fragmentation ch. (1) or (2), can be described via a set of electrons with $E_{(k,e^-)} = (30...38 \text{ eV})$, which corresponds for a photon energy of 56.7 eV

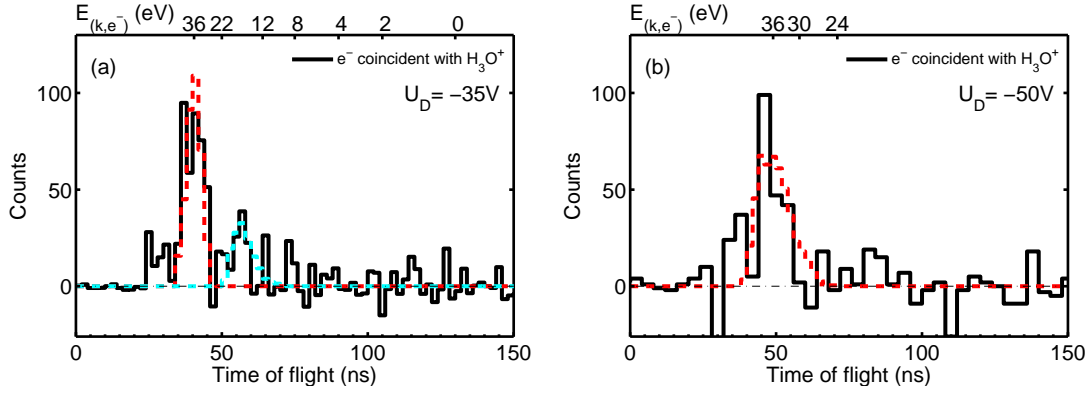


Figure 6.13: (a): Retardation $U_D = -35$ V (b): $U_D = -50$ V. Red dashed line computed time of flight distribution for $(E_{(k,e^-)}, \beta_1) = ((32...38 \text{ eV}), 1)$ and cyan dashed $(E_{(k,e^-)}, \beta_2) = ((17...19 \text{ eV}), 1)$.

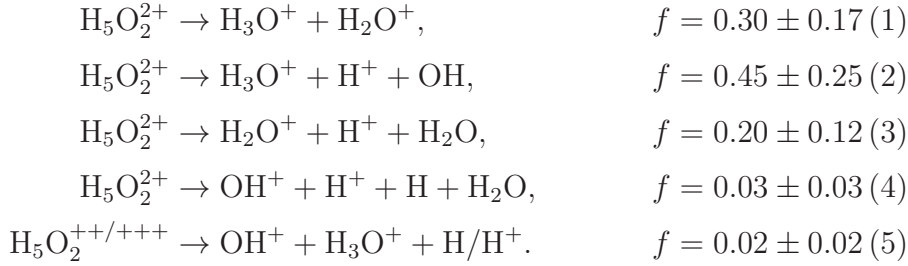
to binding energies of $E_B \approx (19...27 \text{ eV})$.

Coincidence with H_3O^+

The time-of-flight distribution under the coincidence requirement that an electron has to be accompanied by a H_3O^+ fragment is illustrated in fig. 6.13. The hydronium ion is split off in the break-up pathways (1), (2) and (5). The major peak around 35 ns is expressed with the Monte Carlo simulation by a set of electrons with a kinetic energy randomly taken from the interval $E_{(k,e^-)} = (32...38 \text{ eV})$ and an asymmetry parameter $\beta_1 = 1$. The feature around 55 ns can be represented with a kinetic energy $E_{(k,e^-)} = (17...18 \text{ eV})$ and an asymmetry parameter $\beta_2 = 1$. With a photon energy of 56.7 eV a binding energy of $E_{B,1} \approx (19...25 \text{ eV})$ and $E_{B,2} \approx (38...40 \text{ eV})$ for the fast and slow electron family can be computed.

6.5 Discussion

The dissociative photoionization of $\text{H}^+(\text{H}_2\text{O})_2$ in the xuv wavelength regime has been investigated both regarding photoelectron- and photofragment- spectroscopy where the following prominent break-up pathways (indicated in fig. 6.14) have been identified,



The majority of light break-up products H and H^+ , formed in chs.(2-5) are found to be released with an average kinetic energy of about 2 eV, whereas the heavy neutral fragments OH and H_2O chs.(2-3) carry about 0.3 eV of kinetic energy. In comparison to the expected fragmentation pathways, as depicted in fig 6.2 the observed kinetic energies of the break-up products allow to conclude that the major part of reactions proceeds outer valence ionization. The fragments, formed in the binary break-up channel $\text{H}_2\text{O}^+ + \text{H}_3\text{O}^+$ are ejected with a total kinetic energy release of up to $E_{\text{KER}} = 12$ eV. With respect to the fragment production it has to be emphasized that the dominant chs. (1) and (2), which carry three-quarter of the overall intensity, contain the hydronium ion H_3O^+ as a stable structural unit, i.e., the photolysis of the dimer ion seems to favor the production of the hydronium ion. In addition, the formation of the hydroxyl radical OH (ch.(2)) appears enhanced in comparison to neutral water production (ch.(3)). Larger neutral water clusters have recently been subjected to photoionization studies in the vuv wavelength regime [Bar09, Bel07]. In the latter, it has been found that the relaxation of the larger mono-cationic systems is mediated by a proton transfer followed by the emission of an OH molecule. The tendency of an elevated production of the hydroxyl radical ch.(2) might point to a similar relaxation mechanism, i.e., the transfer of electronical excitation of the charged water molecule into its vibrational motion may lead to its dissociation, where a further H^+ is split off. For the neutral fragment producing break-up channels an absolute cross section of $\sigma_{\text{neut.}} = (3.6 \pm 1.2) 10^{-18} \text{ cm}^2$ has been found.

By means of coincidence analysis the electronic signal was linked with certain break-up channels. The electron energies and corresponding binding energies are

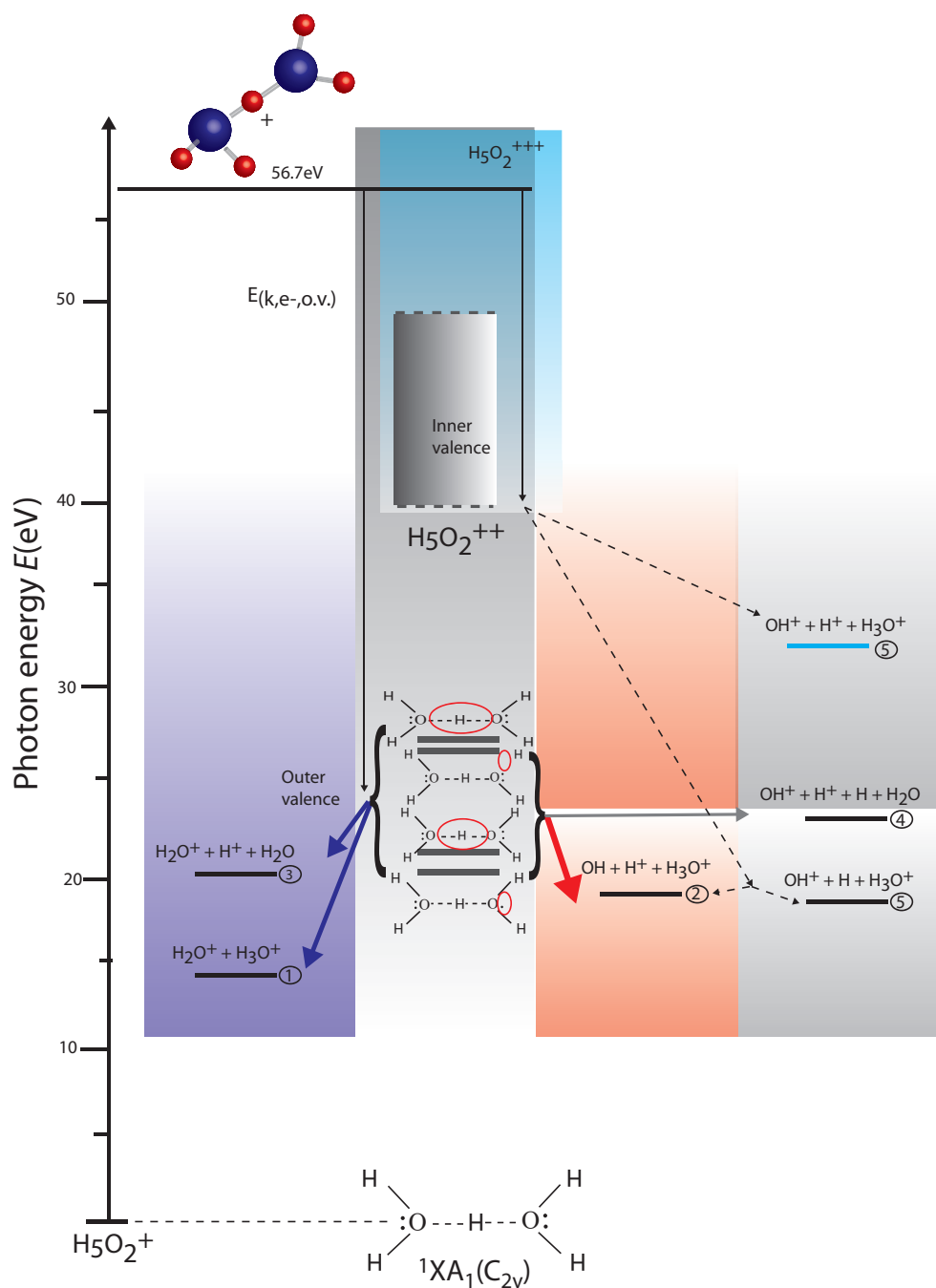


Figure 6.14: Obtained fragmentation pathways of dissociative photoionization of H_5O_2^+ at $E_\gamma = 56.7 \text{ eV}$. The black arrows indicate the measured kinetic energy of the photoelectrons. The full arrows mark the identified break-up pathways.

given in sec.6.4.3. The correlation with the heavy ionic break-up product H_2O^+ yields a binding energy of the photoelectrons associated with that fragment species of $E_B \approx (19...27 \text{ eV})$. Since the charged water molecule is formed in the first and third

break-up pathway the observed coincident electronic signal represents the integrated contribution of both channels (c.f. left column of fig. 6.14).

The electronic signal accompanied by H_3O^+ reflects the contributions of ch. (1),(2) and (5). Here, a dominant part was found with a binding energy of $E_B = (19...25 \text{ eV})$ and a smaller fraction bound by $E_B = (38...40 \text{ eV})$. A direct correlation between the OH^+ fragment and the electronic signal was hampered by the limited statistic.

From these electron signals one can conclude that the major fraction of the electrons which are accompanied by one of the two heavy ionic fragment species H_2O^+ ($E_B = (19...25 \text{ eV})$) and H_3O^+ ($E_B = (19...25 \text{ eV})$) are ionized from the outer valence orbital of the system. With a CASSCF approach the outer valence orbital energies have recently been calculated [Ven12] to range from 20 up to 27 eV. In comparison to the ionization potential of $\sim 20.6 \text{ eV}$ reported in [Taf10] and the theoretical predictions [Ven12] the measured binding energies are in good agreement, albeit for the electrons which are detected in coincidence with H_2O^+ a binding energy of up to $\sim 27 \text{ eV}$ is found as compared to electrons which are accompanied by H_3O^+ with a somewhat smaller range up to $\sim 25 \text{ eV}$ binding energy only. This would in particular suggest that the H_3O^+ containing channels are not initiated by a vacancy of the highest outer valence orbital (c.f. fig. 6.14). Here, an electron spectroscopy measurement with a higher resolution could clarify which orbitals are ionized in the initial step.

As illustrated, the electronic signal found coincident with H_3O^+ showed signs of a second electron species with binding energies in the range of $E_B = (38...40 \text{ eV})$ which would match the theoretically expected inner valence orbital energies as given in [Mue04] of about $\sim 40 \text{ eV}$ (c.f. fig. 6.14). As a final channel, this electron family also allows the triply ionized state $\text{OH}^+ + \text{H}^+ + \text{H}_3\text{O}^+$, which could possibly be reached by autoionization to $\text{H}_5\text{O}_2^{+++}$ states. This inner valence contribution, however, results at most in a small fraction of the total signal at $E_\gamma = 56.7 \text{ eV}$.

Summarizing, from the present stage of investigation these findings provide for the first time a detailed representation of the photon induced fragmentation pattern of the mass selected fast moving H_5O_2^+ ion correlated to the respective photoelectron spectra. For future experiments a detailed investigation of the photoelectron spectra with a higher resolution of the spectrometer in parallel to the fragmentation studies could in particular be instructive to clarify whether of the outer valence orbitals are ionized and if autoionization process might open.

Chapter 7

Summary and outlook

In the context of this thesis the reaction channel specific photoelectron spectroscopy of photon induced dissociation processes on fast moving molecular ion-beams in the xuv-wavelength regime has been established. Here, the major aspect was to study the photolysis of the hydronium ion H_3O^+ as well as the dimer ion H_5O_2^+ and to observe the incident photoelectron in coincidence with all outgoing reaction products.

Regarding the photoelectron spectroscopy, a conceptually new saddle-point spectrometer has been employed. In a first measurement to quantify the kinematics of the photoionization process on a moved target, the photodetachment process of a fast beam of O^- anions with a pulsed Nd:YAG laser at 266 nm wavelength, using a magnetic bottle spectrometer has been investigated. There, the branching of the ground $\text{O}(^3\text{P})$ and first excited state $\text{O}(^1\text{D})$ population was found to be $F_{\text{P}}/F_{\text{D}} = 0.32 \pm 0.06$ with asymmetry parameters of $\beta_{\text{P}} = 0.00 \pm 0.10$ and $\beta_{\text{D}} = -0.90 \pm 0.10$, respectively. Based on these findings the novel saddle-point electron spectrometer has been commissioned while studying the photodetachment dynamics on a beam of O^- anions at 532 nm at the X-Ring fast ion-beam infrastructure in Aarhus Denmark. Numerical trajectory simulations were employed to characterize the observed photoelectron spectra and demonstrated that they can be used to obtain the electron energies.

In addition, to perform a break-up channel resolved analysis of the observed photoelectron spectra a new heavy charged fragment analyzing system was developed. The system acts as an energy dispersive filter to separate heavy ionic fragments with one a.u. mass difference. In combination with the saddle-point spectrometer both devices were implemented in the TIFF (**T**rapped **I**on **F**ragmentation at an **F**EL) fast ion beam infrastructure at the free electron laser FLASH at DESY in Ham-

burg, which allows for a coincident detection of the incident photoelectrons with all break-up products.

As a first target, employing the improved detection system the dissociative photoionization of the hydronium ion H_3O^+ at 56.7 eV photon energy has been investigated. By this, three reaction pathways were identified: a dominant binary $\text{H}_2\text{O}^+ + \text{H}^+$ ($f = 0.65 \pm 0.35$) and two three-body break-up channels $\text{OH} + 2\text{H}^+$ ($f = 0.28 \pm 0.15$) and $\text{OH}^+ + \text{H}^+ + \text{H}$ ($f = 0.08 \pm 0.08$). The observed photoelectron spectra revealed each of them to be initiated by outer valence vacancies. A further differentiation, yielding a more channel-specific analysis of the coincident electronic signal, showed that the binary break-up channel is mainly triggered by the ionization of the $3a_1$ orbital, whereas the three-body break-up pathways proceed through ionization of the $1e_1$ orbital of the hydronium ion. Moreover, the correlation of the photofragment as well as photoelectron spectra suggested the charged water molecule to be mainly produced in its electronic ground $\text{H}_2\text{O}^+(\text{X}^2\text{B}_1) + \text{H}^+$ and second excited state $\text{H}_2\text{O}^+(\text{B}^2\text{B}_2) + \text{H}^+$. In [Ped09] a transition into the $\text{H}_2\text{O}^+(\text{A}^2\text{A}_1)$ state has been proposed. There, the fragment spectrum was correlated to the di-cationic state energy of 26 eV for $3a_1$ ionization of H_3O^+ as given in [Raf77]. In the present work, the measured di-cationic state energy of 25.2 eV appears decreased by ~ 0.8 eV in comparison to the theoretically expected value, leading to the different interpretation of the final electronic state of the charged water fragment. On the other hand, in case of the fragmentation into the three-body channel the hydroxyl radical OH is mainly formed in its electronic ground state $\text{OH}(\text{X}^2\Pi) + 2\text{H}^+$. The absolute cross section for all photon induced reactions was found to be $\sigma = (1.2 \pm 0.8) \cdot 10^{-18} \text{ cm}^2$ and for the neutral OH containing channel $\sigma_{\text{OH}+2\text{H}^+} = (0.3 \pm 0.2) \cdot 10^{-18} \text{ cm}^2$.

Moreover, the photolysis of the dimer ion H_5O_2^+ at 56.7 eV photon energy, showed that besides the manifold of energetically allowed fragmentation channels five prominent break-up pathways are populated:

$\text{H}_3\text{O}^+ + \text{H}_2\text{O}^+$ ($f = 0.30 \pm 0.17$) (1), $\text{H}_3\text{O}^+ + \text{H}^+ + \text{OH}$ ($f = 0.45 \pm 0.25$) (2), $\text{H}_2\text{O}^+ + \text{H}^+ + \text{H}_2\text{O}$ ($f = 0.20 \pm 0.12$) (3), $\text{OH}^+ + \text{H}^+ + \text{H} + \text{H}_2\text{O}$ ($f = 0.03 \pm 0.03$) (4) and $\text{OH}^+ + \text{H}_3\text{O}^+ + \text{H}^+$ ($f = 0.02 \pm 0.02$) (5).

For about three quarter of the observed reaction processes the hydronium ion is split off as stable structural unit, whereas for the heavy neutral fragment containing channels the production of the hydroxyl radical OH is preferred compared to neutral water formation. Here, it appears as an interesting question whether in the initial step of a sequential process mainly the binary channel is populated, and a transfer

of internal excitation of either the hydronium or charged water molecule into vibrational motion leads to their dissociation. Such a mechanism would give rise to the enhanced formation of heavy neutral break-up products as observed in channels (2) and (3).

The acquired electron signal showed that the majority of dissociation processes is initiated by outer valence ionization, with binding energies as expected from recent theoretical calculations [Ven12]. Absolute cross sections of the neutral OH producing break-up channel of $\sigma_{\text{ch.(2)}} = (2.4 \pm 1.3) \cdot 10^{-18} \text{ cm}^2$ and for all events of $\sigma = (5.3 \pm 2.8) \cdot 10^{-18} \text{ cm}^2$ have been found, which underlines that in comparison to the dissociative photoionization of H_3O^+ the production of neutral OH fragment is enhanced by a factor of about eight in case of the dimer ion.

Since up to now little is known about the potential energy surfaces arising from valence vacancies of the hydronium as well as the dimer ion, these detailed findings set an interesting model case for theory to further advance their approaches for understanding the response of such small water clusters to ionizing radiation in the vuv to soft x-ray spectral region. With respect to future experiments, the improved detection system in combination with the fast ion beam method provides a versatile instrument to probe the photoexcitation and dissociative photoionization mechanism of a large number of molecular systems. Slight modifications of the setup, such as a better vacuum to further reduce the photon induced noise on the electron detectors and an improved alignment of the setup, would allow for a direct correlation of the photoelectron and photofragment spectrum. Measurements with vibrationally cooled H_3O^+ are in particular interesting to investigate the effect of the target excitation prior to irradiation and to quantify how the production of the different pathways is affected. But also photoexcitation of molecular systems close to their ionization threshold would be an instructive model case to study the effect of non-adiabatic interactions between the electronic and nuclear motion.

Appendix A

Monte Carlo simulation

To derive the asymmetry parameter β , the energy of the observed photoelectrons $E_{(k,e^-)}$ or the total kinetic energy release E_{KER} of the photofragments from the experimental observations, the break-up-/ photoionization process is modeled with a Monte-Carlo simulation. The time-of-flight distributions of the emerging particles (neutral-, ionic fragments and electrons) inside the spectrometer or the mirror-unit are computed with SIMION [SIM] and in case of the photodetachment process studied with the magnetic-bottle spectrometer represented with a parametric Monte-Carlo model.

A.1 SIMION based Monte-Carlo Simulation

The electrostatic field prevailing in the saddle-point electron spectrometer (c.f. sec. 4.2) and the electrostatic mirror unit (c.f. sec. 3.1.3) are too complex to state an analytic expression for the trajectory of a fragment or electron propagating within these devices. Therefore, the paths of the particles arising from the photoionization or photofragmentation process have to be obtained from a numerical simulation based on SIMION.

Saddle point spectrometer

In SIMION, every electrode of the spectrometer is embedded as a potential array, which has to be modeled according to its dimensions. For each potential array the volume is split into sub-volumes, where the Laplace equation is solved [SIM]. Finally, the potential arrays of all electrodes of the system are combined. The crucial

point during the last step is to arrange the different potential arrays as close as possible to the real situation. For this, the spectrometer was operated to study the photodetachment of O^- at 532 nm, where the asymmetry parameter β and the detachment threshold are well known parameters. This reaction was therefore used as a model case to optimize the arrangement of the potential arrays to represent the obtained time-of-flight spectra (c.f. sec. 4.2).

Photoionization process

The Monte-Carlo model includes the kinematics of the ionization process for a certain kinetic energy $E_{(k,e^-)}$ of a randomly oriented, fast moving molecule. The interaction volume is given by the width of photon δ_{photon} and ion δ_{Ion} , respectively, i.e. the interaction point is randomly varied within the interaction volume. For a given asymmetry parameter $\beta \in [-1..2]$ and laser polarization the angular distribution of the photoelectrons is derived according to eq. (2.31). Afterwards, the electrons are propagated through the spectrometer towards the detection unit and the time-of-flight t to the respective detector is recorded and histogrammed to obtain a distribution $P_{\text{MC}}(t, \beta, E_{(k,e^-)}, \mathbf{p})$. By this, the measured time-of-flight spectra are represented and the asymmetry parameter β as well as the kinetic energy $E_{(k,e^-)}$ can be derived.

Setup parameter		Lower limit	Upper limit	Unit
Drift length	L_D	149	151	mm
Kinetic energy of ion beam	E_{Ion}	2900	6100	eV
Width ion beam	δ_{Ion}	0	2	mm
Width photon beam	δ_{Photon}	0	2	mm
Offset saddle point	$\Delta \mathbf{x}_S$	(-3,-3,-3)	(3,3,3)	mm
Pot. central electrodes	U_{C_1, C_2}	-10	-200	V
Pot. Up down electrodes	U_{U_0, D_0}	+0	+200	V
Pot. odd drift unit electrodes	$U_{U_{\text{odd}}, D_{\text{odd}}}$	-1	-100	V
Pot. even drift unit electrodes	$U_{U_{\text{even}}, D_{\text{even}}}$	-1	-100	V

Table A.1: Set of adjustable parameters \mathbf{p} of SIMION based Monte-Carlo simulation of photoionization process. The different electrodes of the saddle-point spectrometer C_1 , C_2 , U_0 , D_0 and U , $D_{\text{odd,even}}$ are introduced in section 3.2.

Fragmentation process

The modeling of the fragmentation process is used to extract the charge to mass ratio of the break-up products observed with the different fragment detectors. Eqs. (3.2) and (3.3) express how the parallel velocity of a neutral and charged break-up product depends on the potential U_B which is applied to the central electrodes of the spectrometer. There, the extend of the interaction region was not taken into account. With the simulation two-body break-up processes of a certain kinetic energy release E_{KER} can be modeled in a finite interaction volume spanned by the width of photon δ_{Photon} and ion δ_{Ion} beam. Similar to the approach described above a certain number of randomly oriented, fast moving molecules is fragmented where the angular distribution is computed according eq. (2.27) and the interaction point is varied within the interaction volume. The break-up products are propagated through the potential landscape imposed by the biased central electrodes of the spectrometer and the mirror unit while the time-of-flight t is recorded. Finally, the set of times t of a certain fragment species F is histogrammed to obtain a distribution $P_{\text{MC}}(t, F, \beta, E_{\text{KER}}, \mathbf{p})$ which allows to assign the charge-to-mass ratio to the break-up product.

Setup parameter		Lower limit	Upper limit	Unit
Kinetic energy ion beam	E_{Ion}	4100	4300	eV
Width ion beam	δ_{Ion}	0	2	mm
Width photon beam	δ_{Photon}	0	2	mm
Pot. central electrodes	$U_{(C_1, C_2)}$	-200	+200	V
Pot. Up down electrodes	$U_{(U_0, D_0)}$	-200	+200	V
Pot. pre-deflector	$U_{\text{pre.}}$	-2000	+2000	V
Pot. post-deflector	$U_{\text{post.}}$	-2000	+2000	V
Pot. Mirror M1...M7	$U_{M1}...U_{M7}$	0	6000	V

Table A.2: Set of adjustable parameters \mathbf{p} of SIMION based Monte-Carlo simulation of photofragmentation process. The different electrodes of the mirror unit $U_{M1}..U_{M7}$ are introduced in section 3.1.3.

A.2 Parametric Monte-Carlo model

The parametric Monte-Carlo model has been introduced and applied to represent the photoelectron time-of-flight distribution observed with the magnetic bottle spectrometer [Dom10]. The complexity in modeling the photoelectron time-of-flight dis-

tribution obtained with a magnetic bottle spectrometer, arises from finding an appropriate representation of the parallelization process. Once the electrons have reached the drift unit the propagation therein can be represented by pure drifting. The analytical expression in eq.(2.38) represents the essential features of the observable time-of-flight distribution, but the idealized assumption of instantaneous and complete parallelization of the momenta for all electrons is oversimplifying. As an improved approximation, the parallelization may be considered adiabatic [Kru83], meaning that the angular momenta of the electrons are considered conserved during the (still instantaneous) magnetic bending. In this case the transfer of transverse to longitudinal momentum is governed only by the ratio of the magnetic field strength at the interaction point and in the drift tube.

In the actual experiment, also this adiabatic approximation cannot be considered fulfilled, and moreover, the time spent in the inhomogeneous part of the magnetic field cannot be neglected. Additionally, the conditions of the actual experimental setup, such as the finite beam sizes, the temporal laser pulse width affect the observed time-of-flight distribution. Thus, to obtain a realistic representation of the observed photoelectron distribution, a parametric Monte Carlo model $P_{\text{MC}}(t, E_{(\text{k}, \text{e}^-)}, \beta, \mathbf{p})$ is introduced where $\mathbf{p} = (A_0, A_1, L_{\text{d}}, \delta t)$ holds a set of parameters that accounts for deviations from the idealized distribution, (c.f eq. (2.38)).

In this model, the parallelization of the electron velocities is described by two parameters, A_0 and A_1 , such that the final transverse velocity of an emitted photoelectron can be written as

$$v_{\text{eff}}^{\perp} = v_{\text{e}}^{\perp} \sqrt{A_0 + A_1 \frac{v_{\text{e}}^{\perp}}{v_0}} \quad (\text{A.1})$$

where A_0 accounts for an adiabatic parallelization and A_1 for first-order deviations from adiabaticity. The normalization of v_{e}^{\perp} to the ion velocity v_0 is performed to express A_1 as dimensionless number. To parametrically describe the combined effects of the non-instantaneous bending process, the finite beam sizes, the finite laser temporal width an effective distance L_{eff} from the interaction region to the detector and an effective temporal resolution δt is introduced.

For a given set of parameters, the Monte Carlo distribution $P_{\text{MC}}(t, E_{(\text{k}, \text{e}^-)}, \beta, \mathbf{p})$ is obtained numerically as follows:

A set of random inclination angles $\tilde{\theta}$ is generated obeying the general distribution in eq. (2.31), together with a set of random azimuth angles $\tilde{\phi} \in [0; 2\pi]$. The initial electron velocities $v_{\text{ei}}^{\parallel}$, v_{ei}^{\perp} are calculated according eq. (2.34). The final electron ve-

locities after the magnetic bending $v_{\text{eff.}}^{\parallel}$, $v_{\text{eff.}}^{\perp}$ are determined by applying eq. (A.1). After the parallelization the time-of-flight to the detector simply depends on the effective velocity $v_{\text{eff.}}$ and is computed as $t = L_{\text{eff.}}/v_{\text{eff.}}^{\parallel}$. In the final step, the resulting set of times t is histogrammed to form a distribution $P_{\text{MC}}^0(t)$ and folded with a Gaussian of width (RMS) δt to obtain the final distribution $P_{\text{MC}}(t, E_{(\text{k}, \text{e}^-)}, \beta, \mathbf{p})$. A least squares fit to the experimental distribution allows to extract the asymmetry parameter β , the energy of the observed photoelectrons $E_{(\text{k}, \text{e}^-)}$ as well as the parameter set $\mathbf{p} = (A_0, A_1, L_{\text{eff.}}, \delta t)$.

Bibliography

- [Ack07] W. Ackermann et *al.*: Operation of a free-electron laser from the extreme ultraviolet to the water window. *Nature Photonics*, **1**, p. 336-342 (2007).
- [Adl82] S.M. Adler-Golden. Sum rules for molecular Electronic spectra: Application to exact and reflection principle. *Chem. Phys.*, **64**, p. 421-426 (1982).
- [Alt03] S. M. Altevogt. *Production of rotationally cold H_3^+ ions with a hollow cathode ion source*. Diploma thesis, Ruperto-Carola-University of Heidelberg, (2003).
- [Alt07] S. M. Altevogt, *Fast-beam Photodissociation Imaging of Molecular Ions* . Ph.D. thesis, Ruperto-Carola-University of Heidelberg, Germany (2007).
- [Asm03] K. R. Asmis, N. L. Pivonka, G. Santambrogio, M. Brümmer, C. Kaposta, D. M. Neumark and L. Wöste. Gas-Phase Infrared Spectrum of the Protonated Water Dimer. *Science*, **299**, 1375 (2003).
- [Aug25] P. Auger. Sur l'effet photoélectrique composé. *J. Phys. Radium*, **6**, 205 (1925).
- [Bal92] A. Balakrishnan, V. Smith, and B.P. Stoicheff. Dissociation energy of the hydrogen molecule. *Phys. Rev. Lett.*, **14**, p. 2149 (1992).
- [Bar09] S. Barth, M. Oncak, V. Ulrich, M. Mucke, T. Lischke, P. Slavicek, and U. Hergenrohn. Valence Ionization of Water Clusters: From Isolated Molecules to Bulk. *J. Phys. Chem. A*, **113**, p. 13519-13527 (2009).
- [Bel07] L. Belau, K. R. Wilson, S.R. Leone, and Musahid Ahmed. Vacuum Ultraviolet (VUV) Photionization of Small Water Clusters. *J. Phys. Chem. A*, **111**, p. 10075-10083 (2007).
- [Blo05] C. Blondel, C. Delsart, C. Valli, S. Yiou, M. R. Godefroid, and S. Van Eck, *Phys. Rev. A* **64**, 052504 (2001).
- [Bor27] M. Born and R. Oppenheimer. Zur Quantentheorie der Molekeln. *Ann. Phys.*, **84**(4) p. 457-484 (1927).
- [Bra58] L. M. Branscomb, D. S. Durch, S. J. Smith, and S. Geltman. Photodetachment Cross Section and the Electron Affinity of Atomic Oxygen. *Phys. Rev.*, **111**, 504 (1958).
- [Bra65] L. M. Branscomb, S. J. Smith, and G. Tisone. Oxygen Metastable Atom Production Through Photodetachment. *J. Chem. Phys.*, **43**, 2906 (1965).

- [Bre78] F. Breyer, P. Frey, and H. Hotop. High resolution photoelectron spectrometry of negative ions: Fine-structure transitions in O^- and S^- photodetachment. *Z. Phys. A*, **286**, 133 (1978).
- [Buh10] H. Buhr, J. Stützel, M. B. Mendes, O. Novotný, D. Schwalm, M. Berg, D. Bing, M. Grieser et al. Hot Water Molecules from Dissociative Recombination of D_3O^+ with Cold Electrons. *Phys. Rev. Lett.*, **105**(10), (2010) 103202.
- [Bus72] F. von Busch and G. H. Dunn. Photodissociation of H_2^+ and D_2^+ : Experiment. *Phys. Rev. A*, **5**(4), 1726-1743, (1972).
- [Cav07] S. J. Cavanagh, S. T. Gibson, M. N. Gale, C. J. Dedman, E. H. Roberts, and B. R. Lewis. High-resolution velocity-map-imaging photoelectron spectroscopy of the O^- photodetachment fine-structure transitions. *Phys. Rev. A*, **76**, 052708 (2007).
- [Ced97] L.S. Cederbaum, J. Zobeley, and F. Tarantelli. Giant Intermolecular Decay and Fragmentation of Clusters. *Phys. Rev. Lett.*, **79** (24), p. 4778-4781, (1997).
- [Ced04] L.S. Cederbaum and G.A. Worth. BEYOND BORN-OPPENHEIMER: Molecular Dynamics Through a Conical Intersection. *Ann. Rev. of Phys. Chem.*, **55**, p. 127-158 (2004).
- [Cha72] R. L. Chase and H. P. Kelly. Many-Body Calculation of the Photodetachment Cross Section of O^- . *Phys. Rev A*, **6**, 2150 (1972).
- [Che87] O. Cheshnovsky, S. H. Yang, C. L. Pettiette, M. J. Craycraft, and R. E. Smalley. Magnetic time-of-flight photoelectron spectrometer for mass selected negative cluster ions. *Rev. Sci. Instrum.*, **58**, 2131 (1987).
- [Coo62] J. W. Cooper and J. B. Martin. Electron Photodetachment from Ions and Elastic Collision Cross Sections for O, C, Cl, and F. *Phys. Rev.*, **126**, p. 1482-1488 (1962).
- [Coo68] J. Cooper and R. N. Zare. Angular distribution of photoelectrons. *J. Chem. Phys.*, **48**p. 942-943 (1968).
- [Dah97] M. Dahan, R. Fishman, O. Heber, M. Rappaport, N. Altstein, D. Zajfman, and W. J. van der Zande. A new type of electrostatic ion trap for storage of fast ion beams. *Review of Scientific Instruments*, **69**(1), p. 76-83 (1998).
- [Dal53] R. H. Dalitz. On the Analysis of τ Meson Data and the Nature of the τ Meson. *Philos. Mag.*, **44**(357), 1068 (1953).
- [Dem03] W. Demtröder. *Molekülphysik*. Oldenbourg Wissenschaftsverlag, 2003.

-
- [Dom10] C. Domesle, B. Jordan-Thaden, L. Lammich, M. Förstel, U. Hergenhahn, A. Wolf and H. B. Pedersen. Photoelectron spectroscopy of O^- at 266 nm: ratio of ground and excited atomic oxygen production and channel resolved photoelectron anisotropy parameters. *Phys. Rev. A*, **82**, 033402 (2010).
- [Eli76] L. R. Elias et al.. Observation of Stimulated Emission of Radiation by Relativistic Electrons in a Spatially Periodic Transverse Magnetic Field. *Phys. Rev. Lett.*, **36**, 717 (1976).
- [Emm10] P. Emma, R. Akre, J. Arthur, R. Bionta, C Bostedt et al. . First lasing and operation of an angstrom-wavelength free electron laser. *Nature Photonics*, **4**, p. 641-647 (2010).
- [For10] M. Förstel *et al.*, to be published.
- [For12] M. Förstel, *Investigation of non-local autoionization processes in rare gas clusters*. Ph. D. thesis, Technische Universität Berlin, Germany (2012).
- [Gar67] W. R. Garrett and H. T. Jackson. Electron Photodetachment from O^- and Elastic Scattering from Atomic Oxygen. *Phys. Rev.*, **153**, 28 (1967).
- [Gre82] C.H. Greene and R.N. Zare. Photofragment alignment and orientation. *Ann. Rev. Phys. Chem.*, **33** p. 119-50 (1982).
- [Gia94] F. Di Giacomo, F. A. Gianturco, F. Raganelli, and F. Schneider. Selective Vibrational Excitations in Proton-Water Collisions: A Study Based on CI Calculations. *J. Chem. Phys.*, **101**, 3952 (1994).
- [Gin01] R. Giniger, T. Hippler, S. Ronen, and O. Cheshnovsky, *Rev. Sci. Instrum.*, **72**, 2543 (2001).
- [Hal68] J. L. Hall and M. W. Siegel. Angular Dependence of the Laser Photodetachment of the Negative Ions of Carbon, Oxygen, and Hydrogen. *J. Chem. Phys.*, **48**, p. 943 (1968).
- [Han89] D. Hanstorp, C. Bengtsson, and D. J. Larson. Angular distributions in photodetachment from O^- . *Phys. Rev A*, **40**, p. 670 (1989).
- [Han99] K. A. Hanold, A. K. Luong, T. G. Clements, and R. E. Continetti. Photoelectron-multiple-photofragment coincidence spectrometer. *Rev. Sci. Instrum.*, **70**, 2268 (1999).
- [Hea05] J. M. Headrick, E. G. Diken, R. S. Walters, N. I. Hammer, R. A. Christie, J. Cui, E. M. Myshakin, M. A. Duncan, M. A. Johnson and K. D. Jordan. Spectral Signatures of Hydrated Proton Vibrations in Water Clusters. *Science*, **308**, p. 1765-1769 (2005).

-
- [Hel93] H. Helm, N. Bjerre, M. J. Dyer, D. L. Huestis, and M. Saeed. Images of photoelectrons formed in intense laser fields. *Phys. Rev. Lett.*, **70**, 3221 (1993).
- [Hen67] R. J. Henry. Elastic Scattering from Atomic Oxygen and Photodetachment from O^- . *Phys. Rev. A*, **162**, 55 (1967).
- [Hla09] P. Hlavenka, R. Otto, S. Trippel, J. Mikosch, M. Weidemüller, and R. Wester. Absolute photodetachment cross section measurements of the O^- and OH^- anion. *J. Chem. Phys.*, **130**, 061105 (2009).
- [Hol99] D. J. Hollenbach and A. G. G. M. Tielens. Photodissociation regions in the interstellar medium of galaxies. *Rev. Mod. Phys.*, **71**, p. 173 (1999).
- [Hun98] E. P. L. Hunter and S.G. Lias. Evaluated Gas Phase Basicities and Proton Affinities of Molecules: An Update. *J. Phys. Chem. Ref. Data*, **27**, p. 413 (1998).
- [Jag02] O. Jagutzki, V. Mergel, K. Ullmann-Pfleger, L. Spiegelberger, U. Spillmann, R. Dörner, and H. Schmidt-Böcking. A broad-application microchannel-plate detector system for advanced particle or photon detection tasks: large area imaging, precise multi-hit timing information and high detection rate. *Nucl. Instr. Meth. Phys. Res. A*, **477**, p. 244-249 (2002).
- [Kin77] B. M. Kincaid. A short-period helical wiggler as an improved source of synchrotron radiation. *Journal of Applied Physics*, **48**, 2684 (1977).
- [Kon80] A. M. Kondratenko and E. L. Saldin. Generation of coherent radiation by a relativistic electron beam in an undulator. *Part. Accel.*, (10) p. 207-216 (1980).
- [Koo34] T. Koopmans, *Physica*, (Amsterdam), **1**, 104 (1934).
- [Kru83] P. Kruit and F. H. Read. Magnetic field parallelizer for 2π electron-spectrometer and electron-image magnifier. *J. Phys.*, E 16, 313 (1983).
- [Lam10] L. Lammich, C. Domesle, B. Jordon-Thaden, M. Förstel, T. Arion, T. Lischke, O. Heber, S. Klumpp, M. Martins, N. Guerassimova, R. Treusch, J. Ullrich, U. Hergenhahn, H. B. Pedersen, and A. Wolf. Fragmentation Pathways of $H^+(H_2O_2)$ after Extreme Ultraviolet Photoionization. *Phys. Rev. Lett.*, **105**, 253003 (2010).
- [Leq91] J. Lequeux and E. Roueff. Interstellar molecules. *Physics Reports*, **200(5)**, p. 241-299 (1991).
- [Mal96] P. R. Maloney, D. J. Hollenbach, and A. G. G. M. Tielens. X-ray-irradiated molecular gas. I. Physical processes and general results. *Astrophys. J.*, **466**, 561 (1996).

-
- [Mar99] D. Marx, M. E. Tuckermann, J. Hutter, and M. Parrinello. The nature of the hydrated excess proton in water. *Nature*, (London), **397**, 601 (1999).
- [Mar06] M. Martins, M. Wellhöfer, J. T. Hoeft and W. Wurth. Monochromator beamline for FLASH. *Review of Scientific Instruments*, **77**, 115108 (2006).
- [Muc11] M. Mucke, *Employing electron-electron coincidence techniques to investigate the autoionization of clusters*. Ph. D. thesis, Technische Universität Berlin, Germany (2011).
- [Muc12] M. Mucke, M. Förstel, T. Lischke, T. Arion, A. M. Bradshaw, and U. Hergenbahn. Performance of a short magnetic bottle electron spectrometer. Submitted to *Rev. Sci. Instr.* .
- [Mue04] I. B. Müller, L.S. Cederbaum and F. Tarantelli. Microsolvation of Li^+ in water analyzed by ionization and double ionization. *J. Phys. Chem. A*, **108** p. 5831-44 (2004).
- [Mue05] I. B. Müller and L.S. Cederbaum. Electronic decay following ionization of aqueous Li^+ microsolvation clusters. *J. Chem. Phys. A*, **122** 094305 (2005).
- [Mul71] R. S. Mulliken. Role of kinetic energy in the Franck-Condon principle. *J. Chem. Phys.*, **55**, 309 (1971).
- [Neu29] J. von Neumann and E. Wigner. Über merkwürdige diskrete Eigenwerte. Über das Verhalten von Eigenwerten bei adiabatischen Prozessen, *Phys. Z.*, **30**, p. 467-470 (1929).
- [Neu85] D. M. Neumark, K. R. Lykke, T. Andersen, and W. C. Lineberger. Laser photodetachment measurement of the electron affinity of atomic oxygen. *Phys. Rev. A*, **32**, 1890 (1985).
- [Nie08] G. Niedner-Schattenburg. Infrarotspektroskopie und Ab initio Theorie des H_5O_2^+ : Von einem Eimer Wasser zur Schrödinger-Gleichung und zurück. *Angew. Chem., Int. Ed.*, **47**, 1008 (2008).
- [Nist] National Institute of Standards and Technology database, <http://www.nist.gov>.
- [Nod82] C. Noda and R.N. Zare. Relation between Classical and Quantum Formulations of the Franck-Condon Principle: The Generalized r-Centroid Approximation. *J. of Mol. Spec.*, **95**, p. 254-270 (1982).
- [Oze72] J. B. Ozenne, D. Pham, and J. Durup. Photodissociation of H_2^+ by monochromatic light with energy analysis of the ejected H^+ ions. *Chem. Phys. Lett.*, **17(3)**, p. 422-424, (1972).

- [Ped99] H. B. Pedersen, M. J. Jensen, C. P. Safvan, X. Urbain, and L. H. Andersen. Fast beam photofragment apparatus for studies of electronic and nuclear dynamics. *Rev. Sci. Instrum.*, **70**, 3298 (1999).
- [Ped07] H. B. Pedersen, S. Altevogt, B. Jordon-Thaden, O. Heber, M. L. Rappaport, D. Schwalm, J. Ullrich, D. Zajfman, R. Treusch, N. Guerassimova, M. Martins, J.-T. Hoeft, M. Wellhöfer, and A. Wolf. Crossed beam photodissociation imaging of HeH^+ with vacuum ultraviolet free-electron laser pulses. *Phys. Rev. Lett.*, **98**, 223202 (2007).
- [Ped09] H. B. Pedersen, S. Altevogt, B. Jordon-Thaden, O. Heber, L. Lammich, M. L. Rappaport, D. Schwalm, J. Ullrich, D. Zajfman, R. Treusch, N. Guerassimova, M. Martins, and A. Wolf. Neutral and charged photofragment coincidence imaging with soft x rays on molecular ion beams: Breakup of H_3O^+ at 13.5 nm. *Phys. Rev. A*, **80**, 012707 (2009).
- [Ped10] H. B. Pedersen, L. Lammich, C. Domesle, B. Jordon-Thaden, O. Heber, J. Ullrich, R. Treusch, N. Guerassimova, and A. Wolf. Experimental investigation of dissociation pathways of cooled HeH^+ following valence electron excitation at 32 nm by intense free-electron-laser radiation. *Phys. Rev. A*, **82**, 023415 (2010).
- [Ped12] H. B. Pedersen *et al.* to be published.
- [Peg89] D. J. Pegg, J. S. Thompson, R. N. Compton, and G. D. Alton, *Nucl. Inst. Meth.*, **B40/41**, 221 (1989).
- [Raf77] R. C. Raffanetti, H. J. T. Preston, and J. J. Kaufman. Ab-initio configuration interaction calculations of hydronium ion excited states. *Chem. Phys. Lett.*, **46**, 513 (1977).
- [Rij00] A. M. Rijs, E. H. G. Backus, C. A. De Lange, N. P. C. Westwood, M. H. M. Janssen, *J. Elec. Spec. Rel. Phen.*, **112**, 151 (2000).
- [Rob67] E. J. Robinson and S. Geltman. Single- and Double-Quantum Photodetachment of Negative Ions. *Phys. Rev.* **153** 4 (1967).
- [Sal00] E. L. Saldin, E. A. Schneidmüller, and M. V. Yurkov. The physics of Free Electron Lasers. Springer-Verlag Berlin Heidelberg, 2000.
- [Sch08] P. Schmüser, M. Dohlus and J. Rossbach. Ultraviolet and Soft-X-Ray Free Electron Lasers. Springer-Verlag (2008)
- [Sea85] T. J. Sears, P. R. Bunker, P. B. Davies, S. A. Johnson, and V. Spriko. Diode laser absorption spectroscopy of D_3O^+ : Determination of the equilibrium structure and potential function of the oxonium ion. *J. Chem. Phys.*, **83**(6), (1985) 2676.

- [SIM] SIMION Version 8.0, www.simion.com.
- [Spi01] U. Spillmann, O. Jagutzki, L. Spiegelberger, R. Dörner, V. Mergel, K. Ullmann-Pfleger, and H. Schmidt-Böcking. A novel delay-line anode design for position and time sensitive read-out of MCP-based detectors. *Physica Scripta.*, T92:225-226, 2001.
- [Sta05] P. Stäuber, S. D. Doty, E. F. van Dishoeck, and A. O. Benz, Astron. X-ray chemistry in the envelopes around young stellar objects. *Astrophys.*, **440**, 949 (2005).
- [Ste01] Z. Sternovsky, M. Horanyi, and S. Robertson. Collision cross sections of small water clusters. *Phys. Rev. A*, **64**, 023203 (2001).
- [Ste95] A. Sternberg and A. Dalgarno. Chemistry in dense photon-dominated regions. *Astrophys. J.*, **99**, 565 (1995).
- [Ste79] R. M. Stehman and S. B. Woo. Zero-core-contribution model and its application to photodetachment of atomic negative ions. *Phys. Rev. A*, **20**, 281 (1979).
- [Sto06] E. S. Stoyanov and C. A. Reed. IR Spectrum of the H_5O_2^+ Cation in the Context of Proton Disolvates $\text{L-H}^+-\text{L}$. *J. Phys. Chem. A*, **110**, p. 12992-13002 (2006).
- [Stu11] J. Stützel, *Fragmentation of Small Multi-Electron Molecular Ions in Cold Electron Collisions*. Ph.D. thesis, Ruperto-Carola-University of Heidelberg, Germany (2011).
- [Suz87] T. Suzuki and T. Kasuya. Optogalvanic study of photodetachment of O^- near threshold. *Phys. Rev. A*, **36**, 2129 (1987).
- [Taf10] U. F. Ndongmouo Taffoti, P. M. Dinh, P-G. Reinhard, E. Suraund, and Z. P. Wang Exploration of dynamical regimes of irradiated small protonated water clusters. *Eur. Phys. J. D*, **58**, 131 (2010).
- [Tie09] K. Tiedtke *et al.* The soft x-ray free-electron laser FLASH at DESY: beam-lines, diagnostics and end-stations. *New J. Phys.*, **11**, 023029 (2009).
- [Tre05] R. Treusch, Photon Diagnostics for the VUV-FEL. *HASYLAB Annual Report*, p. 159 (2005).
- [Van74] N. P. F. B. van Asselt, J. G. Maas, and J. Los. Laser induced photodissociation of H_2^+ ions. *Chem. Phys. Lett.*, **24(4)**, p. 555-558 (1974).
- [Ven08] O. Vendrell and H. D. Meyer. A proton between two waters: insight from fulldimensional quantum-dynamics simulations of the $[\text{H}_2\text{O} - \text{H} - \text{OH}_2]^+$ cluster. *Chem. Phys.*, **10**, 4692 (2008).

- [Ven12] Z. Li, M. El-Amine Madjet and O. Vendrell, private communication.
- [Way00] R. P. Wayne. Chemistry of Atmospheres. *3rd ed., Oxford University Press*, New York, (2000).
- [Wol10] A. Wolf, H.B. Pedersen, L. Lammich, B. Jordan-Thaden, S. Altevogt, C. Domesle, U. Hergenhahn, M. Förstel, and O. Heber. Soft-x-ray fragmentation studies of molecular ions. *J. Phys. B: At. Mol. Opt. Phys.*, **43**, 194007 (2010).
- [Wu03] J. -H. Wu, J.-M. Yuan, and K. L. Vo. Near threshold photodetachment cross section of negative atomic oxygen ions. *Chin. Phys.*, **12**, 1390 (2003).
- [Xie94] Y. Xie, R. B. Remington, and H. F. Schaefer. The protonated water dimer: Extensive theoretical studies of H_5O_2^+ . *J. Chem. Phys.*, **101**, 4878 (1994).
- [Yeh89] L. I. Yeh, M. Okumura, J. D. Myers, J.M. Price and Y.T. Lee. Vibrational spectroscopy of the hydrated hydronium cluster ions $\text{H}_3\text{O}^+(\text{H}_2\text{O})_n$ ($n=1, 2, 3$). *J. Chem. Phys.*, **91**, 7319 (1989).
- [Zar72] R. N. Zare. Photoejection dynamics. *Mol. Photochem.*, 4:1-37 (1972).
- [Zat06] O. Zatsarinny and K. Bartschat. Low-energy photodetachment of O^- . *Phys. Rev. A* **73**, 022714 (2006).
- [Zaj97] D. Zajfman, O. Heber, L. Vejby-Christensen, I. Ben-Itzhak, M. Rappaport, R. Fishman, and M. Dahan. Electrostatic bottle for long-time storage of fast ion beams. *Phys. Rev. A*, **55**(3), p. 1577-1580 (1997).

Danksagung

Am Ende noch ein großes Danke! an all diejenigen, ohne deren Unterstützung die Arbeit in dieser Form nicht vorliegen würde. Besonders danken möchte ich:

Andreas Wolf für die freundliche Aufnahme in seine Arbeitsgruppe mit den damit verbundenen vielfältigen Aufgabenstellungen bei TIFF und seiner großen Unterstützung beim Erstellen dieser Arbeit.

Alexander Dorn für seine Bereitschaft das Zweitgutachten dieser Arbeit zu erstellen.

Henrik Pedersen für seine unzähligen kleinen und großen Anregungen bei der Entwicklung der diversen Bauteile, sowie der großen Unterstützung beim Auswerten und Interpretieren der Daten.

Lutz Lammich dafür, dass er mir zu Beginn der Datenauswertung hilfreiche Tipps gegeben hat.

Florian Grussie, Claude Krantz, JP und Julia Stützel fürs Korrekturlesen und ihren Anregungen bei der Auswertung und zur Gestaltung der Arbeit.

Weiterhin geht ein großen Danke an Brandon Jordan-Thaden, Marko Förstel, Toralf Lischke und Tiberiou Arion für die gute Atmosphäre während der FLASH Strahlzeiten.

Siarhei Dziarzhyski, Natalia Gerasimova und Holger Weigelt für ihren Einsatz an der PG2 beamline bei FLASH.

Arno Becker, Felix Berg, Max Berg, Dennis Bing, Mike Froese, Philipp Herwig, Holger Kreckel, Michael Lange, Mario Mendes, Sebastian Menk, Oldrich Novotny, Andrey Shornikov, Kaija Spruck und allen anderen für die angenehme Arbeits-Atmosphäre und die lustigen Kaffeerunden.

Meiner Mutter ohne deren Unterstützung in den vergangenen Jahren das Studium so nicht möglich gewesen wäre.

Zum Abschluss möchte ich noch ganz besonders Dir liebe Nicola Danke sagen. Du hast mit Deiner mentalen Unterstützung sowie Deinem Korrekturlesen sehr zum Gelingen dieser Arbeit beigetragen.